First Study of Three-body Photodisintegration of ^{3}He with Double Polarizations at HIγS

by

Xing Zong

Department of Physics
Duke University

Date: _____

Approved:

_____
Haiyan Gao, Advisor

_____
Tom Mehen

_____
John Thomas

_____
Henry Weller

_____
Ying Wu

Dissertation submitted in partial fulfillment of the requirements for the degree of
Doctor of Philosophy in the Department of Physics
in the Graduate School of Duke University
2010

Abstract

First Study of Three-body Photodisintegration of ^{3}He with Double Polarizations at HIγS

by

Xing Zong

Department of Physics
Duke University

Date: _____

Approved:

_____
Haiyan Gao, Advisor

_____
Tom Mehen

_____
John Thomas

_____
Henry Weller

_____
Ying Wu

An abstract of a dissertation submitted in partial fulfillment of the requirements for the degree of Doctor of Philosophy in the Department of Physics in the Graduate School of Duke University
2010

Abstract

This dissertation describes the first measurement of three-body photodisintegration of polarized ^{3}He ($\gamma^3He \rightarrow npp$) with a circularly polarized photon beam.

This measurement was carried out at the High Intensity γ-Ray Source(HIγS) facility located at Duke University Free Electron Laser Laboratory and the incident photon energy was 11.4 MeV. A high-pressure polarized ^{3}He target based on spin exchange optical pumping (SEOP) of hybrid alkali was employed. Two methods—Nuclear Magnetic Resonance (NMR) and Electron Paramagnetic Resonance (EPR)—were used to measure the polarization, which was determined to be $\sim 42\%$.

The data from the experiment were analyzed and a GEANT4 simulation was carried out to determine the corrections for finite geometry, neutron multiple scattering and detector efficiencies used in this experiment. The results are compared to the state-of-the-art three-body calculations and agreements are observed within rather large statistical uncertainties of the measurement. This experiment represents the first measurement of the asymmetry using spin-dependent ^{3}He photodisintegration. The unpolarized differential cross section and helicity-dependent differential cross-section difference results are also presented and compared to the same theoretical calculations followed by a discussion of the results. Total cross section is also extracted using two different methods and agrees well with the theoretical prediction.

New developments including a Sol-Gel coated pyrex ^{3}He cell since the experiment

are then presented. The in-beam test results of the aforementioned target cell from May 2009 test run are included and the prospect of future three-body photodisintegration is discussed in the end.

To my parents Qingchao Xiao and Youxin Zong, also to Jidi Liu.

Contents

List of Tables

List of Figures

List of Abbreviations and Symbols

Abbreviations

ADC	Analog-to-Digital Converter
BC-501A	Organic liquid scintillator by Bicron
CAMAC	Computer Automated Measurement And Control
CFD	Constant Fraction Discriminator
DAQ	Data Acquisition System
DFELL	Duke Free Electron Laser Laboratory
FI/FO	Fan-in fan-out
GDH	Gerasimov-Drell-Hearn
GEANT	Nuclear Physics Monte Carlo Simulation Package
HIγS	High Intensity Gamma-ray Source
LOR	Light Output Response
OK	Optical Klystron
PH	Pulse Height
PMT	Photo-multiplier tube
PSD	Phase Shape Discrimination
TDC	Time-to-Digital Converter
TFA	Timing filter amplifer
TOF	Time-of-Flight
VME	IEEE standards for electronics modules

Acknowledgements

In August 2003, I came to Duke and began this journey to pursue my Ph.D. degree. Now, seven years passed, when this marathon journey is drawing to a close, I am keenly aware of how deeply indebted I am to so many people.

The first big thank goes to my advisor Prof. Haiyan Gao. Haiyan's door is always open and she really cares about my growth. I am constantly impressed by her enthusiasm in science and her speed in replying my email. I could not imagine accomplishing this thesis without her guidance and encouragement.

I want to thank MEP group members (current and previous). Alan's hand-on skill is remarkable and he takes immediate control whenever entering the laboratory. Xin always bombards me with new physics ideas and interesting insights. He gave me lots of help when I prepared for the qualify exams and I sincerely wish him become a successful scientist. Wei impresses me with his computer savvy and his quite way of thinking. He gave me numerous help in the data analysis. Rongchun and I worked together for several sleepless nights when setting up the experimental apparatus, which is unforgetable. Kevin is the original designer of this project and he taught me all the basics from scratch. I also want to thank Xiaofeng, Wangzhi, George and Dipangkar Dutta for their help. I will always cherish the precious friendship, both professional and personal.

This experiment could not be successful without the expertises from members of Capture group. Our collaboration has been a fruitful and pleasant one. I am grateful

to Prof. Henry Weller, Ahmed Mohammad, Sean Stave, Brent Perdue, Matthew Blackston for sharing their valuable time and knowledge with me. Especially, Sean and Brent always answered my questions patiently and gave me great help during the data analysis.

Working on a HIγS project gives me an opportunity to interact with many FEL staff members. I thank Prof. Ying Wu, Changchun Sun, Jingyi Li, Mark Emamian, etc. It was their outstanding support that made the experiment go smoothly. I also want to take this opportunity to thanks many TUNL faculty and staff members, Prof. Calvin Howell, Prof. Werner Tornow, Chris Westerfeldt, Alex Crowell, Bret Carlin, Brenda West, etc. It was a great pleasure to work with them.

I also want to take this opportunity to thank our collaborated theorists: Prof. Arnoldas Deltuva, Prof. Jacek Golak and Prof. Roman Skibinski. It is their excellent work that makes this experiment meaningful.

Many people at Physics Department helped me during the past six years. Among them are Prof. Springer, Prof. Mehen, Prof. Palmer, Donna Ruger, etc. I also enjoy the friendship of my physics grad peers, Peng Li, Phil Wu, James Esterline, Botao Jia, etc.

Last but not least, I want to thank my family members, especially my parents who never doubt that their son will eventually get a Ph.D. degree and have made countless sacrifices along the way. And I feel very fortunate to meet Jidi in graduate school. It is with deep love and gratitude that I dedicate this dissertation to her.

1

Introduction

1.1 Background

Understanding nuclear interactions is one of the most fundamental goals of nuclear physics. The Japanese physicist Hideki Yukawa first predicted that the exchange of a pion—the lightest meson—accounted for the force between two nucleons and this groundbreaking theory earned him a Nobel Prize in 1949. In 1964, two physicists, Murray Gell-Mann and George Zweig, independently proposed the existence of more elementary particles, i.e. quarks. Upon experimental verification, Gell-Mann was awarded the Nobel Prize for this theory five years later. In the 1970s, quantum chromodynamics (QCD), a fundamental theory that describes the strong interaction in terms of quark and gluon degrees of freedom, was proposed. The 2004 Nobel Prize in physics went to three physicists David J. Gross, H.David Politzer and Frank Wilczek for their pioneering work in this area.

Few-nucleon systems are excellent testing grounds to study the nuclear interaction. Among them, the three-nucleon system has long been of fundamental importance [1, 2] because it is the simplest system with more than two nucleons. Calcula-

tions (mainly in the form of Faddeev equations [1]) can be solved numerically for three-body systems using a variety of modern nucleon-nucleon (NN) potentials [3, 4, 5]. NN potentials are based on the traditional one-pion exchange potential and are not very accurate when applied to three-nucleon systems. Most noticeably, they fail to reproduce the binding energies of ^{3}H and ^{3}He. As a result, modern three-nucleon forces (3NFs) including the Tucson-Melbourne [6], Urbana [7] and Hanover models [8] have been adopted. Meanwhile, chiral Effective Field Theory (EFT), introduced by Weinberg [9] almost two decades ago, has become a powerful framework to analyze few-nucleon systems at low energy. There has been a proliferation of work in EFT and a good review can be found in [10]. For three-nucleon systems, calculations are now available at next-to-next-to-leading order (N^{2}LO) and have achieved good agreement with the experimental Nd scattering and Nd break-up data [10].

The advance of theories points to the necessity of rigorous tests by high precision experimental data and by new experimental observables which have not been measured previously. Electro- and photo-induced reactions are attractive probes because photons (real or virtual) interact with nucleons or nuclei through electromagnetic interactions, which are well understood, thus providing powerful probes into the structure of the nucleon and nuclei. Recent developments of polarized beams and polarized targets have made the investigation of the additional spin-dependent quantities possible.

Polarized ^{3}He targets are particularly important as effective polarized neutron targets [11, 12] due to the fact that the ground-state wave function is dominated by the S state in which the two proton spins cancel and the nuclear spin is carried by the unpaired neutron. There have been extensive studies employing polarized ^{3}He targets to extract the neutron electromagnetic form factors [13, 14, 15, 16, 17, 18], and to extract neutron spin structure functions [19, 20, 21]. To extract the information

[1] The details of the theory will be discussed in Chapter 2.

on the neutron using a polarized ^{3}He target, nuclear corrections need to be applied which rely on state-of-the-art calculations. A first precision measurement of the spin-dependent asymmetry in the threshold region of $^3\vec{H}e(\vec{e},e')$ at Q^2-values of 0.1 and 0.2 (GeV/c)^2 was reported in Ref. [22]. The agreement between the data and non-relativistic Faddeev calculations [23] which include both final-state interactions (FSI) and meson-exchange current (MEC) effects is very good at $Q^2 = 0.1$(GeV/c)^2, while a small discrepancy is observed at $Q^2 = 0.2$(GeV/c)^2. Compared with the considerable effort on electrodisintegration of ^{3}He, data from photodisintegration of ^{3}He, especially from the three-body channel are very scarce. Recently a simultaneous measurement of cross sections from two-body and three-body channels of ^{3}He was reported [24]. A severe discrepancy between the new data and theoretical calculations based on AV18+Urbana IX [25] nuclear forces including π- and ρ-like meson exchange current was observed at an incident photon energy of 10.2 MeV.

More recently, the three-nucleon breakup reaction calculation including the Coulomb interaction between two protons has been carried out in momentum space [26]. The calculation is based on the Alt-Grassberger-Sandhas (AGS) equation [27], and employs charge-dependence (CD) Bonn plus Coulomb as a pure nucleonic reference and two-baryon coupled-channel CD Bonn +Δ with Coulomb. The Δ-isobar excitation yields an effective three-nucleon force and effective two- and three-nucleon currents in addition to Δ-isobar effects. This calculation predicts a spin-dependent asymmetry for three-body photodisintegration of polarized ^{3}He breakup with polarized photons. It is important to test ^{3}He calculations at a level not tested before and in observables which have not been studied before. A precision measurement of this spin-dependent asymmetry will provide such a new test of the theory and it will also help future experiments using polarized ^{3}He to probe the structure of the neutron to reduce model uncertainties.

Three-body photodisintegration of ^{3}He is of further importance for future Gerasimov-

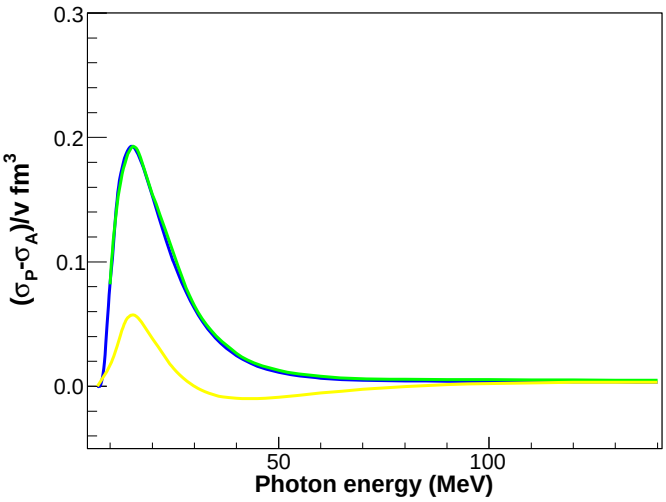

FIGURE 1.1: Three-body GDH integrand from A. Deltuva [28, 29]. Three curves are explained as follows: the green line uses CD Bonn + Δ potential, plus Siegert including relativistic charge operator (RCO), and explicit MEC (h.o.); the blue line (underneath the green line) uses CD Bonn plus Siegert including RCO and MEC (h.o.); and the yellow line is from CD Bonn, the Siegert theorem and MEC (h.o.). Here MEC (h.o.) means explicit MECs are used for magnetic multipoles and higher order terms of electric multipoles not accounted for by Siegert.

Drell-Hearn (GDH) sum rule [30] experiments. The GDH sum rule is constructed using the total helicity dependent nucleon (or nuclei) real photo-absorption cross sections σ_N^p (nucleon (or nuclei) spin parallel to the helicity of the photon) and σ_N^A (nucleon (or nuclei) spin anti-parallel to the helicity of the photon):

$$\int_{\nu_{thr}}^{\infty} (\sigma_N^P - \sigma_N^A)\frac{d\nu}{\nu} = \frac{4\pi^2\alpha}{M^2}\kappa_N^2 I, \tag{1.1}$$

where κ_N is the anomalous magnetic moment, M the mass and I is the spin of the nucleon or nuclei, $\alpha = \frac{e^2}{4\pi}$. This sum rule is based on rather general principles such as Lorentz and Gauge invariance, crossing symmetry and unitarity, as well as an unsubtracted dispersion relation applied to the forward Compton amplitude [30]. A simple derivation will be given in Chapter 2. It relates the anomalous magnetic moment—a static ground state property—of the nucleus to the excitation spectrum

of the polarized target. Recently, there have been worldwide efforts [31, 32] in testing GDH sum rules on the nucleon and testing GDH sum rule on ^{3}He is just as interesting and important. The energy range that interests us is from the two-body break-up threshold (∼5.5 MeV) to the pion production threshold (∼140 MeV). There are two reasons for this. First, there is an enormous strength expected to be present in this range, which we will discuss in details in Section 2.6. Second, this is the energy range that we can do measurements using the HIγS facility. The calculations [28] mentioned above demonstrate that the three-body breakup channel below 40 MeV dominates the integrand, as shown in Fig 1.1. There are three curves in this plot: The green line uses CD Bonn + Δ potential, plus Siegert including relativistic charge operator (RCO) [2], and explicit MEC (h.o.) [3]; the blue line (underneath the green line) uses CD Bonn plus Siegert including RCO and MEC (h.o.); and the yellow line is from CD Bonn, the Siegert theorem and MEC (h.o.). The large difference between the top two curves and the bottom curve shows that the considered observable is very sensitive to the relativistic corrections. Therefore, a spin-dependent asymmetry measurement from $^3\vec{H}e(\vec{\gamma}, n)pp$ will not only provide a stringent test of the modern three-body calculations, but will also serve as an important step towards an experimental test of the GDH sum rule on ^{3}He nucleus in the future when one combines measurements from ^{3}He using photon energies above the pion production threshold from other laboratories.

1.2 Review of Three-body Photodisintegration Measurements

In this section, I will briefly review the previous three-body photodisintegration experiments which were carried out for $E_\gamma < 140\ MeV$.

[2] In Deltuva's calculation, nonrelativistic charge is of zeroth order, and the leading relativistic charge corrections are of the second order. RCO is sum of the zeroth and the second order terms.

[3] Here MEC (h.o.) means explicit MECs are used for magnetic multipoles and higher order terms of electric multipoles not accounted for by Siegert.

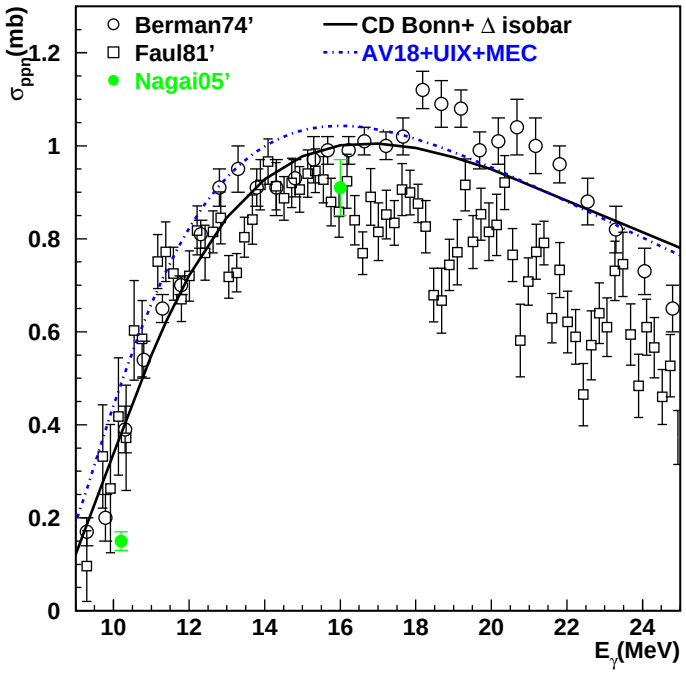

FIGURE 1.2: Total $^3He(\gamma, pp)n$ cross sections. Two sets of calculations with two different dynamical inputs: CD Bonn + Δ isobar (solid line, from Deltuva [33]), AV18 + UrbanaIX + MEC (dotted line, from Skibinski [34]). Three sets of data include Nagai 05' [24] (only at 10.2 and 16 MeV) are plotted.

Figure 1.2 shows a comparison between two state-of-the-art theoretical calculations and three sets of experimental data. In 1974, Berman *et al.* reported the first low-energy measurement [35] for three-body photodisintegration of ^{3}He and ^{3}H from breakup threshold to 30 MeV using a photon beam from positron annihilation at Livermore. At ∼15 MeV, the cross section reached the peak value, then sharply decreased as the photon energy increased. As observed from the plot, at the higher E_γ side, there was a disagreement with the theoretical calculation from Golak and Skibinski *et al.* [23]. In 1981, an experiment carried out again at Livermore was reported [36]. This experiment also used a photon beam from positron annihilation

up to 25 MeV, to measure the cross sections of two- and three-body photodisintegration of ^{3}H and ^{3}He. There was some discrepancy between the data from these two measurements, as seen from Figure 1.2.

The third and most recent set of data was from a simultaneous measurement of the cross sections of $^3He(\gamma, p)d$ and $^3He(\gamma, pp)n$ in 2005 [24]. This experiment used a pulsed laser-Compton backscattered γ-ray beam at 10.2 and 16.0 MeV. As described before, a severe discrepancy was observed at 10.2 MeV when comparing the data to Golak's calculation [23] which is based on the AV18+Urbana IX nuclear force including π- and ρ-like meson exchange currents. The theory missed the data by a factor of 3. One possible explanation was the lack of the Coulomb force in the continuum. However, the Coulomb force alone cannot fully explain the discrepancy since Deltuva predicts that the three-body cross section would only decrease by $\sim 25\%$ compared with Golak's result at 10 MeV [29], as indicated by the solid line.

With the recent development of polarized beam and polarized targets, new experiments will provide valuable tests of the theory. The Duke University HIγS facility takes one step further by employing a free electron laser (FEL) backscattered γ-ray beam and is able to probe new polarization observables. This thesis describes a first study of three-body photodisintegration of polarized ^{3}He ($\gamma^3He \rightarrow npp$) with an incident circularly polarized photon beam.

The following chapters will present the details of this study. Chapter 2 reviews the theoretical foundation of the three-body calculations as well as the GDH sum rule. Chapter 3 discusses the experiment including the HIγS facility. Chapter 4 describes the polarized ^{3}He target used in the experiment. Chapter 5 explains the detailed data analysis procedure and Chapter 6 summarizes the results from this experiment. Chapter 7 discusses the further development after the experiment and Chapter 8 presents the summary and future outlook.

2

Theory

2.1 Introduction

This chapter is devoted to the discussion of the three-body calculations and the GDH sum rule. I will start with the modern nucleon-nucleon (NN) potentials including CD Bonn and AV18, the two used in the calculations, followed by an introduction of the three-nucleon forces (3NF), such as Urbana IX and coupled-channel potential with the Δ-isobar excitation. After that, the theoretical framework based on the non-relativistic Faddeev equation and AGS equation is presented. At the end of the chapter, a simple derivation of the GDH sum rule is given, followed by the GDH sum rule on ^{3}He.

2.2 Nucleon-Nucleon Potential

The three-nucleon wave function $|\psi\rangle$ is obtained by solving the Schrodinger equation,

$$H|\psi\rangle = E|\psi\rangle. \tag{2.1}$$

For a three-body system, as shown in Figure 2.1, the conventional wisdom is that the interaction between the nucleons is described by a two-body potential V_{ij}. The

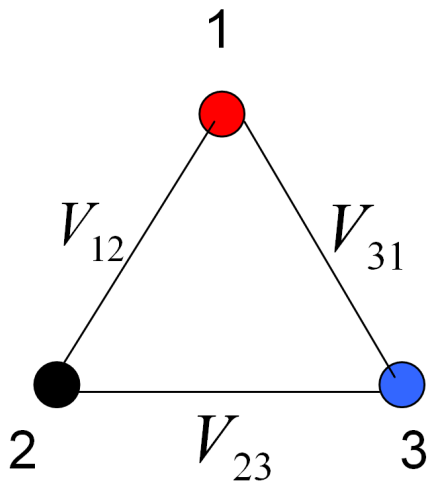

FIGURE 2.1: A picture demonstrates a simple three-nucleon system based on NN potentials.

Hamiltonian is generally written as,

$$H = \sum_{i=1}^{N} \frac{p_i^2}{2m_i} + \sum_{i<j} V_{ij}. \tag{2.2}$$

where p_i is the momentum and m_i is the mass of the nucleon.

Five modern NN potentials, based on traditional one-pion exchange (OPE) potential are developed successfully through the constraints of a significant number of NN scattering data. They are: Nijm I, Nijm II, Reid 93 [3], AV18 [4] and CD Bonn [5]. These potentials are qualitatively similar in treating NN interactions, i.e., long range one-pion exchange (r$\geq$ 2 fm), an intermediate-range attraction (1 fm$\leq$ r$\leq$ 2 fm), and a short-range repulsion (r$\leq$ 1 fm).

In the context of the NN interaction, the pion—the lightest meson—accounts for the long-range component. The OPE potential is written as,

$$V^{OPEP} = \frac{f_{\pi NN}^2}{3} m_\pi c^2 (\boldsymbol{\tau}_i \cdot \boldsymbol{\tau}_j)\{\boldsymbol{\sigma}_i \cdot \boldsymbol{\sigma}_j + S_{ij}(1 + \frac{3}{x} + \frac{3}{x^2})\}\frac{e^{-x}}{x}, \tag{2.3}$$

where m_π is the pion mass, $f_{\pi NN}$ is the coupling constant, S_{ij} is the tensor operator

and x is a dimensionless length defined as $x = m_\pi cr/\hbar$, with $\boldsymbol{r}$ the distance between the nucleons. The operator $\boldsymbol{\sigma} = \sigma_x \boldsymbol{i} + \sigma_y \boldsymbol{j} + \sigma_z \boldsymbol{k}$ is a spin operator, and $\boldsymbol{\tau}$ is the isospin operator. The tensor operator S_{ij} is defined as,

$$S_{ij} = 3(\boldsymbol{\sigma}_i \cdot \hat{\boldsymbol{r}})(\boldsymbol{\sigma}_j \cdot \hat{\boldsymbol{r}}) - \boldsymbol{\sigma}_i \cdot \boldsymbol{\sigma}_j \tag{2.4}$$

Compared with the relatively simple picture of one-pion exchange in the long range, the more complex multi-pion exchanges and the exchange of heavier mesons dominate the intermediate- and short-range. CD Bonn and AV18 are most different in treating short and intermediate range interactions.

2.2.1 Argonne V18

The AV18 potential is the newest version of the Argonne NN potential in which an electromagnetic interaction and a phenomenological short- and intermediate- range component coexist with the long range OPE potential. The short- and intermediate-range components are parameterized as,

$$V_{ST}^R(NN) = v_{ST}^c(r) + v_{ST}^{l2}(r)\boldsymbol{L}^2 + v_{ST}^t(r)S_{ij} + v_{ST}^{ls}(r)\boldsymbol{L}\cdot\boldsymbol{S} + v_{ST}^{ls2}(r)(\boldsymbol{L}\cdot\boldsymbol{S})^2. \tag{2.5}$$

Each spin and isospin state has a separate potential. The radial functions can be written as,

$$V_{ST}^i = I_{ST}^i T^2(r) + [P_{ST}^i + \mu r Q_{ST}^i + (\mu r)^2 R_{ST}^i]W(r), \tag{2.6}$$

where the average pion mass is given by $\mu = 1/3(m_{\pi^0} + 2m_{\pi^\pm})c/\hbar$. The parameters I_{ST}^i, P_{ST}^i, Q_{ST}^i and R_{ST}^i are obtained from a fit to the Nijmegen database [37, 38].

The tensor Yukawa function with the cutoff parameter α is

$$T(r) = (1 + \frac{3}{\mu r} + \frac{3}{(\mu r)^2})\frac{e^{-\mu r}}{\mu r}(1 - e^{-\alpha r^2})^2, \tag{2.7}$$

and $W(r)$ is the Woods-Saxon function, which provides a short-range core and is defined as,

$$W(r) = [1 + e^{\frac{r-r_0}{a}}]^{-1}, \tag{2.8}$$

where the shape parameters r_0, a and α are obtained from the fit.

AV18 is a nonrelativistic potential that is fit to np, pp and nn scattering data with good accuracy.

2.2.2 CD Bonn Potential

The full Bonn model was first proposed by Machleidt *et al.* in 1987 [39]. It is based on field theoretical meson-exchange and has enjoyed wide popularity since its inception. In 2001, Machleidt published a new version [40] discussing charge-dependent Bonn potential, i.e. CD-Bonn potential.

The CD-Bonn potential is a relativistic treatment of the OPE potential. It is nonlocal, an important feature that will be discussed later. The short range part of the potential is parameterized by the exchanges of heavier mesons, including ρ and ω. In principle, there are four mesons with masses below the nucleon mass: π, η, ρ, ω. But the coupling constant of the η is very small, and its contribution is negligible. In addition, two scalar-isoscalar σ_1 and σ_2 bosons are introduced to approximate the higher order two-meson exchanges: 2π and $\pi\rho$ [1]. Table 2.1 shows the parameters of mesons. Figure 2.2 shows the one-boson exchange in NN interaction.

Particle	Mass(MeV)
$\pi^{\pm}$	139.6
π^0	134.9
$\rho^{\pm}$, ρ^0	769.9
ω	781.9

Table 2.1: The mesons used in the CD Bonn NN potential model.

[1] In the one-boson exchange model, the intermediate range attraction is due to the 2π exchange

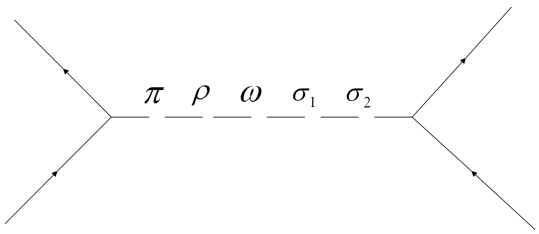

FIGURE 2.2: The lowest order contribution to the NN interaction through one-boson exchange.

Nonlocality

Nonlocality is an important concept in CD Bonn potential. The nonlocal potential generally refers to the potential acting at one point of space may depend on the value of the wave function at a different point [41]. Local representations of the OPE potential are approximations of the full relativistic treatments. The AV18 potential mentioned before employs Woods-Saxon function, which is a local version of the short-range part of the nuclear interaction. In the coordination-space calculation, these local formulations are quite successful. However, they underbind the ^{3}H. The experimental data for ^{3}H binding energy is 8.48 MeV. While AV18 and other local potentials predicted around 7.62 MeV [4], CD Bonn did a better job in predicting 8.0 MeV [5], closer to the experimental value. We can see that about half of the discrepancy comes from this nonlocality and the other half is due to some other sources [42].

2.3 Three Nucleon Force and Relativistic Effects

Although NN potentials reproduce the NN scattering database with high precision (χ^2/datum close to 1), they are not successful in predicting the trinucleon binding energies. Therefore it leads to the conclusion that there exist more complicated forces when more than two nucleons are present. Fujita and Miyazawa first introduced the

3NF [43] in 1957, which corresponds to the excitation of a Δ-isobar, the lowest excitation of the nucleon. This is due to the virtual excitation of the nucleons into isobar states and this effect is very important in the region of the Δ resonance. In Deltuva's calculation, CD Bonn is used together with the Δ isobar configuration explicitly in the nuclear wave function. Figure 2.3 shows that three nucleons interact through the two-meson exchange potentials.

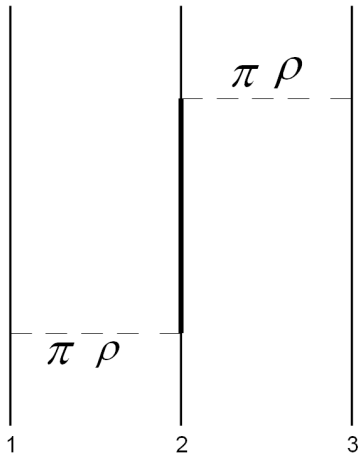

FIGURE 2.3: Three nucleons interact through the two-meson exchange potential.

The Fujita-Miyazawa term is written as a function of commutator and anticommutator,

$$V_{ijk}^{2\pi} = A_{2\pi} \sum_{cyclic} (\{X_{ik}^{\pi}, X_{jk}^{\pi}\}\{\tau_i \cdot \tau_k, \tau_j \cdot \tau_k\} + \frac{1}{4}[X_{ik}^{\pi}, X_{jk}^{\pi}][\tau_i \cdot \tau_k, \tau_j \cdot \tau_k]), \tag{2.9}$$

where {} and [ ] are anticommutator and commutator of two operators A and B, and the one-pion exchange operator is

$$X_{ij}^{\pi} = Y(r_{ij})\sigma_i \cdot \sigma_j + T(r_{ij})S_{ij}. \tag{2.10}$$

The Urbana IX (UIX) is one of the most widely used three-nucleon forces. One

term is $V_{ijk}^{2\pi}$ and the other is a phenomenological short-range repulsive term V_{ijk}^{R},

$$V_{ijk} = V_{ijk}^{2\pi} + V_{ijk}^{R}, \tag{2.11}$$

$$V_{ijk}^{R} = U_0 \sum_{cyclic} T_{\pi}^{2}(r_{ij}) \cdot T_{\pi}^{2}(r_{ik}). \tag{2.12}$$

This term is to give multiple-pion exchange and repulsive contributions. U_0 is a parameter adjusted to reproduce the correct experimental triton binding energy.

The approach of UIX is different from other models such as the Tuscon-Melbourne (TM) potential [6] and the Brazil model [44]. The TM model is based on the scattering of two pions among three nucleons. It uses the ρ-nucleon scattering amplitude from a complex interplay of a phenomenological input, current algebra and partially conserved axial-vector current. The Brazil model uses an effective Lagrangian which is invariant under chiral and gauge transformations. These two models give similar trinucleon bound state results.

The second extension to the NN potential is the relativistic correction. For example, a fully relativistic calculation using CD-Bonn potential predicts the triton binding energy to be 8.19 MeV [5], which is closer to the experimental value (8.48 MeV) compared with the result of the non-relativistic calculation (8.00 MeV).

To carry out the relativistic calculation, One has to start with the fully relativistic expression for one-nucleon electromagnetic current and make an expansion. Nonrelativistic charge is of zeroth order, nonrelativistic spatial current is of first order, whereas the leading relativistic corrections are of second (charge) and third (spatial) order. In Deltuva's calculation, RCO calculation charge operator is a sum of the zeroth and second order terms. The explicit expressions can be found in [28]. A recent paper [45] studied the sensitivity of various observables including asymmetry and differential cross section to the relativistic correction, and significant effects of the relativistic spin-orbit charge are found.

2.4 Meson Exchange Current

Nuclear current operator plays an important role in the model calculation. In plane wave impulse approximation, all nuclear current operators are treated as one-body, which is incomplete. The meson exchange currents are included explicitly as effective operators. They are simply effective two- and many-body current operators.

We can expand the charge and current operator in the following way:

$$\begin{aligned} \rho(\boldsymbol{q}) &= \sum_i \rho_i^{(1)}(\boldsymbol{q}) + \sum_{i<j} \rho_{ij}^{(2)}(\boldsymbol{q}) + ... \\ \boldsymbol{j}(\boldsymbol{q}) &= \sum_i \boldsymbol{j}_i^{(1)}(\boldsymbol{q}) + \sum_{i<j} j_{ij}^{(2)}(\boldsymbol{q}) + ... \end{aligned} \tag{2.13}$$

where the one-body operators $\rho_i^{(1)}(\boldsymbol{q})$ and $\boldsymbol{j}_i^{(1)}(\boldsymbol{q})$ are obtained from the covariant single-nucleon current [46].

Two-body currents are constructed from the nucleon-nucleon interaction and constrained by the continuity equation, which is written as,

$$\boldsymbol{q} \cdot \boldsymbol{j}(\boldsymbol{q}) = [H, \rho(\boldsymbol{q})]. \tag{2.14}$$

Take CD-Bonn for example, the nuclear interaction is mediated by π-meson and ρ-meson exchanges, as shown in Fig. 2.4. At short distances the nucleon-nucleon interaction leads to σ-like and ω-like meson-exchange currents for the isospin-independent terms and ρ-like meson-exchange currents for the isospin-dependent terms.

2.5 Theoretical Framework for Three-body Calculations

The final experimental results are compared to two sets of theoretical predictions from two groups [33, 34]. One is based on the Faddeev decomposition framework and the other uses AGS equation framework. Both techniques will be briefly introduced in this section.

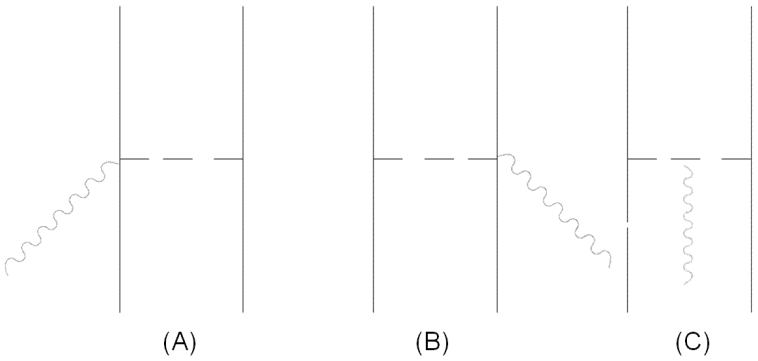

FIGURE 2.4: The diagram of the isovector currents associated with ϕ and ρ exchanges. Three components in the plot: Nucleons (solid line), ϕ and ρ mesons (dashed line), and photons (wavy line).

2.5.1 Faddeev Decomposition

The Faddeev decomposition of the three-body problem is a powerful tool to study three-nucleon system. The coordinate-space Schrodinger equation for three nucleons can be written as three separate Faddeev equations [2] with each equation involving only the interaction between one pair of the nucleons, which significantly reduces the amount of calculational requirements. In momentum space three Faddeev equations can be written as three integral equations.

$$\begin{aligned} \psi_1 &= G_0 T_1 (\psi_2 + \psi_3), \\ \psi_2 &= G_0 T_2 (\psi_3 + \psi_1), \\ \psi_3 &= G_0 T_3 (\psi_1 + \psi_2), \end{aligned} \tag{2.15}$$

where the terms ψ on the left hand side are the Faddeev amplitudes, G_0 is the propagator for three noninteracting particles,

$$G_0 = \frac{1}{E - H_0}, \tag{2.16}$$

where E is the kinetic energy and H_0 is the kinetic energy operator. The T_i can be expressed through the equation

$$T_i = v_{jk} + v_{jk} G_0 T_i. \tag{2.17}$$

The traditional procedure then is to express ψ in terms of the momenta, and relate to the standard two-body scattering operator t. But the equations are difficult to solve in the presence of three-nucleon interactions. A good way is to use the symmetry of the equation. The three-nucleon interaction can be decomposed as,

$$V_{ijk} = V_{i;jk} + V_{j;ki} + V_{k;ij}, \tag{2.18}$$

Therefore the Faddeev equation can be written as

$$\psi = G_0 T E \psi + G_0(1 + T G_0) V_{i;jk}(1 + E)\psi, \tag{2.19}$$

where the first term describes the two nucleon interaction and the second term describes the three-nucleon interaction. The operator E is the sum of the two cyclic permutations.

Skibinski's calculation

Observables in the 3N scattering at energies below 140 MeV have been calculated by Skibinski *et al.* [47, 25, 48]. The key steps are briefly summarized here. The nuclear matrix element for 3N breakup of ^{3}He is written as,

$$N_\tau^{3N} = \frac{1}{2}\langle \Phi_0 | (t G_0 + 1) P | \tilde{U} \rangle, \tag{2.20}$$

where $\langle \Phi_0 |$ is the properly antisymmetrized free 3N state (in the two-body subsystem), t is the NN matrix, G_0 is the free 3N propagator, P is the sum of a cyclical and anticyclical permutation of three particles. The state $|\tilde{U}\rangle$ follows the Faddeev-type equation:

$$|\tilde{U}\rangle = (1 + P) j_\tau(\vec{Q}) |\Psi\rangle + [t G_0 P + \frac{1}{2}(1 + P) V_4^1 G_0 (t G_0 + 1) P] |\tilde{U}\rangle, \tag{2.21}$$

where j_τ is a spherical τ component of the ^{3}He electromagnetic current operator. $|\Psi\rangle$ is the ^{3}He bound state with spin projection; V_4^1 is the part of 3NF, which is symmetrical under the exchange of nucleons 2 and 3.

Once the N_τ^{3N} amplitude is given, we can easily calculate any polarization observables through the different nuclear matrix components with spin projections.

Figure 2.5 shows the ^{3}He photodisintegration differential cross section at 90° calculated using AV18 and meson exchange current by Skibinski [34]. It is calculated for different incoming photon energies ranging from 10.6 MeV to 15.5 MeV.

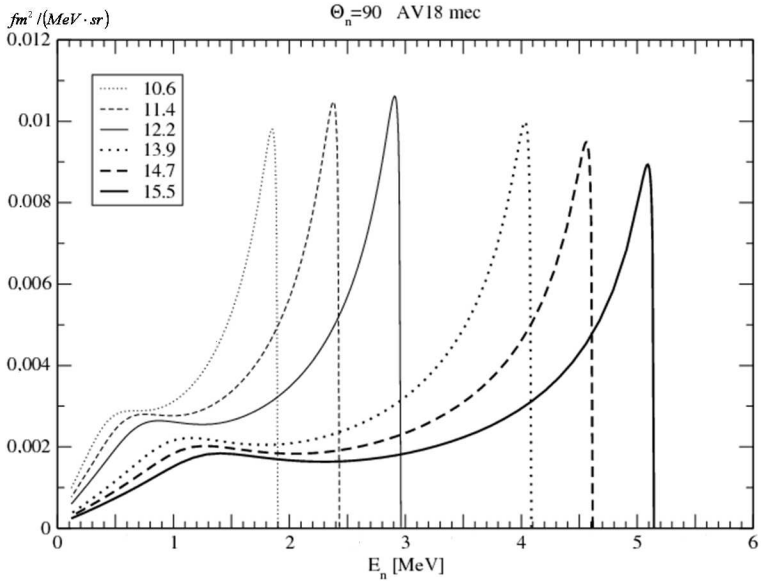

FIGURE 2.5: The inclusive differential cross section for ^{3}He photodisintegration at 90°. Six curves correspond to different incoming photon energies. The x-axis is the neutron kinetic energy and the y-axis is the differential cross section. The calculation is done by Skibinski.

2.5.2 Alt-Grassberger-Sandhas (AGS) Equation

Based on Faddeev's equations, Alt, Grassberger and Sandhas [27] derived the exact one-dimensional integral equations for the 3-body scattering problem. This more

practical approach has a structure of multi-channel two particle Lippmann-Schwinger equations [41].

The original decomposed Faddeev equations are written in a way so that the components of the wave function can be solved. Their sum is the full wave function. In the differential form, one needs to impose desired boundary conditions on the trial solutions [33]. The scattering amplitude can be extracted from the wave function. The AGS equations are formulated not for observables, but for the transition operators, and they incorporate standard boundary conditions. So AGS are Faddeev equations in the integral form in some sense. The certain (so called on-shell) matrix elements of the transition operators are scattering amplitudes from which the observables can be calculated [49]. Meanwhile, the full wave function can also be constructed from the matrix elements.

For a three nucleon system with kinetic energy and NN potential only, we have the following relation:

$$G(Z) = \delta_{\alpha\beta} G_\alpha(Z) + G_\beta(Z) U_{\beta\alpha}(Z) G_\alpha(Z), \tag{2.22}$$

where $G(Z)$ is the full resolvent expressed as

$$G(Z) = (Z - H_0 - \sum_\sigma v_\sigma)^{-1}, \tag{2.23}$$

and $G_\alpha(Z)$ is the channel resolvent expressed as

$$G_\alpha(Z) = (Z - H_0 - v_\alpha)^{-1}, \tag{2.24}$$

and $U_{\beta\alpha}(Z)$ is the AGS transition operator:

$$U_{\beta\alpha}(Z) = \bar{\delta}_{\beta\alpha} G_0^{-1}(Z) + \sum_\sigma \bar{\delta}_{\beta\sigma} T_\sigma(Z) G_0(Z) U_{\sigma\alpha}(Z), \tag{2.25}$$

where the summation on τ is from 1 to 3. $\bar{\delta}_{\beta\alpha} = 1 - \delta_{\beta\alpha}$, $G_0(Z) = (Z - H_0)^{-1}$ is the

free resolvent. $T_\alpha(Z)$ is the two-body transition matrix that obeys the Lippmann-Schwinger equation for pair α,

$$T_\alpha(Z) = v_\alpha + v_\alpha G_0(Z) T_\alpha(Z), \tag{2.26}$$

The AGS equations can be solved exactly for numerical solution. They are consistent with the corresponding Schrodinger equation and therefore provide an exact description of the quantum three-body problem. AGS are for short range potentials only.

Deltuva's calculation and Coulomb Interaction, Screening

Deltuva *et al.* published a series of papers [8, 28, 29, 26, 50] discussing their approach of calculating three-nucleon systems. The calculation used the AGS equation in momentum space and employed CD Bonn + Δ as the potential, together with Coulomb force. Figure 2.6 shows three possible reactions.

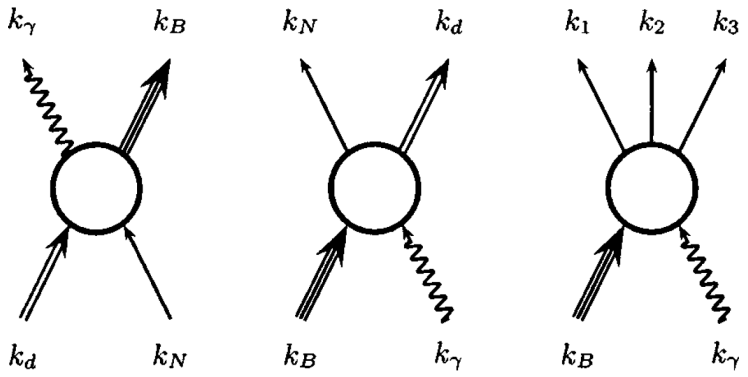

FIGURE 2.6: Schematic description of all considered three-nucleon photoreactions. Figure is from [28]. k_B (three-baryon), k_d (two-baryon), k_N (one-baryon), k_i (one-baryon), k_γ (photon) are on-mass-shell four momenta.

It is very challenging to include the Coulomb interaction between the two protons for three-body photodisintegration. This is because of the $1/r$ behavior, which doesn't qualify for the mathematical requirement of the standard scattering theory.

In a recent paper [51], Deltuva described his treatment of the Coulomb interaction, which is based on two ingredients. The first is the momentum-space integral equations and the second is the method of screening and renormalization. The new technique is employed so that the use of realistic force models and the full treatment of Coulomb interaction is possible. In the configuration space, the Coulomb potential can be written as,

$$w_R(r) = \frac{\alpha}{r} e^{-(\frac{r}{R})^n}, \tag{2.27}$$

where α is the fine-structure constant, R is the screening radius, and for finite R, the term satisfies the integral equations and after renormalization have well-defined $R \to \infty$ limits. n represents the smoothness of the screening. Deltuva used a sharper screening than the Yukawa screening, where $n = 1$. The optimal choice is that $n = 4$, which includes the exact Coulomb potential at short distances.

The inclusion of Coulomb screening follows the standard scattering theory. Coulomb interaction is screened at large distances. Figure 2.7 compares the three-body differential cross section with and without Coulomb interaction in the final state at E_γ=15 MeV and neutron scattering angle of 90°. To show the three-body force effect, the purely nucleonic results including Coulomb are also included.

2.6 GDH Sum Rule

2.6.1 A simple derivation of GDH Sum Rule

In 1966, Drell and Hearn [30] and Gerasimov [52] independently proposed a sum rule on very general physics principles.

$$\int_{\nu_{thr}}^{\infty} (\sigma_N^P - \sigma_N^A) \frac{d\nu}{\nu} = \frac{4\pi^2 \alpha}{M^2} \kappa_N^2 I, \tag{2.28}$$

where the notations have been introduced in Chapter 1. The fundamental interpretation of this sum is that any particle with a nonzero anomalous magnetic moment

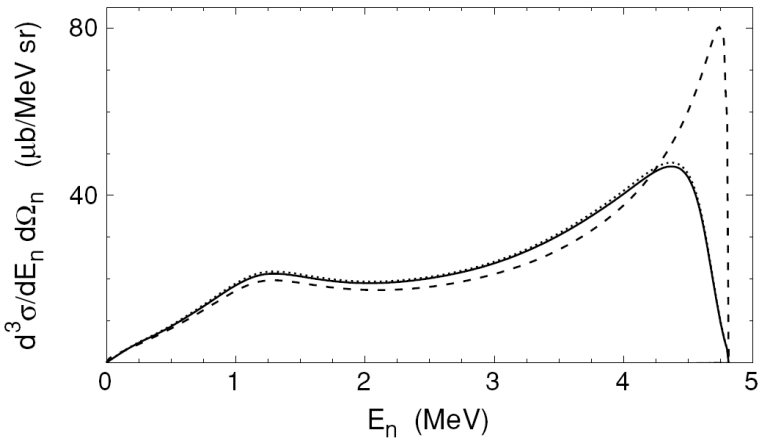

FIGURE 2.7: At an incoming photon energy of 15 MeV and neutron scattering angle 90°, the threefold differential cross section for ${}^3\vec{H}e(\vec{\gamma}, n)pp$ as a function of neutron energy E_n. Solid curve: CD Bonn + Δ isobar + Coulomb interaction. Dashed curve: CD Bonn + Δ isobar. Dotted curve: CD Bonn + Coulomb interaction. Figure is from [26].

has internal structure. This relation can be derived using the dispersion relation for forward Compton scattering and the low-energy theorem for Compton scattering.

Before proceeding to the derivation, it is necessary to specify two points. First of all, in some literature, $\sigma_{1/2}$ and $\sigma_{3/2}$ are often used, which leads to some confusion. Weller addressed this issue in [53]. The helicity has a definition of $S \cdot P/|p|$ and is only meaningful in the center of momentum (CM) frame. In the CM frame, the photon and target have opposite momenta. Therefore, their helicities are opposite when their spins are parallel. So in our case, σ_P is equivalent to $\sigma_{1/2}$ and σ_A is equivalent to $\sigma_{3/2}$. Secondly, some literatures don't have spin term in the sum rule. Since proton, neutron and ^{3}He all have spin 1/2, the coefficient on the right hand side should be 2 instead of 4.

Dispersion Relations

In the forward Compton scattering off the nucleon, the scattering angle θ equals 0. The corresponding scattering amplitude can be expressed as follows,

$$f(\nu) = f_1(\nu)\vec{e'}^{*}\vec{e} + \nu f_2(\nu) i\vec{\sigma} \cdot \vec{e'}^{*} \times \vec{e} \tag{2.29}$$

where ν is the photon energy and $\vec{e'}^{*}$ and $\vec{e}$ are the transverse polarization vectors of the incident and scattered photons, respectively. $\vec{\sigma}$ denotes the nucleon spin vector. Both f_1 and f_2 are photon energy functions and the difference is that, f_1 is the no-flip amplitude and f_2 is the spin-flip amplitude.

Under crossing symmetry transformation($\nu \to -\nu$), f_1 is an even function and f_2 is an odd function. They can be expanded into a power series,

$$\begin{aligned} f_1(\nu) &= -\frac{e^2}{m} + (\alpha + \beta)\nu^2 + [\nu^4] \\ f_2(\nu) &= -\frac{e^2\kappa^2}{2m^2}\nu + \gamma\nu^3 + [\nu^5] \end{aligned} \tag{2.30}$$

In the expansion of f_1, the first term is a consequence of gauge invariance, and is the Thomson limit for low-energy scattering. The second term comes from the contribution of electric and magnetic polarizabilities. In the expansion of f_2, the first term is proportional to the square of the anomalous magnetic moment, γ in the second term is the spin polarizability.

Using the circularly polarized photons and nucleons polarized with spin parallel or antiparallel to the photon momentum can separate these two terms f_1 and f_2. Then the optical theorem is used to relate the imaginary parts of these amplitudes to the corresponding total absorption cross sections. One can write a dispersion relation for f_2,

$$Re f_2(\nu) = \frac{2\nu}{\pi^2} \int_{\nu_{thr}}^{\infty} \frac{\sigma_A(\nu') - \sigma_P(\nu')}{\nu'^2 - \nu^2} \nu' d\nu'. \tag{2.31}$$

Low Energy Theorem

Low [54], Gell-Mann and Goldberger [55] related the zero energy limit of the spin-flip amplitude to the square of the anomalous magnetic moment of the nucleon:

$$f_2(0) = -\frac{1}{2}(\alpha/M^2)\kappa^2. \tag{2.32}$$

Therefore, we obtain the GDH sum rule:

$$I(Q^2 = 0) = -\frac{\kappa^2}{4} = \frac{M^2}{8\pi^2\alpha}\int_{\nu_{thr}}^{\infty}\frac{\sigma_A(\nu') - \sigma_P(\nu')}{2\nu'}d\nu' \tag{2.33}$$

where $Q^2 = -q^2$, in real photon case, $Q^2 = 0$; in electron scattering, $Q^2 > 0$. $\alpha = e^2/4\pi = \frac{1}{137}$. While the upper limit for the integral is infinity, the lower limit is the nuclei breakup threshold.

2.6.2 GDH Sum Rule on ^3He

Table 2.2 lists the anomalous magnetic moments and GDH integral values for proton, neutron and ^{3}He.

Target	κ (μ_N)	I (μb)
Proton	1.79	204
Neutron	-1.91	233
^{3}He	-8.37 [56]	498

Table 2.2: For proton, neutron and ^{3}He, the anomalous magnetic moments and GDH integral values. μ_N is the nuclear magneton and $\mu_N = e/2M_p$.

For example, the GDH integral value on ^{3}He is calculated as follows,

$$\int_{k_{th}}^{\infty} GDH_{^3He} = 4\pi^2 \cdot \frac{1}{137} \cdot \frac{1}{2} \cdot (-8.37)^2/(2808.4/197.3)^2, \tag{2.34}$$

where the conversion 197.3 MeV·fm =1 is used.

The GDH integral for ^3He can be written into three parts.

$$\int_{k_{th}}^{\infty} GDH_{^3He} = \int_{k_{th}}^{k_\pi} GDH_{^3He} + \int_{k_\pi}^{2-3GeV} GDH_{^3He} + \int_{2-3GeV}^{\infty} GDH_{^3He}. \quad (2.35)$$

The first part can be measured at the HIγS facility. Though the second part has not been measured directly, it is approximately 247 $\pm$ 38 μb as extrapolated from recent experimental data [31]. This experiment was an inclusive electron scattering experiment, and extracted the GDH value to $Q^2 = 0.1(GeV^2)$. This number will become more precise as newer results become available in the near future from a recent experiment completed at JLab [57]. When the energy is beyond the nucleon resonance region, the ^3He GDH integral can be written into neutron and proton integrals in the plane wave impulse approximation as:

$$\int_{2-3GeV}^{\infty} GDH_{^3He} = P_n \times \int_{2-3GeV}^{\infty} GDH_n + P_p \times \int_{2-3GeV}^{\infty} GDH_p, \quad (2.36)$$

where $GDH_{^3He}$, GDH_n and GDH_p refer to the GDH sum rule values of ^3He, neutron and proton, respectively. P_n and P_p are effective polarizations of neutron and proton in ^{3}He. Their values are 87% [58] and -2.7%, respectively.

For the proton $\kappa_p^2 = 1.79^2 = 3.21$ and for the neutron $\kappa_n^2 = (-1.91)^2 = 3.66$. The GDH sum rule predictions for ^{3}He, proton and neutron are 496 μb, 204 μb and 233.5 μb, respectively. The high energy part of the GDH integral for the proton and the neutron is -26 $\pm$ 7μb and 35 $\pm$ 11 μb [59], respectively. Therefore, the high energy part of the ^{3}He GDH integral is:

$$\int_{2-3GeV}^{\infty} GDH_{^3He} = 87\% \times 35 + 2 \times (-2.7\%) \times (-26) = 32. \quad (2.37)$$

The first term of equation (2.35) is estimated to be around 217 $\pm$ 39 μb [60].

There is an enormous strength in the first part of the integral (can be as large as 217 μb) and measurements from the two-body photodisintegration threshold to the

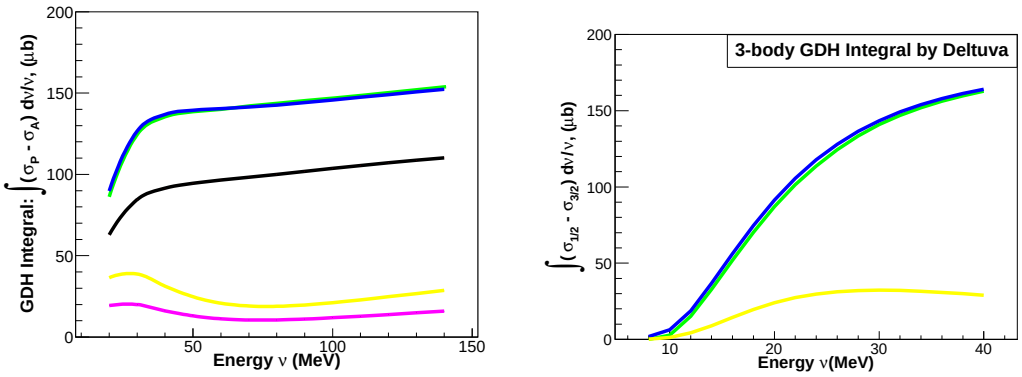

FIGURE 2.8: Theoretical predictions of the ^{3}He GDH integral from 20 MeV up to the pion production threshold (left), and the corresponding contribution due to the three-body break-up channel only (right). The curves with different colors are (from bottom to top) (left): magenta line: AV18 + implicit MEC via Siegert theorem; yellow line: CD Bonn + Siegert + MEC (h.o.); black line: AV18 + explicit MEC; blue line: CD Bonn + Siegert including RCO + MEC (h.o.); green line: CD Bonn+Δ (potential) + Siegert including RCO + MEC (h.o.). The same color designation applies to the right panel.

pion threshold can be used to provide stringent tests of the state-of-the-art three-body calculations including effective field theory calculations in the future and to help test the GDH sum rule on ^{3}He itself.

As shown in Figure 2.8, the blue, green and yellow curves are provided by Deltuva [33] and the other two are from Golak *et al.* [23]. In Ref. [28], in addition to Siegert [61], which assumes current conservation and replaces dominant parts of electric multipoles by the Coulomb multipoles, explicit MECs are used for magnetic multipoles and higher order (h.o.) terms of electric multipoles not accounted for by Siegert. In the RCO calculations the Coulomb multipoles additionally include contribution from the relativistic corrections of the charge operator.

The green line uses the CD Bonn + Δ potential, plus Siegert including relativistic charge operator (RCO), and explicit MEC (h.o.); the blue line uses CD Bonn plus the Siegert including RCO and MEC (h.o.); and the yellow line is from CD Bonn, the

Siegert theorem and MEC (h.o.). Here MEC (h.o.) means explicit MECs are used for magnetic multipoles and higher order terms of electric multipoles not accounted for by Siegert. Some details of these calculations can be found in [29]. More details about the calculations shown as magenta and black curves can be found in [23].

Compared with our simple estimation of the GDH integral below the pion threshold, state-of-the-art few-body calculations predict very different values with a wide range. In light of this large difference, it is crucial to test the theory by carrying out the GDH measurement below the pion production threshold.

3

The Experiment

3.1 Overview of the Experiment

A spin-dependent asymmetry measurement was carried out on the three-body photodisintegration of polarized ^{3}He with a circularly polarized photon beam at an incident energy of 11.4 MeV. In this experiment, the polarized ^{3}He target apparatus was set up for longitudinal polarization configuration. A neutron detection system including seven detectors was employed. The ^{3}He nuclear spin was aligned parallel and antiparallel to the incident photon momentum direction. The three-body photodisintegration process was identified by detecting the neutrons from the three-body breakup channel. This chapter is organized to address every aspect of the experiment except for the polarized ^{3}He target, which is described in Chapter 4. Section 3.2 discusses the HIγS beam. Section 3.3 briefly reviews the experimental setup. Detectors are going to be covered in Section 3.4. Electronics and Data acquisition are described in Section 3.5 and 3.6. Finally, the production runs are summarized.

3.2 High Intensity $\vec{\gamma}$-ray Source (HIγS)

3.2.1 Overview

The High-Intensity γ-ray Source (HIγS) program is the result of a collaboration between Duke Free-Electron Laser Laboratory (DFELL) and Triangle Universities Nuclear Laboratory (TUNL)[1]. This facility is an ideal place to carry out a wide range of nuclear physics experiments which need γ-rays of high flux, 100% beam polarization (circular or linear) and excellent energy resolutions. Currently, the upgrade is completed and γ-rays with energies up to $\sim$90 MeV and up to 10^8/s total intensity are available [62].

3.2.2 Basic Principles of a Free Electron Laser

Four major components of the Duke free-electron facility are a linear accelerator (Linac), a Duke storage ring (DSR), an optical klystron (OK-4), and an optical cavity, as shown in Figure 3.1.

The linear accelerator has 11 sections, three klystrons and a photoinjector. The storage ring at DFELL contains 40 dipole magnets for steering the beam and 64 quadrupole magnets for focusing the beam. The ring also has a radio frequency (RF) cavity. The optical cavity has two mirrors and they are 53.73 m apart. So the photons and electrons enter the undulator at the same time, although fine tuning of the timing is required.

The process of how FEL photons are produced is described as follows: in the linac, an electron beam is first boosted to an energy up to 280 MeV, then it is injected into the DSR. When it goes through the wiggler, which is a region of alternating magnetic fields, it is accelerated back and forth emitting radiation. The electrons also interact with the magnetic field of OK-4, the resulting photons are linearly polarized in the horizontal plane. The photons are then captured in an optical cavity. Consequent

[1] Since Sept 2008, TUNL manages DFELL.

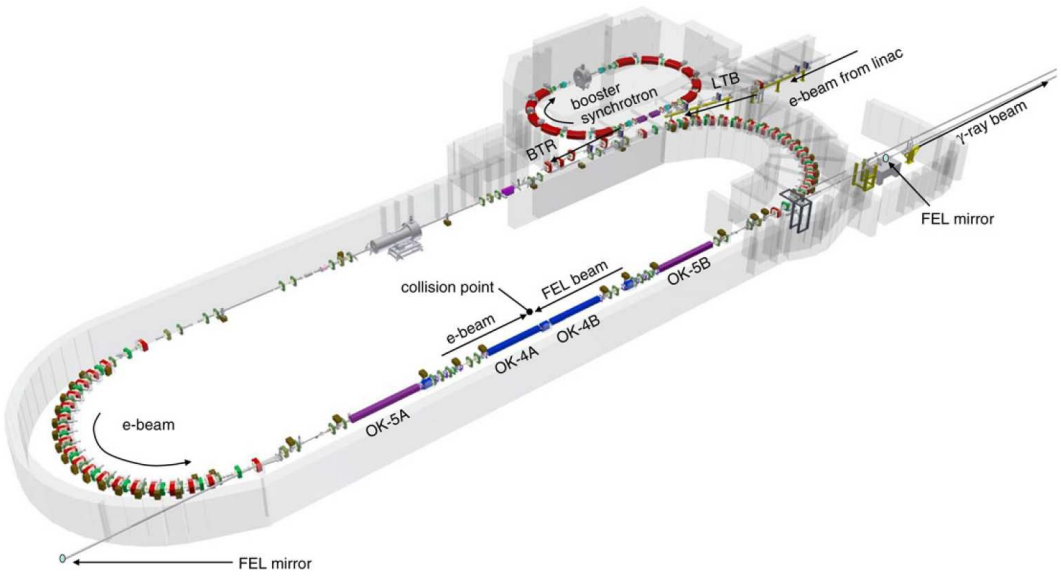

FIGURE 3.1: Schematics of the storage ring and FEL used to produce the gamma-ray beams. Plot is from [62].

electron bunches amplify the radiation. If the electron bunch and photon bunch are properly synchronized so that they enter the FEL region at the same time, the resulting radiation is coherent. The wavelength of FEL photons generated depends on the electron beam energy.

Compton Backscattering and γ-ray Production

Compared to most other facilities where conventional lasers are used, DFELL uses intra-cavity backscattering of the FEL photons in order to produce a γ-flux enhancement. The linac injects a second electron bunch which needs to reach the center at the same time as the FEL photons which are reflected from the downstream mirror with opposite direction. Then a high flux of monochromatic, 100% polarized γ-rays are produced.

According to conservation of momentum and energy, the energy of a Compton scattered photon after a head-on collision between the second bunch electron and

FEL photons is,

$$E_\gamma = \frac{E_\lambda(1+\beta)}{1+E_\lambda/E_e-(\beta-E_\lambda/E_e)cos\theta}, \tag{3.1}$$

where E_γ refers to γ-ray energy, E_λ is the energy of the incident photon, E_e the initial electron energy. $\beta = v/c$ is the ratio of the electron speed to that of the light, and θ is the scattering angle.

At the Duke FEL, $\gamma = \frac{E_e}{m_e c^2} >> 1$, therefore a simplified version of the above equation is obtained:

$$E_\gamma = \frac{4\gamma^2 E_\lambda}{1+(\gamma\theta)^2+4\gamma E_\lambda/m_e c^2}. \tag{3.2}$$

From this equation, we know that γ-ray energy depends on the angle θ.

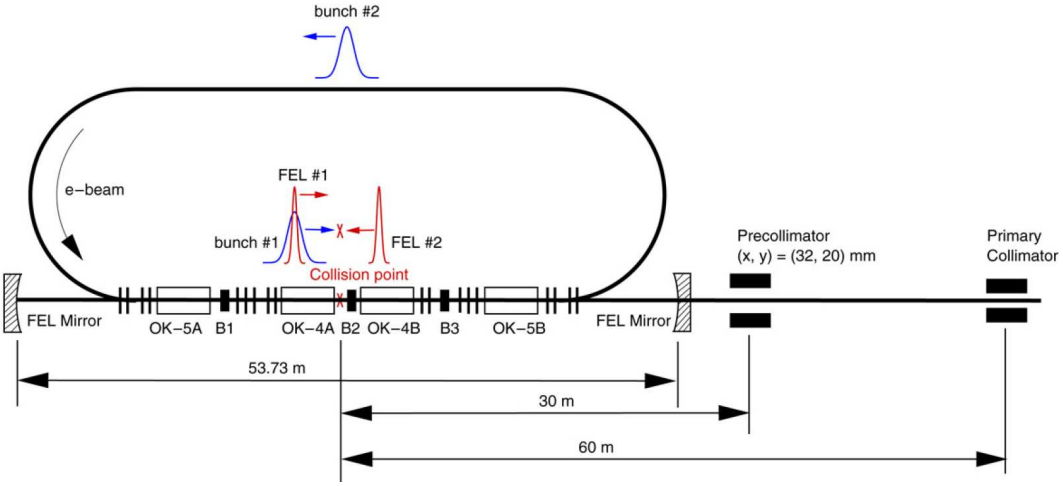

FIGURE 3.2: Layout of Duke Free-Electron Laser Laboratory after the major upgrade. Plot is from [62].

3.2.3 The Recent Upgrade of OK-5

The OK-4 system has a few limitations, one is that it only delivers γ beam with linear polarizations, but many nuclear physics experiments would require circular

polarizations, so the update of OK-5 is crucial. This update also greatly improves the γ-flux intensity as well as its energy range. The upgrade consists of three parts: a 1.2 GeV booster-injector which provides efficient injection at a certain energy, a RF Cavity and a helical undulator system OK-5.

The OK-5 system is a first distributed optical klystron. DFELL has two FEL light sources and a FEL based γ source. The two FEL light sources are capable of generating intense infrared and ultraviolet tunable radiation. Intense γ-rays are produced by internal backscattering of FEL light by electrons from the Duke storage ring.

The storage ring operates at 2.79 MHz frequency. In one-bunch mode, the electron enters wiggler every 359 ns (=1/2.79 MHz). For two-bunch mode, the requirement of γ-ray is that the second electron beam is half of the circumference from the first one, so electron enters every 179 ns (= 359 ns/2).

In summary, the HIγS beam has the following advantages. First of all, photon flux is high, which means less running time is needed. Second, it has a wide range of precisely tunable energies. Last but not least, the OK-5 results in $\sim$100% circular polarization.

Mirror and Collimator

We used the 450 nm LZH304-306 mirror during the 11.4 MeV runs [63]. A Pb collimator used during the experiment played a major role in determining the beam size and the energy spread. This collimator locates inside the collimator hut which is 60 meters away from the collision point. The beam is collimated to 22mm when it passes through the Pb collimator. We need to consider several factors in the collimator size selection: first of all, the larger the collimator, the higher the photon flux. Second, it can not exceed the diameter of the target cell, which is 30 mm, otherwise the beam would hit the glass wall and generate background neutrons. Third, a very

important factor to consider is the beam energy spread which is determined by the collimator size as well. By choosing 22 mm, a good balance is reached.

3.2.4 Beam Monitoring

Two methods were used in the experiment to monitor the photon beam flux. The first one was a 3-paddle (paddle consists of plastic scintillators.) system in the beam, as shown in Figure 3.3. The first paddle—a veto paddle—had two photomultipler tubes (PMT), a thin converter foil. The second paddle also had two PMTs, and the third only had one. The third paddle is very thick compared with the previous two. It is designed so that a constant fraction discriminator (CFD) threshold can be applied to reject single electron events. The last two function simultaneously to generate a signal proportional to the flux intensity, so it is a relative measurement. The paddle is located downstream of the Pb collimator. It is energy-dependent so the paddle efficiency varies with the energy. This paddle system provides a relative flux measurement, as such, a rough estimate of the absolute flux intensity.

The second method employed a 4.7 cm thick liquid D_2O target placed downstream of the ^{3}He target and two BC-501A neutron detectors placed at 90° on both sides. This method was based on the fact that the total cross section for $^2H(\vec{\gamma}, n)p$ was well determined [64]. Given that the electric dipole transitions dominate this reaction, the angular distribution of the neutrons is assumed to be of a $\sin^2(\theta_{\mathrm{CM}})$ form in the center of mass frame. The differential cross section at 90° is therefore the largest. The neutron rates from the two detectors provide a reasonable absolute measurement of the photon flux intensity. A more detailed description of this method can be found in [65]. Figure 3.4 shows the monitor setup. The detectors were placed 36 inch (91.4 cm) away from the center of the target. We will discuss in Section 5.6 the results of this method.

There is an additional method to roughly estimate relative photon flux from the

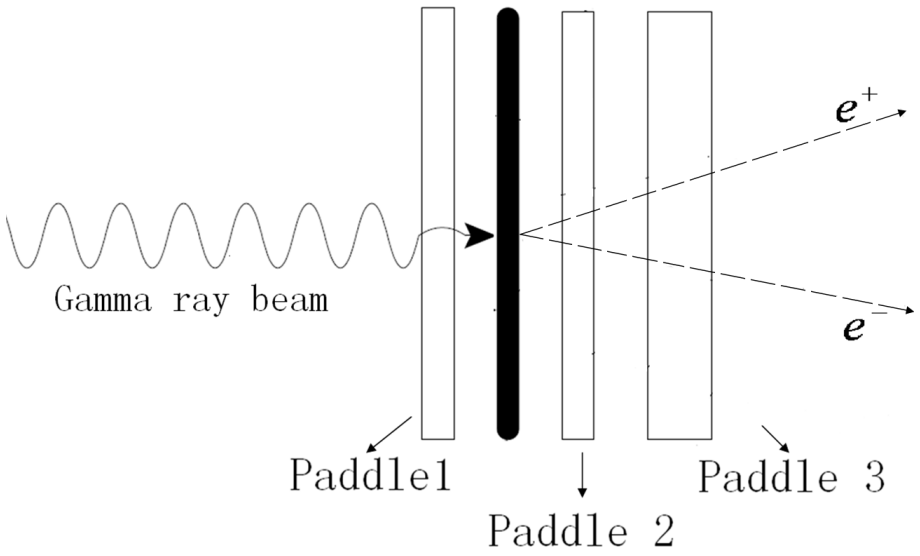

FIGURE 3.3: A schematic drawing of the 3-paddle system. Paddle 1 is on the far left. A converter locates between paddle 1 and 2. Paddle 3 is much thicker than the other two. This system is for relative flux monitoring.

EPICS (Experimental Physics and Industrial Control System) data record. Basically, the total number of gammas produced in the head-on collision is proportional to the number of electrons and the number of photons. The electron current, a bunch current of electrons, is proportional to the number of electrons. The intra-cavity power is proportional to the number of photons. Therefore, the product of the current and the power provides a very rough relative measurement of the total flux.

3.3 Experimental Setup and Targets

Fig. 3.5 shows the experimental layout in the target room. In total four target cells including a 7.6 amagats[2] ^{3}He cell were used in the experiment, and their basic information is listed in Table 2.2. I will discuss the details of the ^{3}He target in the next Chapter.

[2] 1 Amagat = 2.6894×10^{19} atoms/cm^3. It is a practical unit of number density at a pressure of 1 atmosphere and a temperature of 0° C.

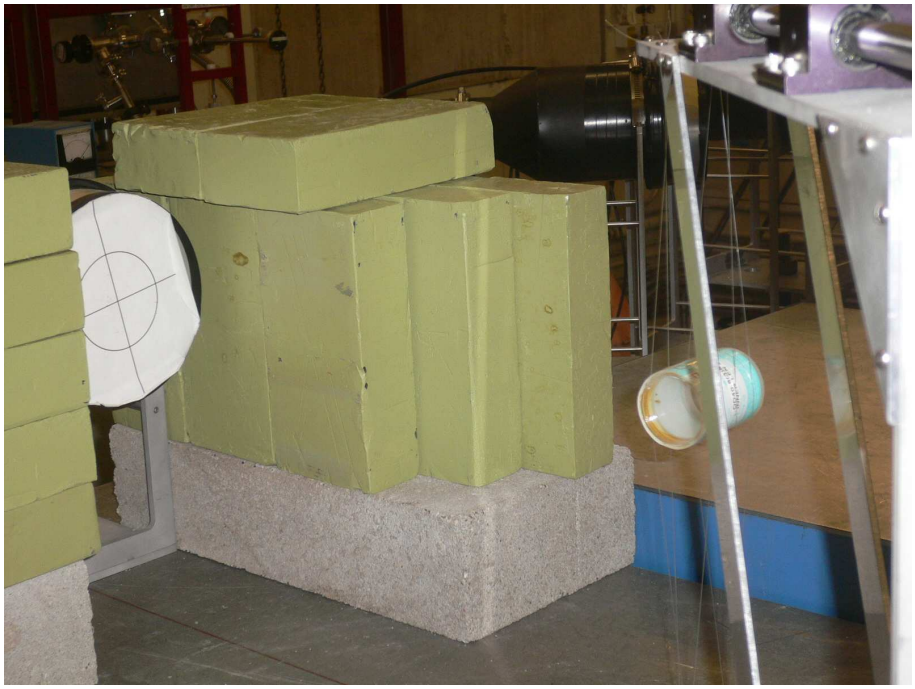

FIGURE 3.4: A picture of the liquid D_2O target taken during the HIγS run. The target has a known target thickness. Two BC-501A detectors were placed at 90° and 91.4 cm away (Only the left one was shown in the picture). Detectors were well shielded from γ-rays.

Gas	Length(cm)	Inner Diameter(cm)	Pressure
D_2	40	3.0	3808 torr
^{3}He	40	3.0	7.6 Amagats
N_2	40	3.0	100 torr
D_2O	4.7	3.8	Liquid

Table 3.1: Four targets were used in the experiment. A D_2 gas target was used at the beginning of the experiment to cross calibrate detectors. The ^{3}He target was the primary target for measurement, The N_2 reference cell was used for background subtraction and the D_2O target was placed downstream of the ^{3}He target to monitor the photon flux.

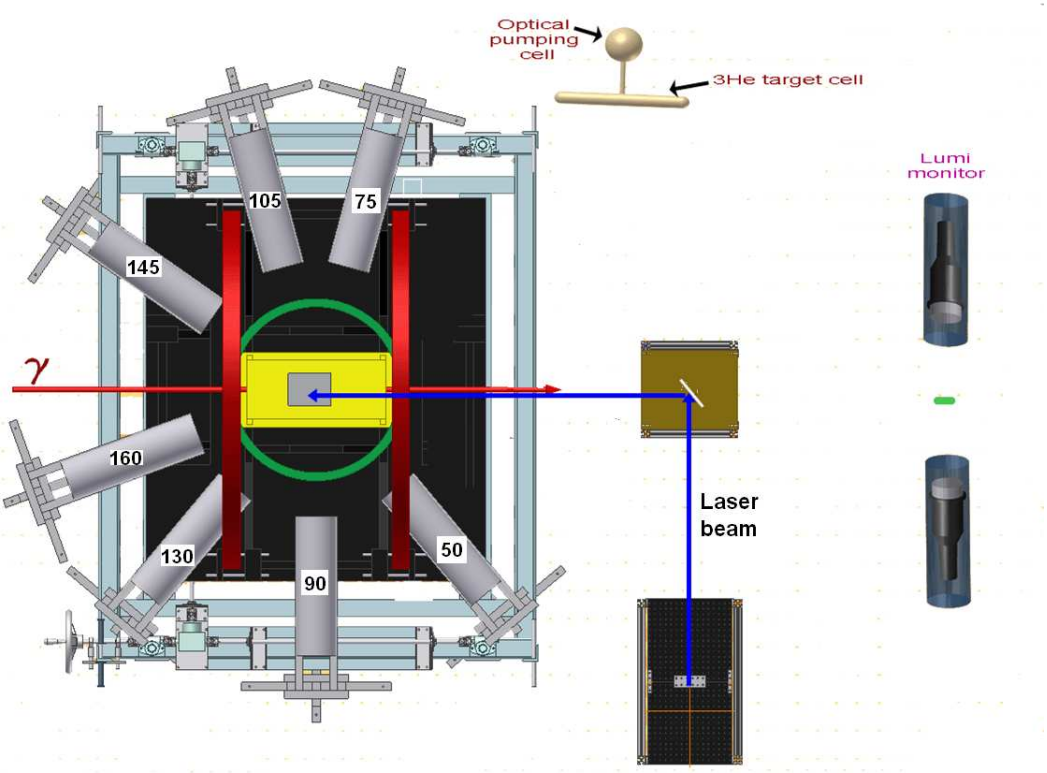

FIGURE 3.5: The schematics of the ${}^3\vec{H}e(\vec{\gamma}, n)pp$ setup. The ^{3}He target is polarized through spin exchange optical pumping, and the pumping light came from two 60 W lasers. The target was surrounded by 7 detectors with angles marked. A liquid D_2O target and two detectors were placed downstream to monitor the photon flux.

3.4 Detectors

The scattered neutrons were detected by seven liquid scintillating detectors which contained BC-501A [42] placed between 75-90 cm away and at 50°, 75°, 90°, 105°, 130°, 145°, 160° on both sides of the beam line[3]. Two other angles 20°, 35° were originally planned but later dropped due to too high rates.

[3] As seen in Figure 3.5, 50°, 90°, 130° and 160° were on the right hand side facing the downstream target room wall and the other three were on the left hand side. This two-side placement was mainly due to geometrical constraints.

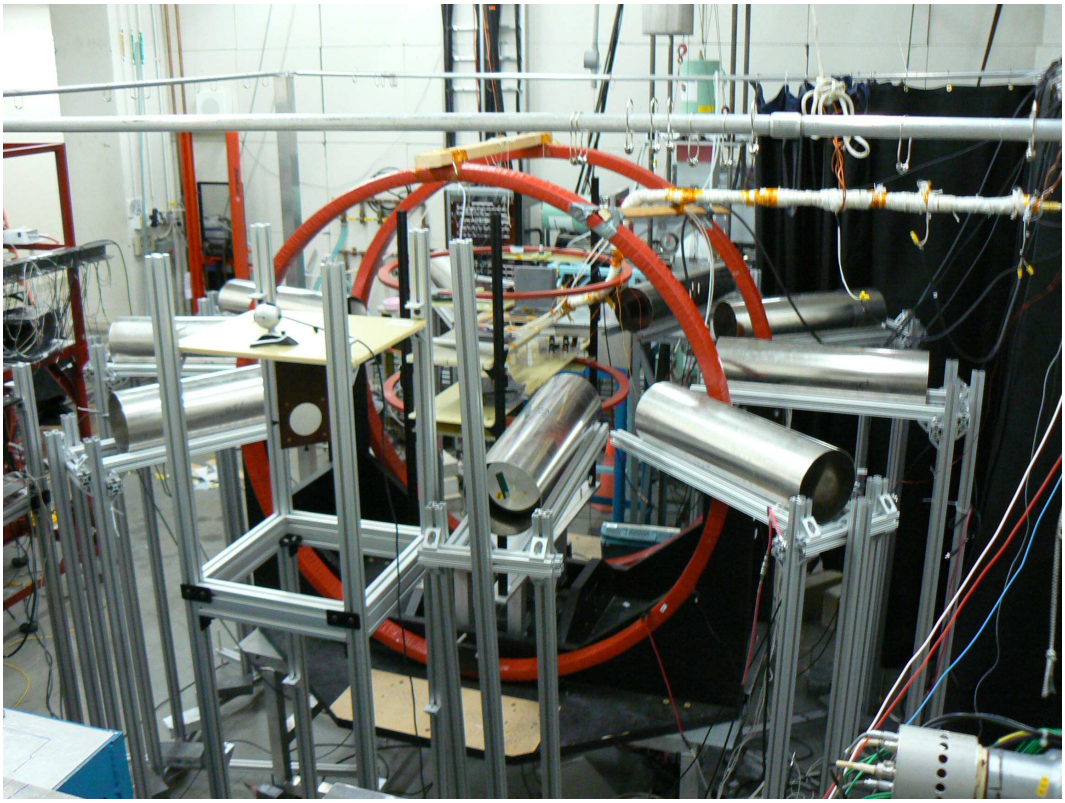

FIGURE 3.6: A picture taken during the experiment shows the experimental setup.

3.4.1 Working Principle

Liquid organic scintillator detectors were used in detecting the neutrons. Typically, hydrogen and carbon are contained inside the scintillators. The most common organic scintillation materials are aromatic hydrocarbon compounds. Neutrons interact with the hydrogen through the strong force predominantly because neutrons are neutral particles[4]. The process is as follows: neutrons strike the protons and recoiling protons then interact with the materials. The atoms and molecules are excited from their interaction with protons, then de-excite and emit light which would be collected

[4] Neutron has magnetic moment, so in principle, it can have magnetic dipole-dipole interaction with proton. However, the electromagnetic interaction has a typical cross section of 10 μb, much smaller than 10 mb, the typical cross section of strong interaction. Therefore we mainly consider strong interactions here.

by the photomultiplier tube (PMT).

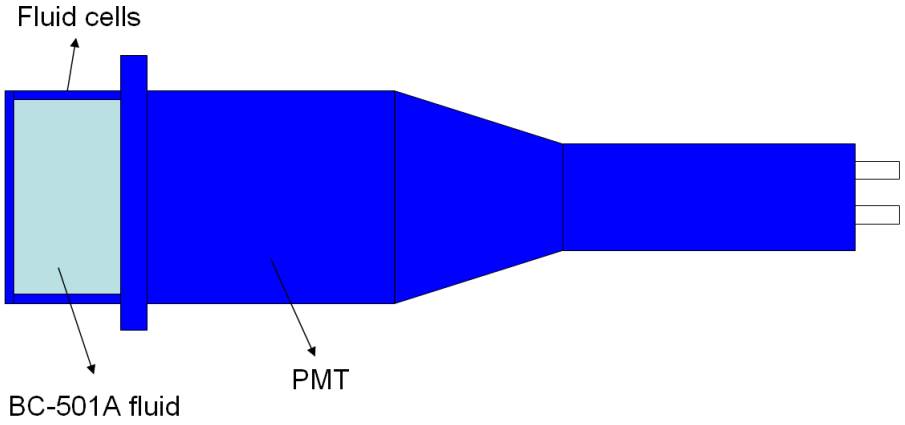

FIGURE 3.7: Liquid organic scintillator detectors contain BC-501A materials. In total nine detectors were used in the experiment, including two placed downstream for flux monitoring. The inner diameter of the fluid cell is 12.68 cm. Note that the detector is not drawn to scale.

In our experiment, detectors from the Bicron Corporation were used and they were filled with BC-501A (NE-213) fluid. The specifications of the scintillators are listed in Table 3.2. The fluid cells are aluminum cylinders equipped with a glass window on one end and an aluminum plate on the other. BC-622 reflector paint is employed to coat the interior surfaces. The cell is directly coupled to the flat-face PMT with optical grease.

Scintillator	Density (g/cm^3)	Hydrogen/Carbon ratio
BC-505	0.877	1.331
BC-501	0.901	1.287
BC-501A	0.874	1.212

Table 3.2: Properties of different liquid scintillating fluids: density of the material and hydrogen-to-carbon ratio.

A PMT is an amplifying device, optically coupled to the scintillating material to convert the emitted light into a usable signal. Through the photoelectric effect,

light strikes a metal cathode and causes electrons to be ejected. Secondary electrons are emitted and are accelerated to the next dynode. For a typical PMT, there are between 10 to 14 dynodes. At the final stage, an anode collects the charge and produces a current pulse (i.e. pulse height) which is then sent into MPD-4 pulse shape discrimination modules. A detailed description of MPD-4 module is given in Section 3.5.

A signal from the scintillator provides rich information. First of all, it provides information about the neutron energy, since light output is directly proportional to the energy deposit in region above certain thresholds. Second, it makes accurate timing measurement possible since its response and recovery time are usually on the order of nanoseconds. Third, it has particle identification characteristics. In our case, neutrons can be separated from photons due to different pulse shapes.

3.4.2 Light Output Response

Light output response plays a crucial role in determining the efficiency of the scintillator to convert ionization energy to photons. I will discuss it in details in Section 5.9.

3.4.3 Detector Placement and Shielding

The inter-play between target and detectors is an important factor which has to be taken into consideration.

On the detector side: since detectors were placed inside of a magnetic field, concerns were raised about the function of the detectors in the presence of this field. We have performed a few tests and decided to use mu metal shields.

On the target side: equipped with mu-metal shields, we did studies to determine the detector locations. While we would like to place detectors as close as possible to the target in order to improve acceptance, we had to be mindful about their effect on

the polarized ^{3}He target since magnetic materials would affect the ^{3}He polarization. Finally, we decided to place the detectors 75 cm away from the center of the target. The exceptions were the 50° and 130° detectors where they were placed at 90 cm.

Detector positions and distances to the center of the target are listed in Table 3.3.

Detector	Angle	Distance (cm)
1	50°	90
2	75°	75
3	90°	75
4	105°	75
5	130°	90
6	145°	75
7	160°	75

Table 3.3: This table lists the geometrical location information of the detectors. The angle and distance information are with respect to the center of the ^{3}He target.

3.5 Electronics

The main functions of the electronics are three-fold: amplify the signal, discriminate the particles of interest, and convert them from the detectors to a digital format, which can be read into the data acquisition system.

Signals from the photomultiplier were sent into the MPD-4 pulse shape discrimination modules, which is a key component of the electronics. It has four channels and is used for particle identification. It includes fast variable gain PMT input amplifiers; internal Constant Fraction Discriminators (CFD), the goal of which is for rising edge start signals and zero crossing for tail length detection.

MPD-4 modules have three outputs: Amplify-out, TAC-out, Gate-out, as seen from Figure 3.8. Their functions are explained as follows: Amplify-out is the integrated PMT charge output, and will go to the ADC gates; TAC-out channel corresponds to the ratio of fast to slow components of detector light output signals;

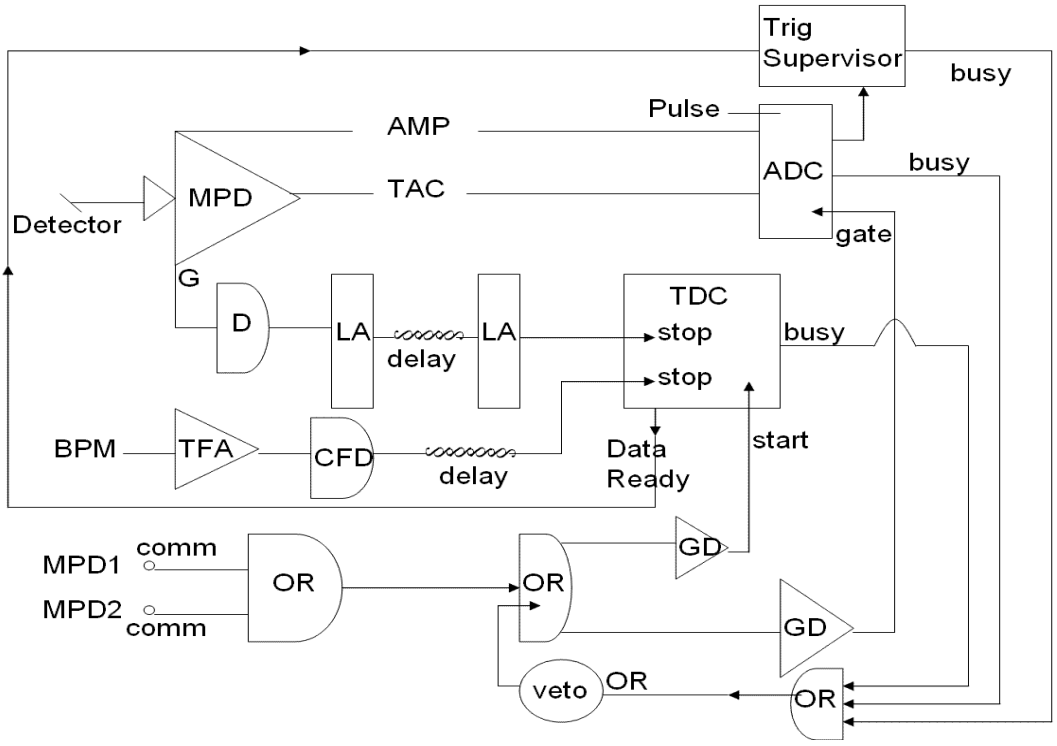

FIGURE 3.8: The block circuit diagram which shows the process of signal generation.

Gate-out means that the output signal goes through the discriminator, then a level adaptor is used to change the signal into a Nuclear Instrument Module (NIM) pulse when the signal is above the CFD threshold. It finally goes to the TDC as a stop signal. In our experiment, we used CAEN V775 32 channel multievent TDCs.

The signal from the γ beam is picked up by the Beam Pickoff Monitor (BPM) and goes to a Timing Filter Amplifier (TFA) which amplifies the pulse and gives it a shape with a short rise and decay time. A CFD is then used for a rising edge start and a zero crossing detector for the tail length. These signals then are sent to Time-to-digital converters as stop signals. In the data analysis, the stop signal from the BPM is treated as a benchmark (TDC1), all other stop signals from the detectors will need to subtract this TDC value.

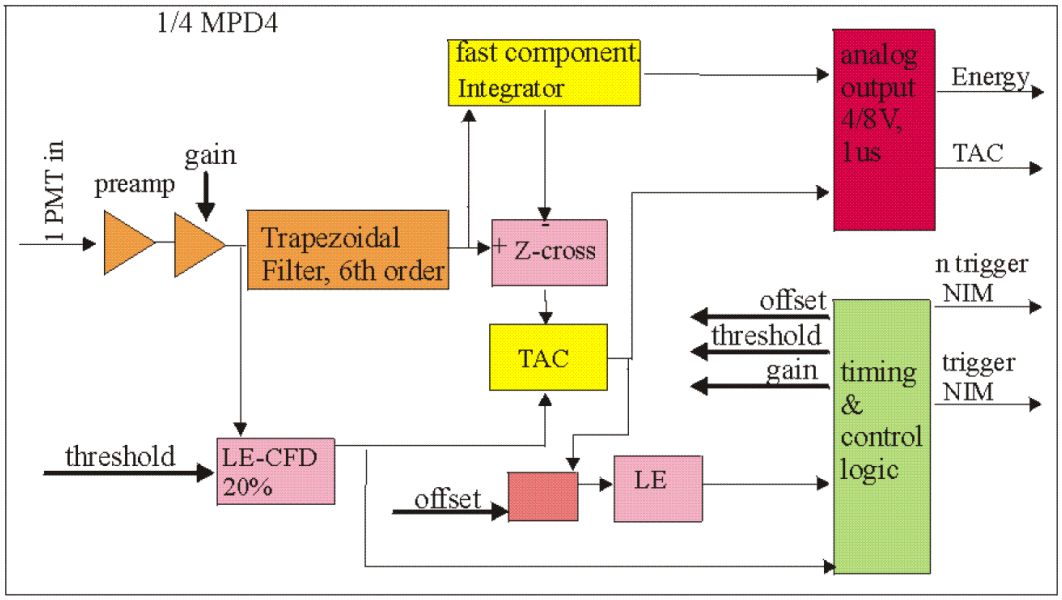

FIGURE 3.9: MPD module schematics. Figure is from [66].

Each MPD-4 module has four channels and they share one Common Trigger output. Since in total 7 detectors are used, we need to use 2 MPD-4 modules to cover them. These two common Triggers MPD1 and MPD2 are fanned together to form a common OR for all the detectors to be used to form the trigger for neutron detectors. In this case, any of the 7 channels responds, a NIM trigger is created. When system is reading, any new trigger will get a "veto". This OR is used to prevent system from crashing. They will then go through the Gate and Delay Generators (GDG) to create an ADC gate and a start signal for TDC. Dead time refers to the period of time that a data acquisition system (DAQ) is unable to take data. Thus, new signals arriving during a "dead period" are lost.

A TAC is a module that generates a pulse whose height is proportional to some length of time. We call it the PSD signal because a TAC pulse measures the time from the initial pulse to the zero crossing. TAC has a full range of 4V-8V.

CAEN V792 32 channel multievent ADC modules are used. They take Event

Trigger as the gate, one channel is for Amplify and the other channel is for TAC.

Finally, signals will go to the Trig Supervisor, which serves as the function of a writer and record all the data into a Single Board Computer (SBC).

In summary, TAC, ADC and TDC are three parameters that are read out from the raw data. In our case, TAC provides PSD information, ADC provides pulse height information and TDC provides neutron timing information.

3.6 Data Acquisition System

The digitization and counting are mainly done through CAMAC, which is an acronym for Computer Automated Measurement And Control. This open concept embraces a modular, real-time data acquisition and control system. Its main advantage includes high-speed data acquisition, wide variety of I/O interface modules and large I/O point capacity.

The connection between control terminal and experiment is called the VME crate. Various VME modules such as ADC, TDC and Scalers have been integrated. The commands are interpreted here and forwarded to other electronic devices. A single-board computer (SBC) in a VME crate controls the event readout and data flow through a VME-CAMAC interface module.

CODA, the acronym of CEBAF Online Data Acquisition (DAQ) system, was first developed at Jefferson National Laboratory, where continuous electron beam accelerator facility (CEBAF) locates. It was modified for local HIGS use. A complete DAQ system includes two parts: acquisition and analysis. Fig. 3.10 show the front panel and coda master. The main merit of CODA system is that data could be easily analyzed and replayed at a later time.

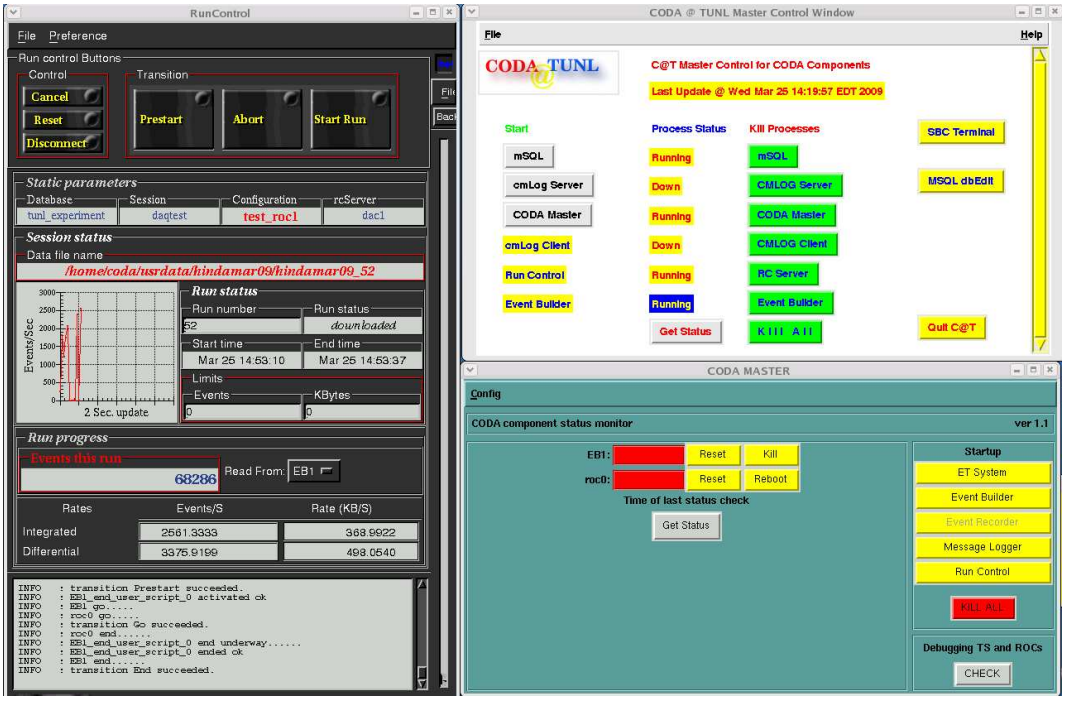

FIGURE 3.10: Left plot shows the CODA front panel, which includes start/end run buttons, and run status information. Right plot shows the CDDA master.

3.7 Run Summary

The long-awaited experiment was carried out at the HIγS facility in May 2008. We started with 14.7 MeV photon beam and observed higher-than-expected neutron events. Data were taken continuously at this energy for a total running time of 36 hours and then another 36 hours at a photon energy of 11.4 MeV. The target performance was stable throughout both running periods with an average polarization around 38% at 14.7 MeV and 42% at 11.4 MeV. There was a downtime of about a week between these energies for the replacement of a broken RF amplifier in the storage ring.

At both energies, we carried out a measurement of $^2H(\vec{\gamma}, n)p$ using a D_2 gas target. This measurement serves as the calibration purpose since the expected number of

neutrons can be calculated given the fact that the total cross section of ${}^2H(\vec{\gamma}, n)p$ is well determined [64] and the angular distribution of the neutrons is assumed to be in the form of $\sin^2(\theta_{\rm CM})$, as mentioned in Section 3.2.

At HIγS, it takes several hours[5] to flip the γ-ray beam helicity. This means each beam flip would be at the expense of the precious beam time. So we decided to flip target spin to accumulate data for both spin states. Every three hours, we made an entry to the gamma vault and physically rotated the quarter-wave plate[6].

Before we analyze the data from 11.4 MeV runs, let's discuss the polarized ^{3}He target first.

[5] This flipping time will be significantly reduced in the future.

[6] Improvements have been made since and no vault access is needed in the future running of the target at HIγS for target spin flip.

4

The Polarized ^{3}He Target System

This chapter is devoted to the discussion of the polarized ^{3}He target[1].

4.1 Overview

We first address why a polarized ^{3}He target is an effective polarized neutron target. Ideally, one would use a polarized neutron target directly for experiments to probe the structure of the neutron. However, the lifetime of free neutrons is less than 15 mins (885.7 ± 0.8 s [68]), so there is no stable free neutron target in the nature. Effective neutron targets such as the deuteron and ^{3}He are commonly used for the study of the neutron.

Polarized ^{3}He has been used extensively to study the structure of the neutron because of its unique ground state spin structure. The ground state is dominated by the S wave, in which the two proton spins cancel, and the unpaired neutron carries most of the ^{3}He nuclear spin. In order to polarize the ^{3}He nuclei, the spin-exchange optical pumping technique is routinely employed, during which the angular

[1] Most of this chapter was published in [67].

momentum is transferred from polarized photons to rubidium outshell, which is subsequently transferred to the ^{3}He nuclei through spin-exchange collisions.

4.2 Spin Exchange Optical Pumping

4.2.1 Polarizing Rubidium

In the presence of an external magnetic field, circularly polarized laser light can excite valence electrons of alkali atoms to a specific spin state because of the principle of angular momentum conservation. There are two possibilities in the case of rubidium, left-handed circularly polarized 795 nm photons can be used to excite electrons of the $m = \frac{1}{2}$ (5S) state to the $m = -\frac{1}{2}$ (5P) state, while right-handed circularly polarized light of the same wavelength can be used to excite electrons in the $m = -\frac{1}{2}$ (5S) state to the $m = \frac{1}{2}$ (5P) state. This process is commonly known as "optical pumping" and results in polarized rubidium atoms. A diagrammatic explanation of optical pumping is shown in Figure 4.1. After being excited, the Rb atom will emit a photon, and decay into either the $m = \frac{1}{2}$ (5S) with 2/3 probability or the $m = -\frac{1}{2}$ (5S) state with 1/3 probability. The probabilities are determined by Clebsch-Gordon coefficients [69].

However, one fact prevents rubidium from reaching high polarization—the emitted photons from the Rb decays are unpolarized and can be re-absorbed by other rubidium atoms. Fortunately, by introducing nitrogen—"buffer gas"—into the system, this effect could be reduced. The nitrogen allows for photon-less de-excitation by absorbing the emitted photon energy into its rotational and vibrational motion during a collision [70]. The amount of N_2 is chosen to be orders of magnitude less than the ^{3}He density and orders of magnitude more than the Rb density. Only about 5% of excited electrons decay by emitting a photon after introducing N_2.

The polarization of the rubidium vapor can be calculated via the following equa-

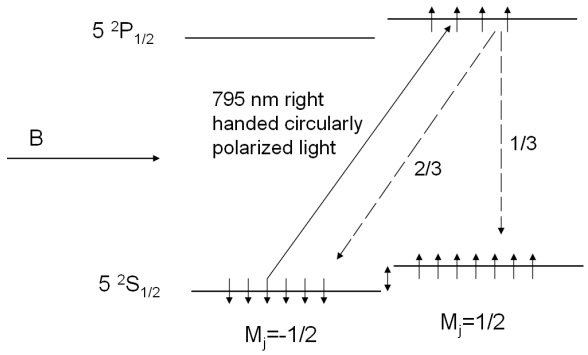

FIGURE 4.1: A diagram that explains the optical pumping process. Rb atoms in a magnetic field are exposed to right-handed circularly polarized laser light. Then the valence electron is excited from the $5S_{-1/2}$ state to the $5P_{1/2}$ state. Subsequently, the Rb atom decays by emitting a photon into either the $5S_{-1/2}$ or into the $5S_{1/2}$ state with different probabilities. By repeating this process, electrons would eventually occupy the $5S_{1/2}$ state.

tion [71]:

$$< P_{Rb} >= \frac{R}{R + \Gamma_{SD}}, \tag{4.1}$$

where R is defined through

$$R = \int \Phi(\nu)\sigma(\nu)\, d\nu, \tag{4.2}$$

where $\Phi(\nu)$ is the photon flux per unit frequency emitted from the laser and $\sigma(\nu)$ is the light absorption cross section. Γ_{SD} is the spin-destruction rate of the rubidium vapor.

It is obvious to conclude that a high value of R and a small value of Γ_{SD} will lead to high rubidium polarization, according to the equation above. While it is relatively straightforward to calculate the laser flux as a function of laser power at the absorption frequency, it is more complicated to determine the spin-destruction rate because several factors contribute to it.

The primary reason is due to rubidium transferring angular momentum to the

rotational angular momentum of other atoms during collisions. The three major rubidium collisions are: Rb-Rb, Rb-^{3}He and Rb-N_2, therefore it can be expressed as:

$$\Gamma_{SD} = k_{Rb-He}[^3He] + k_{Rb-N_2}[N_2] + k_{Rb-Rb}[Rb], \tag{4.3}$$

where for each collision Rb-i, k_{Rb-i} denotes the spin destruction rate constant accordingly. The gas density for a typical ^{3}He target cell is:

$$[^3He] = 8.0\ amg = 2.15 \times 10^{20}\ cm^{-3}. \tag{4.4}$$

The N_2 pressure at room temperature is about 100 torr.

$$[N_2] = 100\ torr = 0.123\ amg = 3.31 \times 10^{18}\ cm^{-3}. \tag{4.5}$$

Rb density is given by the following empirical formula [72],

$$[Rb] = (10^{26.178-4040/T}/T), \tag{4.6}$$

where T is in the unit of K, and Rb density is in the unit of cm^{-3}.

In our experiment, the oven temperature is at T=510°K (237°C). Plug this number into the expression of Rb density, we get

$$[Rb] \approx 3.54 \times 10^{15} cm^{-3}. \tag{4.7}$$

Spin destruction constants can be found in Ref. [73]:

$$k_{Rb-He} \sim 2 \times 10^{-18}\ cm^3/s \tag{4.8}$$

$$k_{Rb-Rb} \sim 8 \times 10^{-13}\ cm^3/s \tag{4.9}$$

$$k_{Rb-N_2} \sim 8 \times 10^{-18}\ cm^3/s \tag{4.10}$$

Therefore we obtain the spin destruction rate

$$\Gamma_{SD} = 430_{Rb-He} + 25_{Rb-N_2} + 2800_{Rb-Rb} \sim 3255\ s^{-1}. \tag{4.11}$$

4.2.2 Spin exchange between ^{3}He and Rubidium

Rubidium can transfer its electron polarization to the nucleus of a ^{3}He atom through a hyperfine-like interaction. This spin-exchange process between Rb and ^{3}He has a small contribution compared to the total number of Rb-He collisions; consequently, only approximately 3% of polarized rubidium atoms lose their polarization through a spin-exchange process with ^{3}He. This makes the polarization of ^{3}He through rubidium spin-exchange an inherently inefficient process.

The time evolved expression of ^{3}He polarization is

$$P_{^3He}(t) =< P_{Rb} > \frac{\gamma_{SE}}{\gamma_{SE}+\Gamma}(1-e^{-(\gamma_{SE}+\Gamma)t}), \tag{4.12}$$

where γ_{SE} is the Rb-^{3}He spin exchange rate per ^{3}He nucleus, Γ is the ^{3}He polarization destruction rate.

Γ is the quantity which best determines the ^{3}He polarization. The smaller the Γ is, the higher the ^{3}He polarization would be as shown in Eqn. 3.13. It can be decomposed into the following four terms:

$$\Gamma = \Gamma_{Dipole} + \Gamma_{Wall} + \Gamma_{\bigtriangledown B} + \Gamma_{BeamDepol}, \tag{4.13}$$

where Γ_{Dipole} means depolarization from ^{3}He-^{3}He dipole collisions, Γ_{Wall} is depolarization due to interactions with the glass wall, $\Gamma_{\bigtriangledown B}$ is depolarization from magnetic field gradients and $\Gamma_{BeamDepol}$ is depolarization by the photon beam.

Γ_{Dipole} is the dominant factor in a high-density ^{3}He system. It is the result of spin-destructive ^{3}He-^{3}He collisions. Another important process in polarization relaxation is the ^{3}He interactions with the glass cell wall. There are multiple reasons that the cell wall causes depolarization. First is the out-gassing of paramagnetic gases like O_2 from the wall when the cell is heated; second is the paramagnetic material like Rb_2O on the surface of the cell walls; the third is the increasing sticking time of ^{3}He

to the surface of the wall due to microscopic fissures in the glass. For different cells, Γ_{Wall} varies significantly. A good cell can have a $\Gamma_{Wall} < 1/200\ hrs^{-1}$, a bad cell can have a $\Gamma_{Wall} > 1\ hrs^{-1}$.

Magnetic field gradients can contribute to depolarization. The formula is from Ref. [74],

$$\Gamma_{\bigtriangledown B} = D\frac{|\bigtriangledown B_x|^2 + |\bigtriangledown B_y|^2}{B_z^2}, \tag{4.14}$$

where B_z is the magnitude of the holding field, $\bigtriangledown B_x$ and $\bigtriangledown B_y$ are the gradients of the two transverse field components, and D is the self-diffusion coefficient: $D \approx 0.28\ cm^2/s$.

Using the magnetic field gradient values we measured in our target system, we have

$$|\bigtriangledown B_x|^2 = (\frac{\partial B_x}{\partial x})^2 + (\frac{\partial B_x}{\partial y})^2 + (\frac{\partial B_x}{\partial z})^2 \tag{4.15}$$

$$= (4\ mG/cm)^2 + (1\ mG/cm)^2 + (20\ mG/cm)^2 = 417\ (mG/cm)^2 \tag{4.16}$$

$$|\bigtriangledown B_y|^2 = (\frac{\partial B_y}{\partial x})^2 + (\frac{\partial B_y}{\partial y})^2 + (\frac{\partial B_y}{\partial z})^2 \tag{4.17}$$

$$= (5\ mG/cm)^2 + (3\ mG/cm)^2 + (30\ mG/cm)^2 = 934\ (mG/cm)^2 \tag{4.18}$$

For a holding field value of $B_z = 25\ G$, we then obtain $\Gamma_{\bigtriangledown B} = 459\ hr^{-1}$, so it is negligible.

The last factor that can contribute to the ^{3}He depolarization is the photon beam. This effect was studied by comparing the maximum polarization of the ^{3}He target "Linda" with and without photon beam. As shown in Figure 4.2, photon beam has a negligible effect on target polarization.

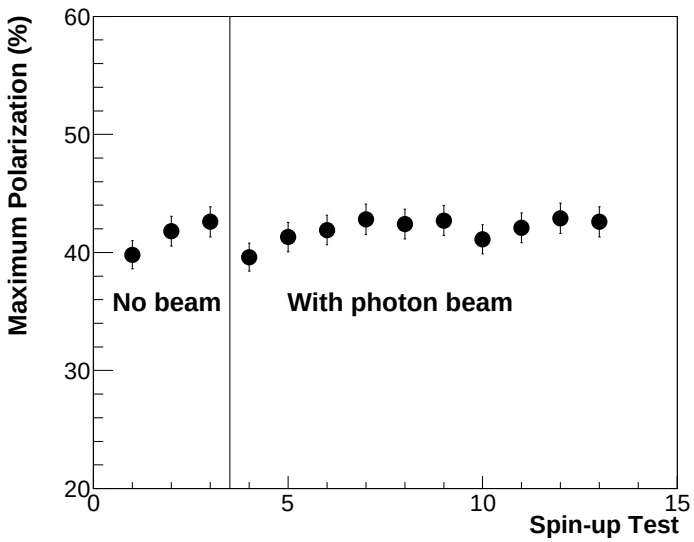

FIGURE 4.2: Comparison of the maximum polarization of the ^{3}He target "Linda". The first three tests were taken in French Science Lab without any photon beam, and the rest were conducted at FEL when photon beam was present. The conclusion is that photon beam has a negligible effect on target depolarization.

However, a more efficient hybrid approach to polarize ^{3}He atoms, by adding vaporized potassium to the pumping chamber, was first proposed by Happer *et al.* [75]. The advantage of this method is as follows: Rb atom is polarized through the standard optical pumping, then it transfers the angular momentum to the potassium atom. The spin-exchange collision between ^{3}He and K atoms will subsequently polarize ^{3}He atoms. The likelihood of spin-exchange between K-^{3}He is significantly higher than that of rubidium to ^{3}He. Princeton Group [76] was able to extract γ_{SE} to be around 2% at about 175°C, which is the typical optical pumping temperature for Rb. In contrast, the typical value of γ_{K-^3He} is around 25%. Therefore one would expect the SEOP process for hybrid cells to be more efficient than for a Rb-only-cell. Such improvement has been demonstrated by an extensive study carried out by W.C. Chen *et al.* [77]. The direct spin exchange between potassium and ^{3}He has also been realized by the Caltech Group [78].

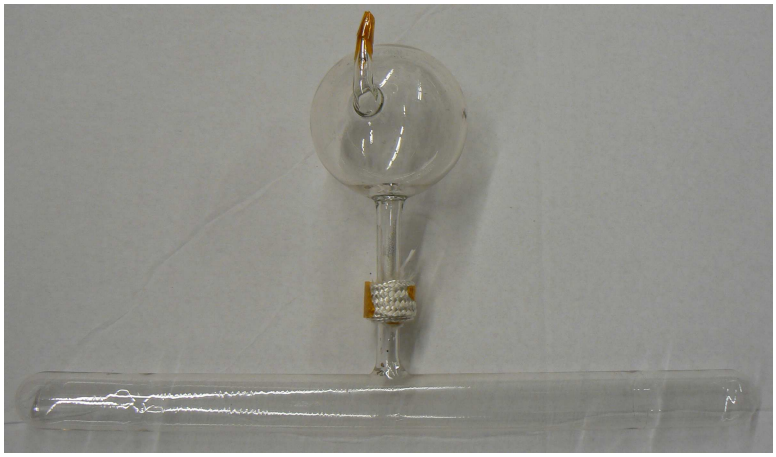

FIGURE 4.3: The ^{3}He cell used in the experiment. It is a double-cell system: the upper pumping chamber and lower target chamber. The pumping chamber has a diameter of 9 cm and the target chamber has a diameter of 3 cm, a length of 40 cm. A transfer tube connects the two chambers.

4.3 Experimental Setup

At the center of the target system is a double-chambered GE180 glass cell which contains the ^{3}He gas. The cell's upper chamber, referred to as the pumping chamber, is where optical pumping and the spin exchange between alkali atoms (Rb or Rb and K) and ^{3}He take place. Light from the diode lasers is focused onto this part of the cell. The pumping chamber sits in an oven which is heated up to 170-175°C for Rb-only cells or 230-240°C for Rb-K cells, so that the vapor pressures of Rb and K are optimized for spin-exchange. The target chamber is typically 40 cm long with an inner diameter of 3.0 cm to accommodate a 2.2 cm diameter photon beam. The volume of the pumping chamber is similar to the volume of the 40 cm target chamber, around 250 ml. The entrance and exit windows of the cell are 0.2-0.3 mm thick at the central point with some thickening near the side walls. The cell side walls are 1-2 mm thick.

The oven is heated by a flow of compressed air through two 3/4" diameter 750 W air process heaters. The oven is made of alumino-silicate machinable ceramic and is

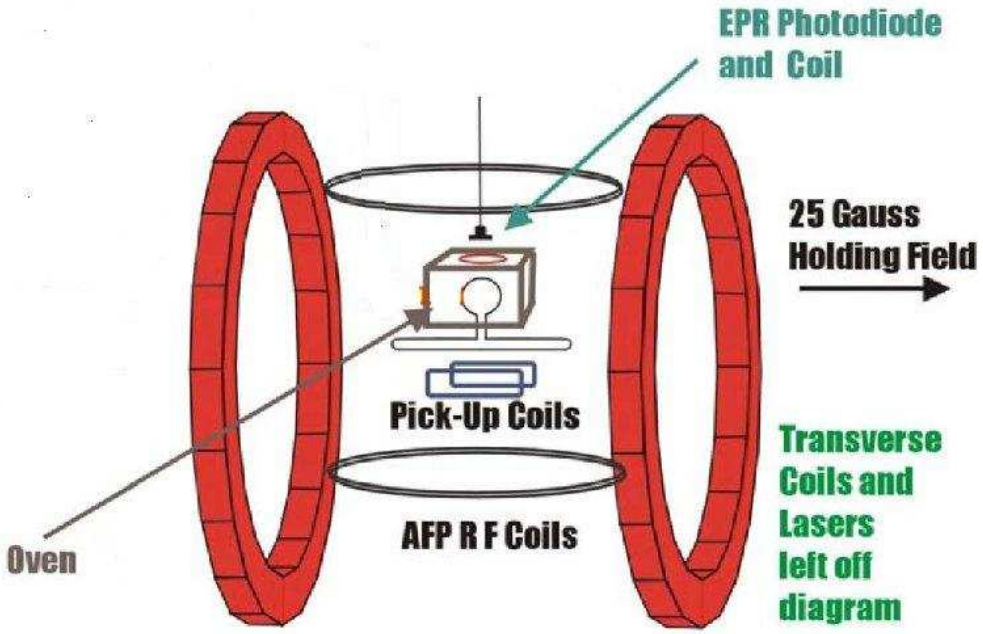

FIGURE 4.4: The equipment set up for AFP and for NMR polarimetry.

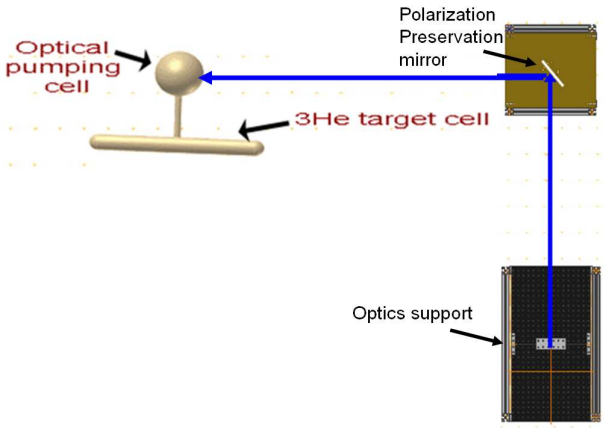

FIGURE 4.5: A schematic drawing of the laser beam path. Detailed schematics of the optics is shown in Figure 4.6.

held together by bronze screws. Since the target is to be polarized longitudinally in this work, there is a 4" window on the side of the oven coated with an anti-reflection coating acceptable for the 794.7 nm light. There is also a small window on another side of the oven for the Electron Paramagnetic Resonance (EPR) photo-diode.

The target cell sits in a holding field with a magnetic field gradient of < 10 mG/cm at 25 G. This holding field is generated by a pair of 58" diameter Helmholtz coils that are oriented so the field is parallel to the ground. These Helmholtz coils are powered by a single water-cooled 1.25 kW DC power supply. The output current of the power supply is controlled by a programmable Tektronix AFG 310 function generator.

The laser light is provided by two Coherent FAP system diode lasers. Each laser has a 2-diode package that feeds into a single output optical fiber. Each diode package has a nominal maximum power of 30 W; therefore, the two lasers combined provide 120 W total laser power. The laser spectrum has a FWHM of around 2 nm. About 70-90% of laser light is incident onto the pumping cell of our target.

Each laser has its own set of focusing and polarizing optics, as shown in Figure 4.6. The emitted laser light has a 13° divergence from the optical fiber and is focused by a spherical plano-convex lens. The light is then sent through a polarizing beam splitter. The light going straight through the beam splitter is reflected 90° by a mirror and then through a quarter-wave plate. The light reflected 90° through the beam splitter travels through a quarter-wave plate then onto a mirror and then through the same quarter-wave plate. This rotates the polarization direction of the light by 90° where it is then going straight through the beam splitter into a quarter-wave plate. Both beams are focused on a 4" polarization-preserving mirror that is at a 45° angle at the downstream of the oven. The diameter of the beam spot incident on the target is around 3.7", about 10% larger than the diameter of the pumping chamber, but slightly smaller than the size of the window.

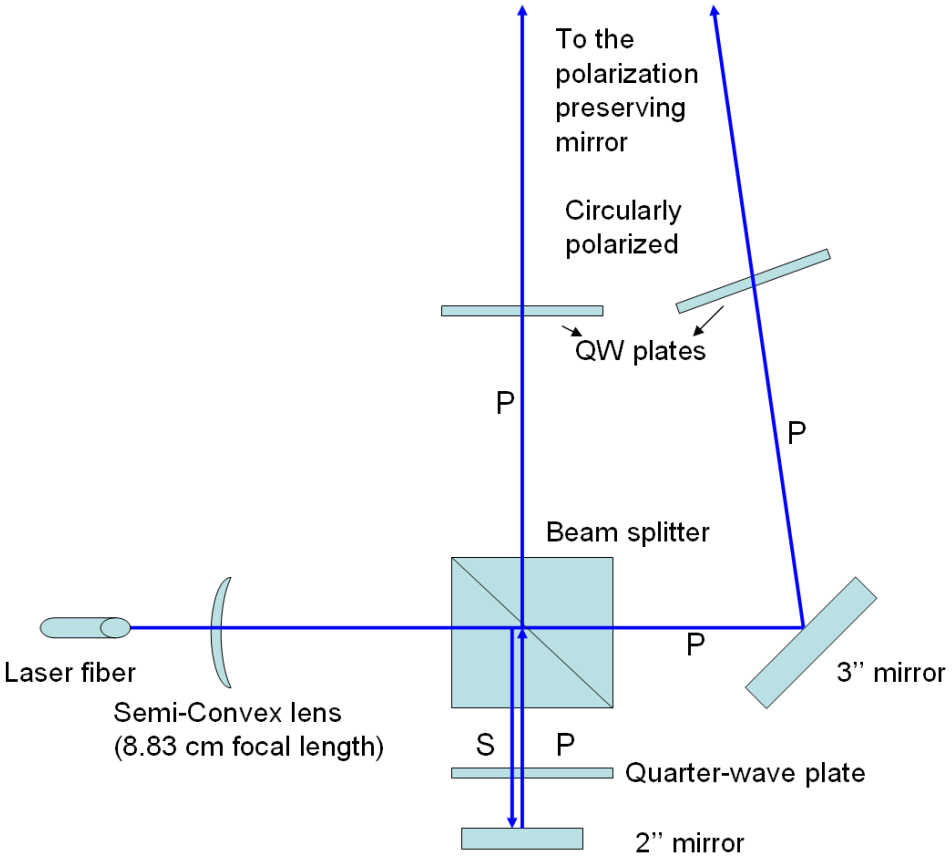

FIGURE 4.6: The layout of the optics. Beam first passes through the lens, and is split into S and P waves by the beamsplitter. S-wave goes through a quarter-wave (QW) plate and is reflected by the 2" mirror, then goes through the same QW plate and the beamsplitter and another QW plate before reaching the polarization preserving mirror. P-wave passes through a QW plate and then is incident on the polarization preserving mirror.

4.4 Measuring the Target Polarization

4.4.1 Polarimetry

The polarization of the target is determined by two independent polarimetry systems. The first is NMR-AFP (Adiabatic Fast Passage), in which the magnetic holding field is increased adiabatically to go through the Larmour resonance then swept back to reverse the polarization back to the original direction. The rate at which the

holding field is ramped has to be slow enough to meet the adiabatic condition, but fast enough so that the sweep rate is significantly faster than the relaxation rate ($1/T_1$ and $1/T_2$), where T_1 and T_2 are the longitudinal and transverse relaxation times, respectively. T_1 is also called spin-lattice relaxation time, a time constant to describe the rate at which spin's longitudinal part recovers when exposed to an external magnetic field. The time it takes to recover $1 - 1/e \sim 63\%$ of the initial polarization is defined as T_1. Similarly, T_2 is also called spin-spin relaxation time, a quantity measuring the average time that spin's perpendicular component decays. The time it takes to drop to $1/e \sim 37\%$ of the initial polarization is defined as T_2. A detailed description of T_1 and T_2 is in [79].

A brief review of the NMR-AFP principle is stated here. The magnetic moment of a free particle of spin $\vec{I}$ is,

$$\vec{M} = \gamma \vec{I}, \tag{4.19}$$

where γ is the gyromagnetic ratio. For proton, $\gamma = 4.26 \times 2\pi$ kHz/G, for ^{3}He, $\gamma_h = 3.24 \times 2\pi$ kHz/G. When placed in an external magnetic field, the magnetic moment is described by the equation of motion,

$$\frac{d\vec{M}}{dt} = \gamma \vec{M} \times \vec{B}. \tag{4.20}$$

Now assume an RF field $\vec{B_1} = 2B_1 cos(\omega t)\hat{x}$ is applied. We can decompose it into two rotating fields,

$$\vec{B_1} = (B_1 cos(\omega t)\hat{x} + B_1 sin(\omega t)\hat{y}) + (B_1 cos(\omega t)\hat{x} - B_1 sin(\omega t)\hat{y}). \tag{4.21}$$

These are two magnetic fields rotating at the frequencies $\vec{\omega} = \omega\hat{z}$ and $\vec{\omega} = -\omega\hat{z}$. In the rotating frame, one is static and the other is at a frequency of 2ω. Since the frequency 2ω is off-resonance, it can be neglected. The effective field therefore can

be written as,

$$B_{eff} = (B_0 - \frac{\omega}{\gamma})\hat{z} + B_1\hat{x}. \tag{4.22}$$

If we ramp the holding field $B_0\hat{z}$ from below the resonance $\vec{\omega}/r$ to above it, there is a time when the z component of magnetic field becomes zero and only x component exists. At this resonance, the magnetic moment of ^{3}He atoms induces a signal in the pickup coil, which is proportional to the ^{3}He polarization. This signal is also perpendicular to the holding field and the RF field. Then holding field goes from above the resonance to below it. In this process, spin is flipped twice. A more detailed description of the AFP-measurement can be found in [80].

The ^{3}He polarization is calibrated by the known NMR water signal. The EPR technique extracts the polarization of ^{3}He by measuring the frequency shift in the electron paramagnetic resonance (EPR) of rubidium when the spin direction of the ^{3}He is flipped. The systematic uncertainty in the determination of the target polarization is reduced when both techniques are employed. More details on NMR and EPR are presented in Section 3.5.

4.4.2 NMR and AFP set-up

In our system, the AFP technique is applied by sweeping the magnetic holding field from 25 G to 32 G and then back to 25 G, while a perpendicular 91 kHz RF field is applied. The holding field is swept by triggering a programmable signal shape in the holding field function generator. The RF field is created by a pair of 31" diameter coils driven by a HP3325A function generator whose signal is amplified by a 150 W AG Series RF amplifier made by T & C Power Conversion. Additionally, there is a custom-built impedance matching transformer between the amplifier and the coils. The RF field generated at the target cell has an amplitude of around 90 mG.

The NMR signal is detected by a pair of pick-up coils, which are made of 100-

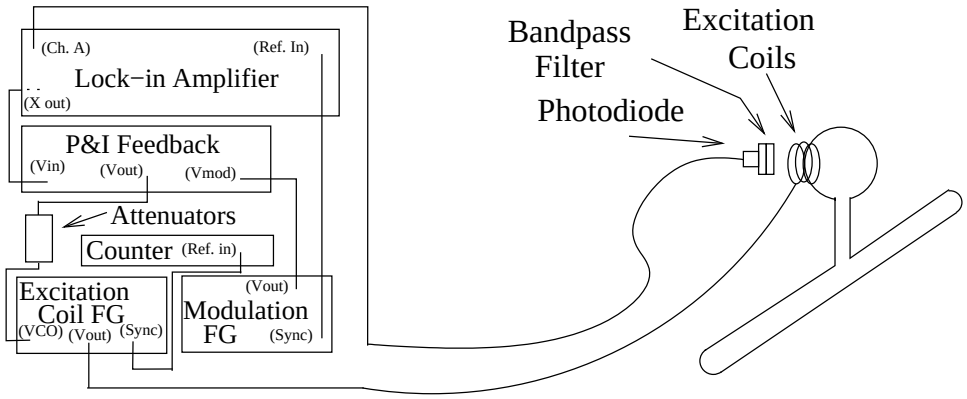

FIGURE 4.7: The EPR polarimetry set-up.

turn coils using copper wire wrapped around a 3 cm by 15 cm acrylic frame. The coils are connected to a Stanford Research Systems Model SR560 pre-amplifier. The pre-amplifier is only used to add the two signals from the two coils during the ^{3}He NMR measurement; however, the pre-amplifier can be set to have a gain of 100-500 for NMR water measurement. The output of the pre-amplifier is sent into a Signal Recovery 7225 DSP lock-in amplifier. The reference frequency comes from the function generator producing the 91 kHz RF field. All electronic equipments can communicate with the target control PC to record the data.

4.4.3 EPR Measurement Technique

Measurement of the shift of the electron paramagnetic resonance frequency of the rubidium valence electron before and after AFP is a demonstrated way of measuring the polarization of a ^{3}He sample [81, 82, 83, 84]. Measurement of EPR shift, $\Delta\nu$, was performed by observing the D2 fluorescent light emitted by decaying rubidium atoms. A small EPR coil is placed on the side of the pumping chamber to induce the transition of rubidium atoms from a non excitable state to an excitable state. The frequency of the resonance is affected by the ^{3}He polarization.

The system for EPR starts with a small 2" diameter RF excitation coil that is

attached to the cell with high-temperature RTV. The excitation coil is driven by a HP3314A function generator. The 780 nm light from the EPR is detected by a photodiode with a bandpass filter to attenuate the 794.7 nm light from the laser. The photodiode is fed into the Signal Recovery 7225 lock-in amplifier. The function generator connected to the excitation coil is modulated at 200 Hz by a HP 3312 A function generated through the HP 3314A voltage-controlled oscillator (VCO) input. The modulation signal from the HP 3312 A is fed through a feedback box which adds a DC offset to the VCO based on the size of the signal in the photodiode. This feedback box, which was developed in previous experiments [85, 86], allows the output frequency of the excitation coil to be continuously locked to the resonance. The output frequency is measured by an Agilent 53132A frequency counter. The equipment used for EPR polarimetry is shown in Figure 4.7.

4.5 Polarization Results

4.5.1 Measurements of Pump-up and Relaxation Time

For each target cell, a complete set of tests consist of the following steps: first, use SEOP technique to pump up the cell, after the ^{3}He NMR signal saturates, an EPR measurement is conducted so that two independent measurements can provide better insight to determine the accuracy of the polarization. A relaxation measurement will then be performed.

The pump-up measurement is the core of the complete test. Our systematic study shows the laser power, laser spectrum and oven temperature are the three major factors that determine the ^{3}He NMR signal height. The laser tuning, optics alignment and maintaining a stable oven temperature are essential. The relaxation measurement is carried out by turning off the laser and heater and monitoring the NMR signal as a function of time at room temperature. The data are taken every 3 hours. To calculate the lifetime of the cell, the AFP loss rate needs to be taken

into account. By performing NMR measurements consecutively over a short period of time, the AFP loss rate is determined by averaging over 10 measurements. The lifetime is then determined by fitting the data to an exponential decay function with loss rate as the correction factor.

In total ten ^{3}He cells have been tested during the course of this study. Two are the Rb-only-cells, and the rest are the hybrid cells (Rb+K), all filled at College of William and Mary. The names "Kosmo" and "Kelly" are given to the Rb-only-cells while "Katrine", "Kramer", "Jagger", "Richards", "Elvis", "Princeton", "Linda" and "Tatoo" are given to hybrid cells.

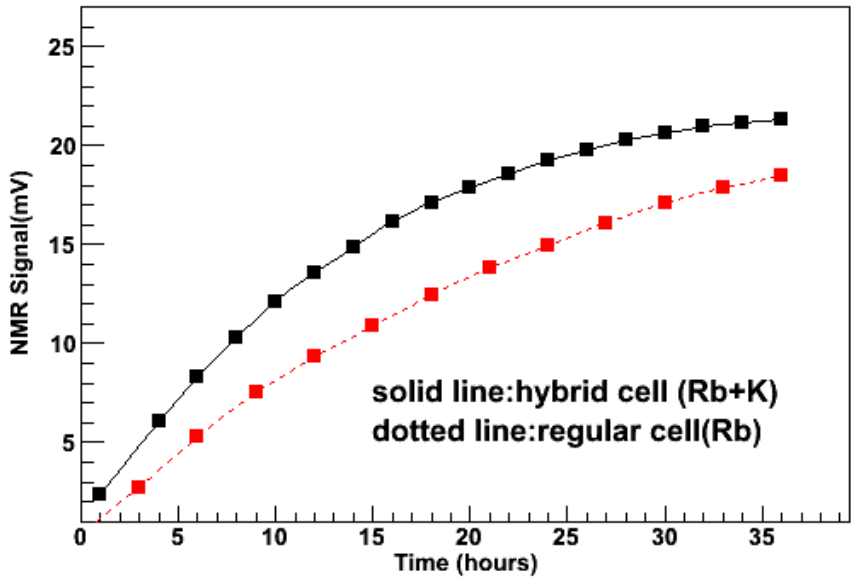

FIGURE 4.8: Pump up curves of "Kosmo"and "Katrine".

A measurement of polarization versus time is called a spin-up (or pumpup) measurement. The spin-up curve is fitted using the following equation

$$NMR(t) = A \cdot (1 - 0.01)^{(x+3.0)/3.0} \cdot (1 - e^{-x/t}), \tag{4.23}$$

where A is the amplitude and t is the time, 0.01 is the NMR measurement loss

rate (i.e. each NMR measurement causes 1% polarization loss.) and 3.0 is the time interval between two NMR measurements. The steady increase of NMR signal can be seen from Fig. 4.8, which shows the pumpup curve for two cells "Kosmo" and "Katrine". The results for Rb-only-cells are obtained under the following condition: the magnetic holding field is 25 G, the oven operating temperature is 170-175°C, which is optimal for laser absorption. The experimental condition for hybrid cells is slightly different, and the optimal oven temperature is around 235°C. For all these measurement, two 60-watts lasers are used.

Table 4.1 summarizes the test results for seven cells.

4.5.2 Water Calibration of ^{3}He NMR Measurement

The ^{3}He NMR signal does not indicate the absolute value of polarization of ^{3}He. In order to determine the absolute polarization of ^{3}He, it is necessary to do a calibration with a sample—such as water—whose polarization is well known. Given a magnetic holding field, the thermal polarization of protons in water is given by

$$P_p = tanh(\frac{\mu B}{kT}) = tanh(\frac{h\nu}{2kT}) \approx \frac{h\nu}{2kT}, \tag{4.24}$$

where $h = 6.626 \times 10^{-34}$ Js is the Planck constant, μ the magnetic moment, B the holding field, k the Boltzmann constant, T the water temperature in K, and $\nu = 91$ kHz is the Lamor frequency for a magnetic field of 21.36 Gauss. At 295 K, $P_p = 7.4 \times 10^{-9}$. The ratio R of ^{3}He signal height $S_{^3He}$ to that of the water S_p can be written as:

$$R = \frac{S_{^3He}}{S_p} = \frac{[Q\nu nV\mu P(n_{pc}\Phi_{pc} + n_{tt}\Phi_{tt} + n_{tc}\Phi_{tc})/G^{Pre}]_{^3He}}{[Q\nu nV\mu P\Phi/G^{Pre}]_p}, \tag{4.25}$$

where Q is the quality factor of pickup coils, n is the number density in m^{-3}, V is the volume in m^3, μ is magnetic moment in JT^{-1}, G^{pre} is the gain of the pre-amplifier, P

Cell	Kosmo	Kelly	Katrine	Richards	Elvis	Linda	Bolt
Polarization	34.1%	34.3%	38.5%	33.2%	46.1%	45%	69%
NMR Signal(mV)	20.9	23	22.5	28	44	40	40
EPR Freq. Shift(kHz)	37.7	36	37.4	34	N/A	40	41
Lifetime(hrs)	63.5±0.3	68±0.4	33.2±0.1	34±0.1	36.4±0.15	34	42
Pumpup time(hrs)	23.5±0.7	16.3±0.3	13.2±0.4	7.3±0.2	10.8±0.1	11	12
EPR Calibration constant	0.905	0.951	1.029	1.001	1.03	1.01	1.05

Table 4.1: Test results for seven target cells. "Kosmo" and "Kelly" are Rb-only cells. All other five are Rb-K hybrid cells. Cell "Linda" is used in the 2008 HIγS experiment, and cell "Bolt" was made afterwards.

is the polarization. Φ is the magnetic flux through the pickup coils. The subscripts ^3He and p in the equation represent ^{3}He and water (protons), respectively. pc, tt and tc denote the pumping chamber, the transfer tube and the target chamber, respectively. In light of this equation, the polarization of ^{3}He can be expressed as

$$P_{^3He} = \frac{[Q\nu nV\mu\Phi]_p}{[Q\nu V\mu(n_{pc}\Phi_{pc} + n_{tt}\Phi_{tt} + n_{tc}\Phi_{tc})]_{^3He}} \frac{S_{^3He}}{S_P} \frac{G_p^{Pre}}{G_{^3He}^{Pre}} P_p = cS_{^3He}, \tag{4.26}$$

where c is the water calibration constant. In our experiment, Q, ν cancel out because we run at the same RF resonance frequency for ^{3}He and water NMR measurement, corresponding to two different magnetic holding field values.

To do a water calibration, a cell with a geometry same as that of the ^{3}He cell is used. A single AFP sweep typically lasts 12 seconds, which are equally divided into three stages corresponding to the magnetic field conditions: ramping up, no-change and ramping down. The field changes from 18 G to 25 G at a rate of 1.75 G/s. We then average over the up sweep and down sweep signals for each water NMR measurement. To improve the overall signal-to-noise ratio for the NMR water measurement, over 500 sweeps are averaged. The typical water NMR signal is shown in Fig. 4.9.

The main uncertainties in determining the water calibration constant arise from the uncertainties of n, S and P_p. The uncertainty of the number density n comes from the uncertainty in the temperature and volume measurement. The density n_{pc}, n_{tt} and n_{tc} can be expressed respectively by

$$n_{pc} = \frac{n_0 V_{tot}}{V_{pc} + \frac{T_{pc}}{T_{tt}} V_{tt} + \frac{T_{pc}}{T_{tc}} V_{tc}}, \tag{4.27}$$

$$n_{tt} = \frac{n_0 V_{tot}}{\frac{T_{tt}}{T_{pc}} V_{pc} + V_{tt} + \frac{T_{tt}}{T_{tc}} V_{tc}}, \tag{4.28}$$

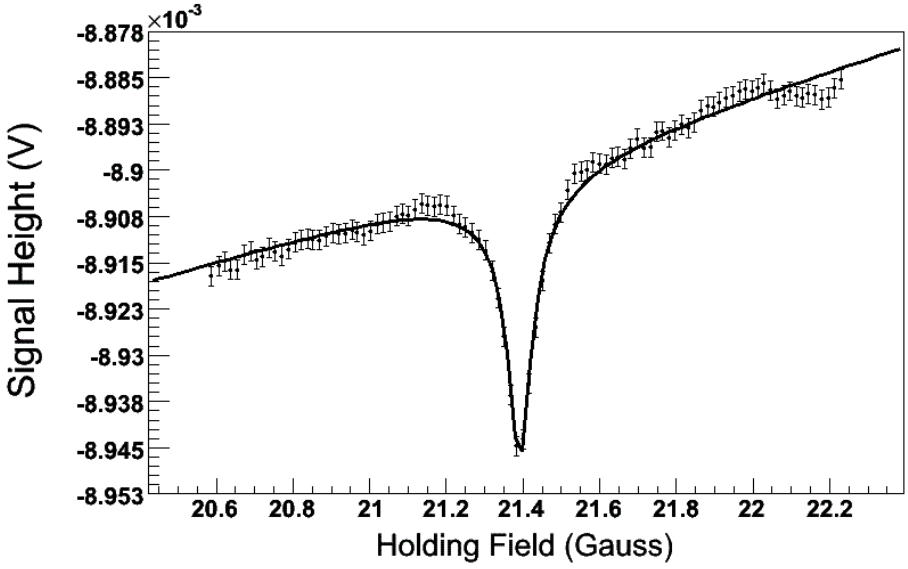

FIGURE 4.9: A typical water signal averaged over 500 sweeps.

$$n_{tc} = \frac{n_0 V_{tot}}{\frac{T_{tc}}{T_{pc}} V_{pc} + \frac{T_{tc}}{T_{tt}} V_{tt} + V_{tc}}, \tag{4.29}$$

where n_0 is the density of ^{3}He cell at the room temperature,

$$V_{tot} = V_{pc} + V_{tt} + V_{tc}. \tag{4.30}$$

In our target system, $\delta T_{pc} = \delta T_{tt} = 10$K, $\delta T_{tc} = 5$K. The uncertainties in the density n_{pc}, n_{tt} and n_{tc} are less than 1%. The uncertainty due to the volume measurement is less than 0.5%. The total uncertainty in the density is smaller than 1.1%.

A major systematic error in our NMR measurement is from the determination of the cell position which affects the magnetic flux through the pickup coils, i.e, the NMR signal height. This effect is studied by running the flux calculation code 100 times while varying a set of parameters randomly within the uncertainty of the cell position measurement. The overall uncertainty in the flux due to the cell position measurement is 2.6%. Table 4.2 lists the systematic uncertainties associated with

NMR measurement. The overall uncertainty in the NMR-AFP polarimetry is 3.5%.

Description	Parameter	Uncertainty
Water NMR Signal Height	S_p	1.1%
Flux(all chambers)	Φ	2.6%
Density	n	1.1%
Polarization	P_p	1.0%
Water calibration constant	c_{NMR}	3.2%
^{3}He NMR Signal Height	S_{NMR}	1.5%
Total NMR uncertainty	P_{NMR}	3.5%

Table 4.2: NMR polarimetry uncertainty.

4.5.3 EPR Measurements

When applying the external magnetic field, Rb atom ($F = 3$) state splits into seven sublevels. The frequency of the $m_F = -3 \rightarrow m_F = -2$ transition is proportional to the magnetic field plus the field created by the polarized ^{3}He:

$$\nu_{EPR} = \nu_0 + \Delta\nu. \tag{4.31}$$

Description	Parameter	Uncertainty
Frequency shift	$\Delta\nu$	3%
Derivative	$d\nu_{EPR}/dB$	0.16%
Constant	κ	1.5%
Density	n_{pc}	1.1%
Total EPR uncertainty	P_{EPR}	3.5%

Table 4.3: EPR polarimetry uncertainty.

As mentioned above, the EPR frequency shift during the measurement is given by the difference in the ν_{EPR} before and after the spin flip. The following equation [87]

gives a quantitative description of the relationship between this quantity and ^{3}He polarization inside the pumping chamber:

$$2\Delta\nu_{EPR} = 2 \times \frac{2\mu_0}{3}\frac{d\nu_{EPR}}{dB}\kappa\mu_{^3He}n_{pc}P_{pc}. \tag{4.32}$$

In order to extract the EPR frequency shift, a constant function is used to fit the EPR spectrum. The discussion of the terms on the right hand side is as follows: μ_0 is the permeability of vacuum, $\mu_{^3He}$ the magnetic moment of ^{3}He, the cell density n_{pc} has been given before. The derivative $d\nu/dB$ has a unit in MHz/G and can be calculated from the absolute EPR resonance frequency. It is fitted by the linear function [88],

$$\frac{d\upsilon}{dB} = 0.4670779 + 7.37904 \times 10^{-4}B, \tag{4.33}$$

where B is the holding field magnitude.

The constant κ is related to the spin-exchange cross section and is independent of ^{3}He polarization. It is determined in [84]:

$$\kappa = 4.52 + 0.00934T_{pc}, \tag{4.34}$$

where T_{pc} is the pumping chamber temperature, typically 175°C for Rb-only cell and 235°C for hybrid cell.

The polarization of the EPR measurement is as follows:

$$P_{pc} = 2\Delta\nu_{EPR} \times (2 \times \frac{2\mu_0}{3}\frac{d\nu_{EPR}}{dB}\kappa\mu_{^3He}n_{pc})^{-1}. \tag{4.35}$$

Since $\delta T_{pc} = 10$°C, the systematic error of the EPR measurement due to κ is determined as $\frac{\delta\kappa}{\kappa} = 1.5\%$. Another major uncertainty in the determination of polarization from EPR measurement comes from the frequency shift, which is typically $\delta\Delta\nu_{EPR}$=1 kHz, corresponding to an uncertainty of less than 3%. The uncertainty

of $d\nu/dB$ comes solely from the uncertainty in the field magnitude $\delta B/B$ which is determined to be 1.6×10^{-3}. Table 4.3 lists all sources of systematic uncertainties. The overall uncertainty in the EPR polarimetry is 3.5%.

Fig. 4.10 shows an example of EPR measurement taken from the cell "Kelly".

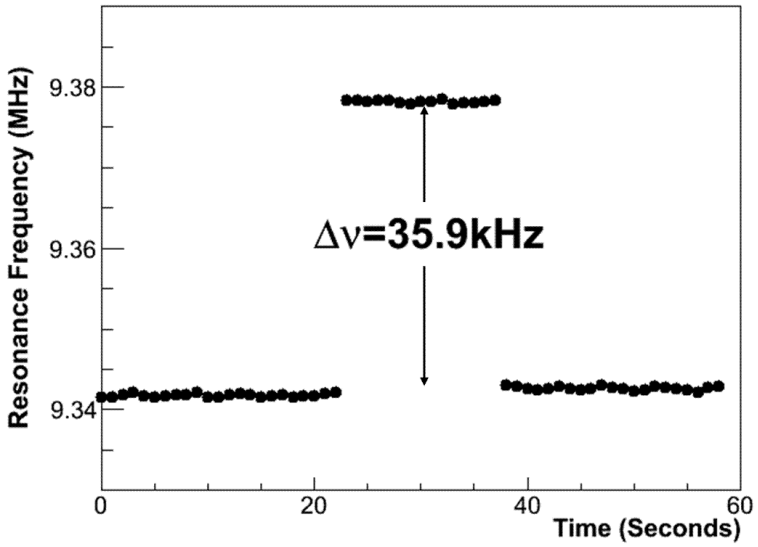

FIGURE 4.10: EPR measurement of cell "Kelly". The frequency shift is proportional to the ^{3}He polarization.

The polarization of ^{3}He target is measured by two methods: NMR-AFP and EPR. The NMR measurement gives

$$P_{^3He} = c_{NMR} S_{NMR}, \tag{4.36}$$

where the value of water calibration constant c_{NMR} depends on different cells as well as the physical position of the water cell. The EPR and NMR polarimetry agree to within 3% based on extensive measurements on cell "Richards". Polarization values based on EPR measurements for different cells are listed in Table 4.1.

5

Data Analysis

The goal of this experiment is fourfold: first, to measure a double spin asymmetry from three-body photodisintegration of longitudinally polarized ^{3}He using a circularly polarized photon beam; second, to extract the unpolarized differential cross section for the aforementioned process; third, to obtain the helicity-dependent differential cross section difference, and finally, to extract the total cross section of $^3\vec{H}e(\vec{\gamma}, n)pp$.

A double spin-dependent asymmetry is defined as,

$$A = \frac{\frac{d\sigma_{++}}{d\Omega} - \frac{d\sigma_{+-}}{d\Omega}}{\frac{d\sigma_{++}}{d\Omega} + \frac{d\sigma_{+-}}{d\Omega}}, \tag{5.1}$$

where σ_{++} and σ_{+-} refer to the cross sections of the two different target spin states, respectively. In the above definition, the photon beam helicity is positive, i.e., right circularly polarized photons. Similarly, one can form the asymmetry by flipping the photon beam helicity and keeping the target spin direction unchanged. In an ideal experiment, one needs to take data for all four beam-target spin configurations with about the same amount of beam time for each configuration in order to suppress false asymmetries. The beauty of measuring an asymmetry is that many experimental

factors which need precise determinations in cross section measurement would cancel out to the first order.

Using the experimental quantities, the asymmetry expression is written as,

$$A = \frac{N_P - N'_A}{N_P + N'_A - 2N'_N} \cdot \frac{1}{P_t \cdot P_b}, \tag{5.2}$$

where N_P (N'_A) refers to the number of neutron events within the chosen acceptance and after the cuts applied (will discuss in details later) when the target spin and the photon spin are parallel (antiparallel), normalized to the integrated photon numbers of the parallel spin case. N'_N refers to the corresponding neutron events from the nitrogen reference cell also scaled to the integrated photon numbers of the parallel spin case. P_t and P_b are the target and beam polarization, respectively.

The unpolarized differential cross section is defined as,

$$\frac{d\sigma}{d\Omega} = \frac{(N_P + N'_A)/2 - N'_N}{N^P_\gamma \cdot N_t \cdot \varepsilon}, \tag{5.3}$$

where N_P, N'_A and N'_N are defined before. N^P_γ is the integrated number of photons extracted using the downstream detectors in spin parallel runs. N_t is the target thickness. ε is the detector acceptance which includes both the extended target effect and the detector efficiency extracted from the simulation.

Similarly, the helicity-dependent differential cross section difference is obtained via the following formula,

$$(\frac{d\sigma}{d\Omega})_P - (\frac{d\sigma}{d\Omega})_A = \frac{N_P - N'_A}{N^P_\gamma \cdot N_t \cdot \varepsilon}. \tag{5.4}$$

It is noted that N_2 is not relevant to the above equation. The reason is that N_2 is unpolarized, so it doesn't affect the helicity-dependent cross section difference. In a photodisintegration measurement, such as the ${}^3\vec{H}e(\vec{\gamma}, n)pp$ process at low energies,

the process of interest only produces a small number of neutrons compared with the total number of events collected. Therefore, the core of the analysis is to subtract the large background and extract neutron events reliably. This includes two major steps: the detector calibration and particle identification (PID) by applying cuts to separate neutrons from photons.

A detailed description of how data are analyzed is presented in this chapter.

5.1 Analysis Procedure

Our approach is to extract all the raw counts in spin Parallel (P), spin Anti-parallel (A) and N_2 (N) cases using the same cuts, and scale them according to the integrated photon numbers. In calculating the asymmetry, the beam and target polarizations also need to be taken into account.

For the extraction of the differential cross section, we use the same raw counts in three cases as well as the absolute integrated photon flux information. A Monte Carlo simulation is also used to correct for the detector acceptance which includes both detector efficiency and the extended target effect.

The data analyzed in this thesis were obtained during a 36-hr data taking period from May 15th-17th, 2008. Table 5.1 summarizes all the 11.4 MeV runs we have analyzed.

To determine spin P and A, we resort to the EPR frequency signal. Since ^{3}He g-factor [1] is negative, when ^{3}He spin is parallel to the magnetic field, the EPR frequency is lower. Therefore, if we do an EPR measurement in parallel case, we observe the signal as low$\rightarrow$ high $\rightarrow$ low (like a hat). If the initial spin is antiparallel, then we observe high $\rightarrow$ low $\rightarrow$ high (like a well). In this way, we determine the spin directions.

[1] Nucleons and nuclei have spin and magnetic moments and therefore associated g-factors.

Target	Total runs	Run number
D_2	2	368-369
^{3}He Spin P	18	370-376, 388-393, 407-411
^{3}He Spin A	21	379-385, 396-402, 413-419
Aluminum plate	1	421
N_2	8	423-430

Table 5.1: 11.4 MeV run summary: D_2 runs were taken at the beginning, then we had 3 sets of spin P and A data in turns. Aluminum plate and N_2 data were taken towards the end. The time for each individual run was about half an hour, and the total beam time on ^{3}He target was around 20 hrs.

5.2 Raw Data Conversion and Skim of the Data

The software we use to convert raw data to ROOT ntuples is called TRAP, which refers to TUNL Real-time Analysis Package. The purpose of this software is to simplify the processes involved in creating acquisition and analysis software for the physics experiments at HIγS. These tools allow us to vary analysis parameters, generate histograms, and define data cuts. I will describe details of the off-line analysis procedure used to determine the asymmetry from the raw data.

After converting raw data into the Ntuples, the skim of the data is conducted. This skim process serves as a first pass of the data quality check. In the scaler of each Ntuple file, the following information is read out: paddle counts, counts of the 2 downstream detectors, time, veto time, clock, and event number. In the Ntuple file, the three important output parameters are time-to-analog converter (TAC), analog-to-digital converter (ADC) and time-to-digital converter (TDC) channel numbers, which correspond to pulse shape discrimination (PSD), pulse height (PH) and time-of-flight (TOF) information. During the skim process, events with paddle rates smaller than 20000 Hz are dropped. This is to get rid of the periods when the beam was unstable, for example, when the beam tripped. Figure 5.1 shows the paddle rate over the entire running period. This results in roughly 1% loss of data.

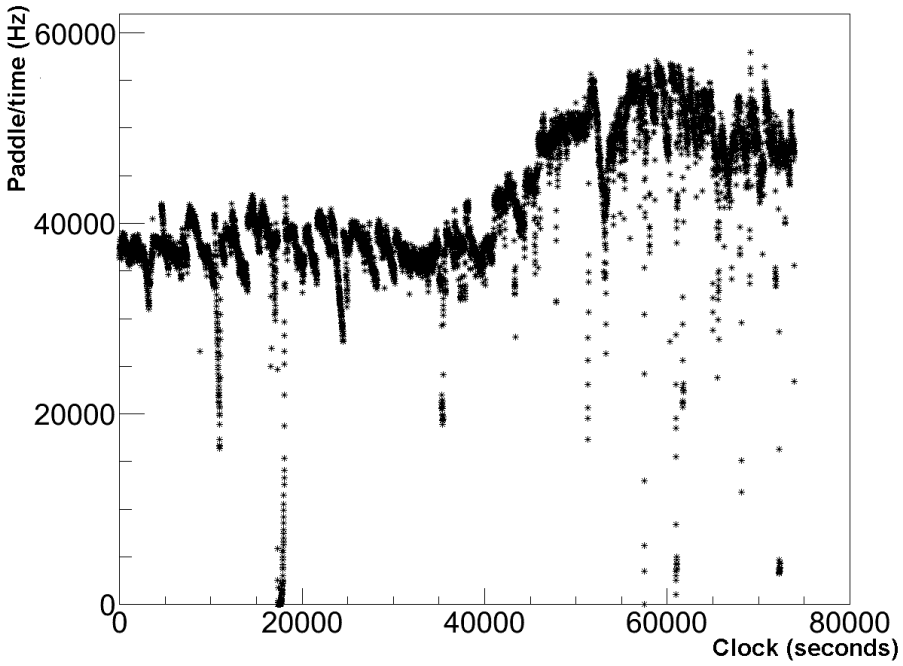

FIGURE 5.1: The paddle rate over the 11.4 MeV running period. Events with paddle rates lower than 20000 Hz are dropped.

5.3 ADC Calibration

After the data were skimmed, calibrations were conducted to relate detector information to the physical variables of detected particles including the energy and timing information.

First, the goal of ADC calibration is to relate ADC channel numbers to the pulse height of the neutron detector signal. The expression of the calibration is

$$PH(MeV_{ee}) = (ADC - pedestal) \cdot gain. \tag{5.5}$$

Please note: eV and eV_{ee} are not the same thing. The former is to measure the energy and the latter is to measure the response of a detector. The reason the subscript ee (which means electron-equivalent units) is adopted is because light output for heavier particles such as a proton is smaller than that of an electron of

an equal kinetic energy.

From the expression above, it is obvious to conclude that we need to determine two quantities: the pedestal and the gain.

5.3.1 Pedestal Determination

At the beginning of the experiment, a few runs were performed to measure the ADC pedestal, which refers to the offset resulting from the DC bias of the electronics, mostly due to photo-multipliers (PMTs). In other words, when no events were received by the detector, triggers were used to readout the ADC channels. Figure 5.2 exhibits a typical pedestal spectrum from ADC channels.

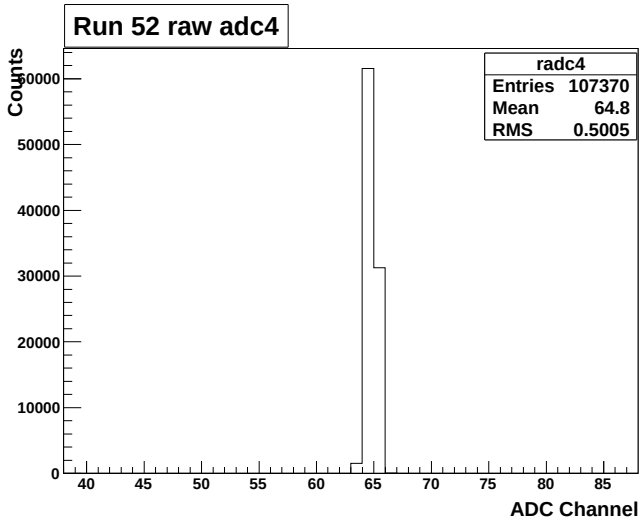

FIGURE 5.2: A pedestal spectrum from ADC channels.

The centroid values of the pedestals are determined by fitting the spectrum to a Gaussian curve. Table 5.2 lists the pedestal values of the 7 detectors.

Detector	Pedestal(ADC channel)
50°	110
75°	102
90°	65
105°	113
130°	97
145°	102
160°	97

Table 5.2: ADC pedestal channel numbers for detectors used in the experiment.

5.3.2 Gain Determination

The detector gain is defined as energy per channel. It is obtained through a two point calibration,

$$gain = \frac{Cs_{Edge}(MeV_{ee}) - Ped(MeV_{ee})}{Cs_{Edge}(ADC) - Ped(ADC)}, \tag{5.6}$$

where Cs_{Edge} refers to Cs edge and Ped refers to pedestal. From the last subsection, we know the Pedestal positions and Ped(MeV_{ee})=0. So we need to extract the Cs edge positions from the ^{137}Cs source calibration runs.

The ^{137}Cs runs were conducted by placing a ^{137}Cs source near the detectors. It usually took 5 minutes to accumulate enough statistics to determine the Compton edge. The Cs source generates a well known γ-ray of 662 keV, which enters the liquid scintillating detector and subsequently causes scintillation by Compton scattering with the electrons inside. The highest kinetic energy that the recoil electron can have after Compton scattering with the incoming γ-ray is the backscattering, when θ=180°.

In determining where the Cs edge is located, a GEANT4 simulation was performed in which 662 keV gammas were incident at one 90° detector and the resulting light output spectrum was viewed. A smearing was applied to the simulated light

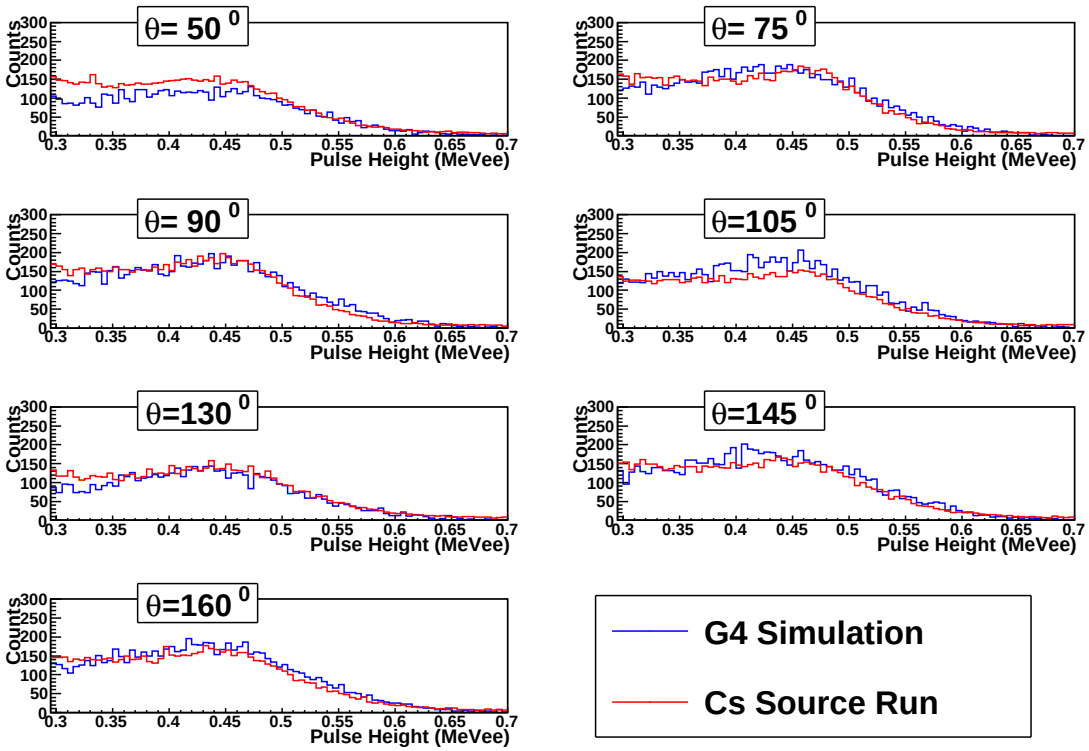

FIGURE 5.3: Comparison between Cs source run data and GEANT4 simulation. The Cs edge is determined to be at 0.52 MeV_{ee}.

output data so that it is consistent with the experimental Cs source data. Figure 5.3 shows the comparison between the simulation and the experimental data. The location of the Cs edge can be extracted from the simulated histogram. A conclusion was made that 1 Cs = 0.52 MeV_{ee}. The gain numbers are shown in Table 5.3.

5.4 TDC Calibration

There are 4096 TDC channels and their full-scale range is around 208 ns. Similar to the ADC calibration where an ADC channel is converted to a pulse height, TDC channels need to be converted to TOF.

$$TOF = (TDC - TDC_{\gamma}) \cdot C + TOF_{\gamma}. \tag{5.7}$$

Detector	Gain (MeV_{ee}/chan)
50°	0.00045
75°	0.00051
90°	0.00047
105°	0.00050
130°	0.00049
145°	0.00046
160°	0.00049

Table 5.3: The detectors' gains were determined by the Cs edge and pedestal positions.

We need to determine two quantities as well: the γ peak position and the TDC calibration constant C.

5.4.1 γ-flash Alignment

Due to many factors such as the difference in cable length, raw TDC spectra have varied one by one. It is crucial as a first step to identify the γ peak and adjust it to zero. During our experiment, a run using a thin aluminum plate (Run 421) was taken to achieve this goal. The γ-flash spectrum corresponds to photons scattering from the target and traveling at the speed of light. These events are typically Compton scattered photons. Once the γ-flash position is found, then the TOF zero point can be determined. The width of γ peak provides a good measure of the timing resolution of the system. A reasonable FWHM value is less than 3 ns [89].

5.4.2 TDC Calibration Constant

TDC calibration constant is defined by the following equation,

$$TDC_{Cal} = \frac{TDC_n - TDC_\gamma}{TOF_n - TOF_\gamma}. \tag{5.8}$$

In order to extract the constants, we need to know the exact locations of both the gamma peak and the neutron peak. D_2 gas target runs can provide neutron peak

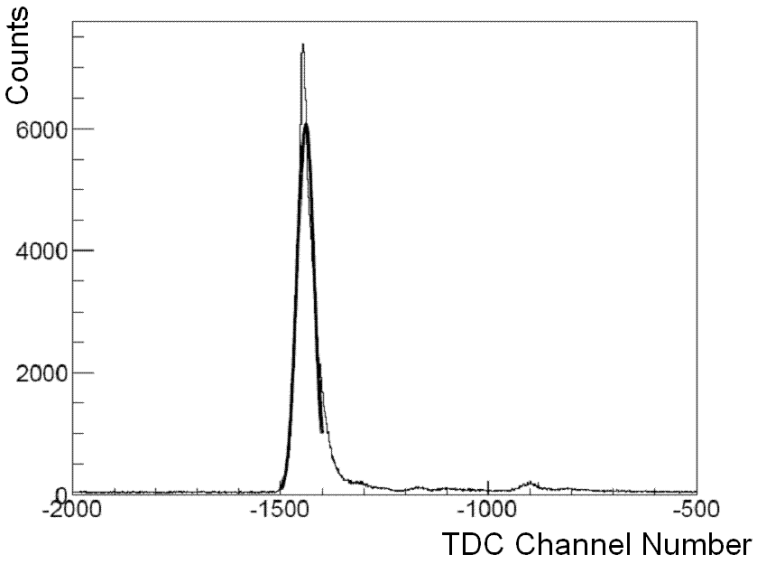

FIGURE 5.4: A fit was made to TDC spectrum (before any cuts) to determine γ-flash TDC channel number. The γ-flash is not an exact Gaussian distribution.

Detector	Gamma Peak(TDC channel)
50°	-1230
75°	-1265
90°	-1431
105°	-1300
130°	-1466
145°	-1488
160°	-1268

Table 5.4: Gamma peak positions expressed in TDC channel numbers.

information because neutrons from $^2H(\vec{\gamma}, n)p$ reaction have a Gaussian distribution at a fixed neutron angle in the lab. The centroid value of this peak is used as neutron peak position. The time when the gammas and the neutrons arrive can also be calculated. In this way, TDC calibration constants are determined. Figure 5.5 shows the γ-peak and neutron peak in the D_2 gas run. Since γ-rays travel at the speed of light before entering the neutron detectors, they arrive at a time before the slower-moving massive neutrons.

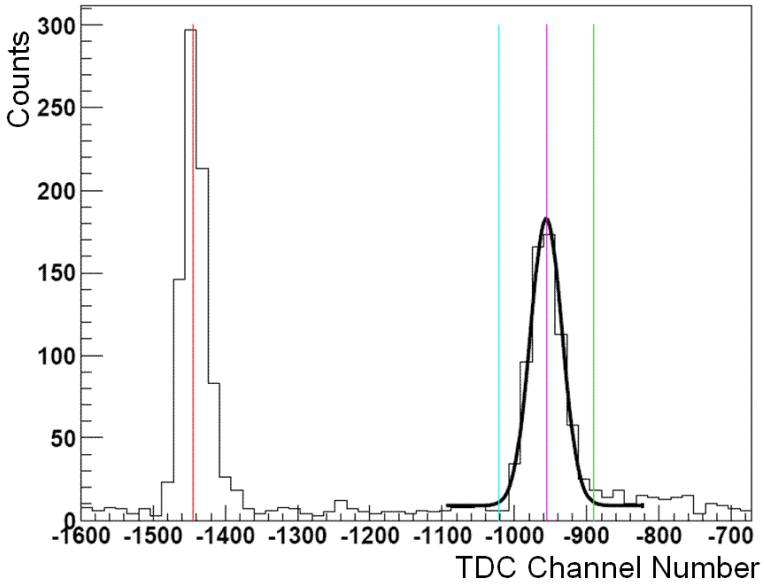

FIGURE 5.5: D_2 gas target run 369: the left peak is photon peak, and red line indicates the centroid value. The smaller right neutron peak is fitted using a Gaussian. Purple line indicates the centroid value.

However, the extended target effect could result in a slight inaccuracy of the constant determination. A GEANT4 simulation is used to fine tune the constants and the method is to adjust the TDC calibration constants until the D_2 data match the simulation. As can be seen from Figure 5.6, neutron peaks spread more at the backward and forward angles.

Detector	TDC calibration const. (ns/chan)
50°	0.048
75°	0.050
90°	0.049
105°	0.049
130°	0.049
145°	0.049
160°	0.050

Table 5.5: TDC calibration constants for BC-501A detectors used in the experiment.

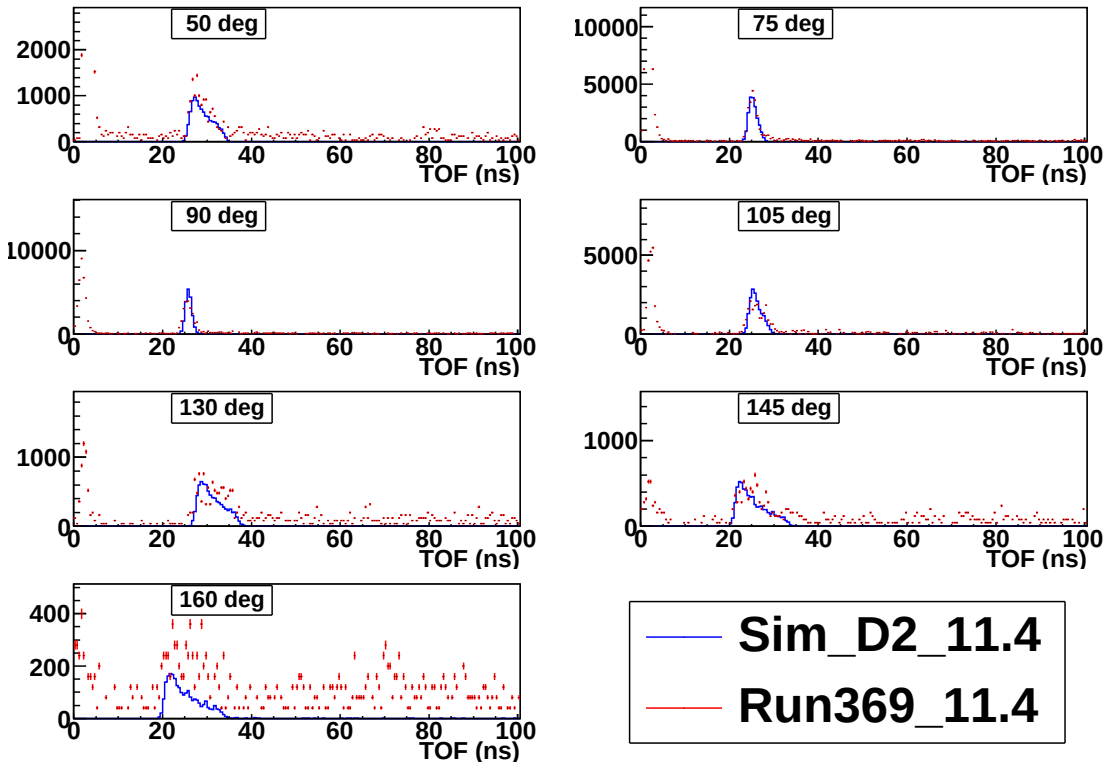

FIGURE 5.6: The comparison between the D_2 simulation and the D_2 experimental data. TDC calibration constants are fine tuned to match the two. We can see that the neutron peaks spread more at the backward and the forward angles due to the extended target effect.

5.4.3 Conversion from TOF to Energy

TOF information can be converted to neutron kinetic energy. We use the relation that the total energy is the sum of kinetic energy and rest energy to write the following expression,

$$E_k = \frac{M_n}{\sqrt{1-\beta^2}} - M_n, \tag{5.9}$$

where E_k is the detected neutron energy, $M_n = 939.565\ \mathrm{MeV/c^2}$ is the neutron mass, $\beta = v/c$, where v is the velocity of the particle and c is the speed of light. The first term on the right hand side is the total energy of a neutron with velocity v.

5.5 Cuts study

We now present the cuts placed on the data. Overall, 4 sets of cuts were applied. They are multiplicity cut, pulse shape discrimination (PSD) cut, pulse height (PH) cut and TOF cut.

5.5.1 Multiplicity Cut

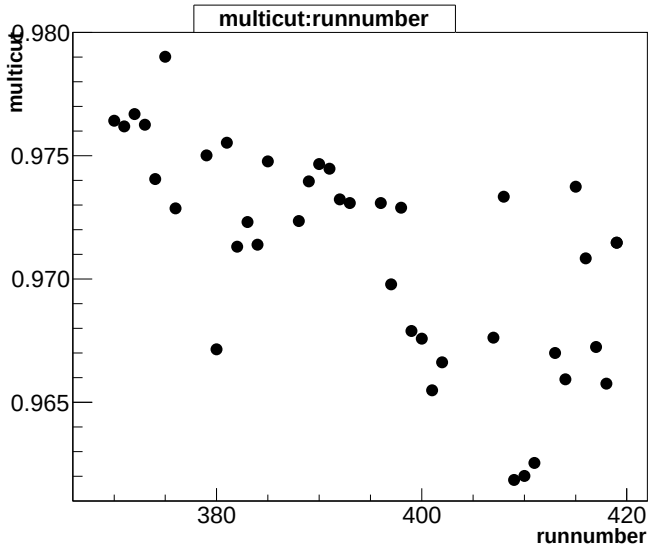

FIGURE 5.7: The ratio of events that passed the multiplicity cut.

The first cut applied to the data set is the multiplicity cut. The definition of multiplicity is: number of detectors which produce non-zero signals for a single event. The criteria is rather simple: any event with multiplicity larger than 1 will be eliminated.

Applying this multiplicity cut would result in roughly a 3% loss of the total events. Figure 5.7 shows the ratio of the total number of events that passed the multiplicity cut to the total number of events versus run number.

5.5.2 PSD Cut

For organic scintillators, the most common way to examine the event type is to study the decay time constants through pulse shape analysis. The technique of using charge integration to distinguish between the two types of events is described as follows: Most of the observed scintillation light is prompt fluorescence. The composite yield curve consists of two exponential decays: one is a fast component which has a decay time of a few nanoseconds and the other is a slow component which takes several hundred nanoseconds.

The process of pulse-shape discrimination can be used to separate neutron induced events from γ-ray induced events with the same pulse height. In the detector, γ-rays interact primarily with the electrons and neutrons interact primarily with protons. Protons and electrons will produce different amounts of light because of the delayed emissions. Protons, with higher dE/dx, will have longer decay times, therefore exhibiting longer "tails" to their pulses than electrons.

The definition of PSD parameter is the difference between the integrated charge over the long and short gates. The short gate has a time range of 20-40 ns and the long gate is around 150-200 ns. PSD measures the amount of charge in the tail of the pulse, as seen in Figure 5.8. In Section 2.4, a description of the mesytec MPD-4 4 channel particle discriminator module is given and this module uses a ratio of fast to slow component of scintillator light output.

A self-consistent and reproducible method to apply a PSD cut is described as follows. ADC channels are divided into equally spaced small segments, then the centroid values of each segment as well as the variance are extracted. Figure 5.9 shows a PSD spectrum with applied cut. We chose to apply the cut along the 6σ line and get rid of all the events on the left side. The systematic effect of varying the cut from 5σ to 7σ was studied and is presented in the later part of this chapter.

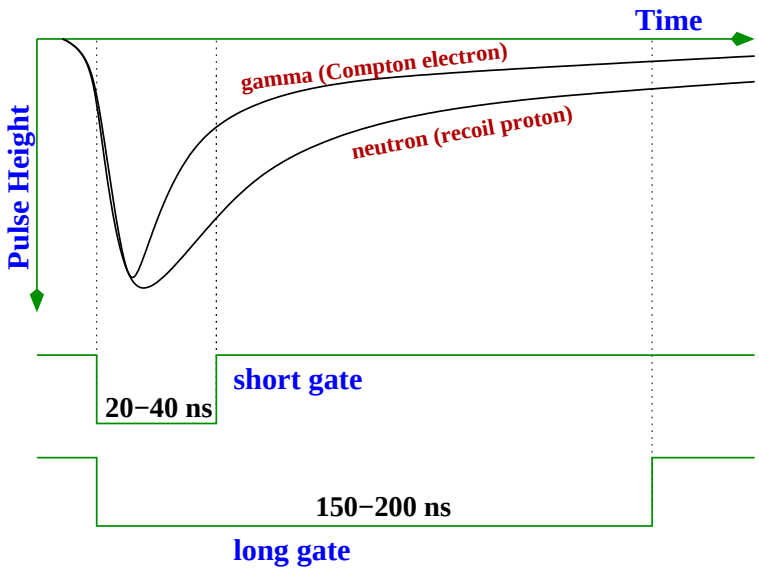

FIGURE 5.8: The traditional PSD technique via integrating over long and short gates. Figure is from [89]. The horizontal axis is time and the vertical axis is pulse height. Gammas and neutrons interact with electrons and protons respectively. Since electrons and protons have different decay time, they exhibit different tails.

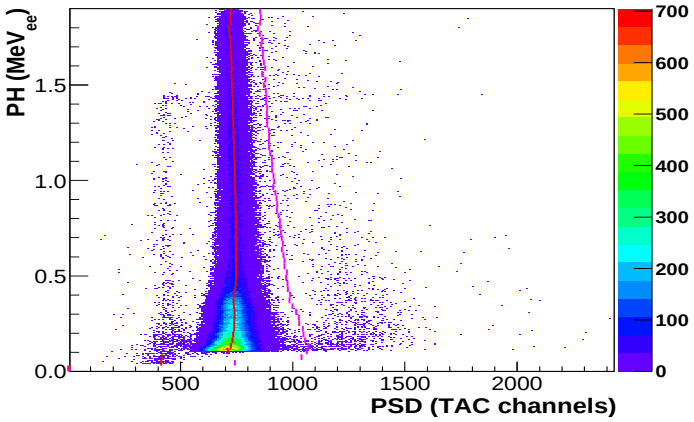

FIGURE 5.9: A PSD spectrum with the applied cut indicated by the right red curve. The left red curve indicates the centroid of the photon band, and neutrons locate to the right of the band. The vertical axis is calibrated PH in the units of MeV_{ee}.

5.5.3 PH Cut

The hardware threshold in the ADC channel is due to a pulse-height threshold of roughly $\frac{1}{4} \times^{137} Cs$ ($\sim$ 0.6 MeV) applied in the experiment. This threshold is not a straight line, instead it is smeared over a few keV$_{ee}$, which poses extra difficulty in comparing the data with the simulation. So we choose to apply a slightly higher software cut—0.2 MeV$_{ee}$ to make the edge uniform. In Figure 5.9, this cut means adding a straight horizontal line along the 0.2 MeV$_{ee}$ and getting rid of all the events underneath. Figure 5.10 shows the effects of PSD and PH cuts.

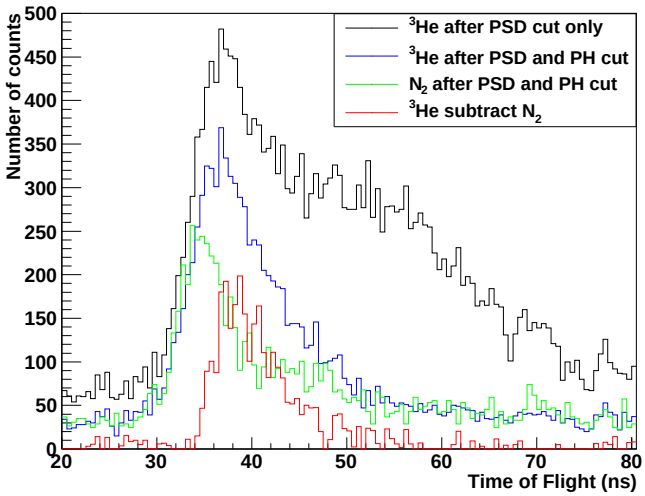

FIGURE 5.10: The effect of different cuts for all parallel spin runs at 90°. (From top to bottom) The top line is after 6σ PSD cut; the second line is after PH cut; the third line (green) is N_2 run after PSD and PH cuts, and the fourth line (red) is ^{3}He after N_2 subtraction.

However, a PH cut of 0.2 MeV$_{ee}$ would produce an efficiency curve with the rapidly changing section from 0 to 2.3 MeV neutron energy. Since the maximum energy of neutrons decreases with the increment of the angles, we take 50 degree to do a study. The neutrons have a maximum energy of 2.6 MeV, which is larger than the maximum neutron energy at six other angles. In this case, 88% [90] of the neutron

counts are in the rapidly changing region. At angles 130, 145 and 160 degrees, since the maximum neutron energies are smaller than 2.3 MeV, all the neutrons are in the rapidly changing region. This is a very big concern in the data analysis.

There are two other important points about the hardware threshold. First, the detection efficiency depends on Cesium threshold. Alex Crowell did an extensive study in his thesis [42] and showed that the higher the Cs Bias threshold, the lower the detection efficiency. Second, the relationship between the Cs threshold and corresponding neutron energies is not linear. For example, 1 Cs corresponds to about 2 MeV neutrons. However, the light output is not linear in that region [91]. Due to that, 1/4 Cs is about 0.6 MeV instead of 0.5 MeV.

5.5.4 TOF Cut

After the first three filters, a significant portion of photon events are rejected. The last round is TOF cut. While the leading edge of the TOF window was straightforward to determine according to the spectrum, the trailing edge was not. In fact, the trailing edge corresponds to the slow moving neutrons, i.e. low energy neutrons. Therefore by choosing a low energy cutoff–1.1 MeV in our case, the TOF window can be determined. There was a discussion about whether the low energy cutoff should be increased to 1.5 MeV in order to avoid the sharply increasing region on detection efficiency curve. Table 5.6 summarizes the ratios between the number of neutron events in the selected energy region and the total number of events. We decided not to use 1.5 MeV because it cuts away a large portion of neutron events. The cuts are varied from 1.0 MeV to 1.2 MeV (approximately $\pm$ 3 ns on TOF) to observe the systematic effects.

Table 5.7 shows the TOF window range. By summing over the raw counts within the TOF window and subtracting the events within an equal length of sideband to eliminate the background events, the number of neutrons were finally obtained.

Detector	CDB E_n >1.1 MeV	CDB E_n >1.5	AV18 E_n >1.1	AV18 E_n >1.5
50°	0.65	0.50	0.73	0.61
75°	0.66	0.49	0.75	0.62
90°	0.66	0.48	0.74	0.61
105°	0.64	0.46	0.73	0.59
130°	0.59	0.39	0.68	0.53
145°	0.53	0.34	0.62	0.47
160°	0.40	0.23	0.49	0.34

Table 5.6: The ratio between the number of neutron events in the selected energy region and the total number of neutrons according to different theories. CDB refers to CD Bonn.

Detector	TOF start (ns)	TOF stop (ns)
50	37	62
75	33	52
90	34	52
105	35	52
130	37	62
145	33	52
160	30	52

Table 5.7: TOF window range. The stop line corresponds to a neutron energy of 1.1 MeV. The side bands start from 90 ns, and have equal lengths as the neutron range. The regions are based on the simulation results.

For the sideband selection, the conventional method is to subtract events using two sidebands with lengths of one half that of the data region, one on each side. Since the left side is contaminated by photons, we simply place the side bands on the far right side, starting from 90 ns.

5.6 Photon flux determination

5.6.1 Back Detector Normalization

The determination of the accurate integrated γ flux information is crucial. As mentioned in Section 3.2, two methods were used during the experiment to monitor the

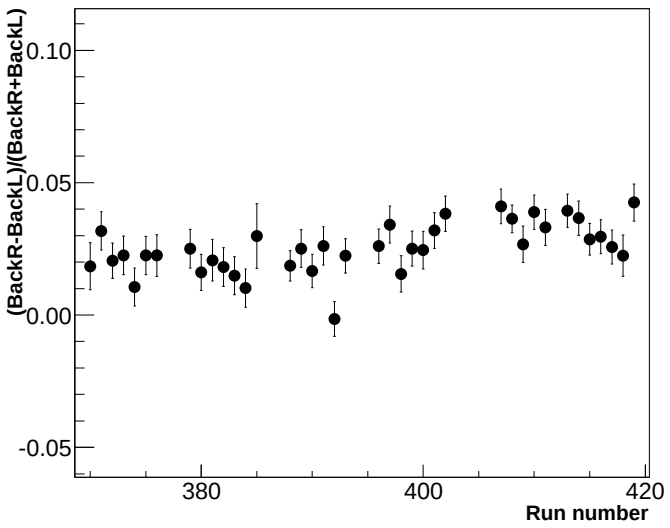

FIGURE 5.11: Two detectors were placed around the downstream D_2O target. This plot compares the asymmetry between the counts. The average of the two is used to extract the neutron yield.

flux. One was a 3-paddle system and the other was the downstream D_2O target with two neutron detectors. The efficiency of the paddle is energy dependent and must be well calibrated, so it can only be used as a rough check. In the downstream D_2O monitoring system, the two detectors were running in the fast mode (in MPD4 module) which means they were deadtime-free. Figure 5.11 shows a study of the asymmetry of the neutron counts on both detectors. We take the average of these two detectors as a measurement of the integrated photon flux.

Integrated photon number determination

To determine the integrated photon numbers, we used the following equation,

$$N_\gamma = \frac{N_n \cdot D_t}{N_t \cdot \frac{d\sigma}{d\Omega} \cdot \varepsilon}, \tag{5.10}$$

where N_n refers to the number of neutrons the back detectors received. D_t is the correction factor for deadtime. Since the back detectors were running in a deadtime

free mode, and the DAQ system (seven main detectors) had deadtime, this needs to be corrected (We can also correct the raw counts, same effect). N_t is the D_2O target thickness, $\frac{d\sigma}{d\Omega}$ is the differential cross section determined from the total cross section [64] and the angular distribution $\sin^2(\theta_{CM})$. ε is the detector acceptance which includes both extended target effect and the detection efficiency from the `GEANT4` simulation. In this way, the integrated photon numbers were determined.

The following table lists the values of all the parameters used in the extraction.

Parameter	Value
D_t	0.85
length	4.7 cm
D_2O density	1.1056 g/cm^3
Avogadro	6.02×10^{23} mol^{-1}
D_2O	20.04 g/mol
r	6.35 cm
d	91.44 cm
90° lab angle conversion	93.524°
$d\Omega_{CM}/d\Omega_{lab}$	1.0019
ϵ(efficiency)	0.213

Table 5.8: The parameters used in calculating the integrated gamma flux. r refers to the radius of the detector surface and d is the distance between the target center and detector surface center.

The total photon numbers for spin P, spin A and N_2 runs are:

$$N_\gamma^P = 1.126 \times 10^{12};$$
$$N_\gamma^A = 1.239 \times 10^{12};$$
$$N_\gamma^N = 5.488 \times 10^{11}. \quad (5.11)$$

Problems with the back detectors

Figure 5.12 shows the run-to-run neutron yields using the average back detector normalization. In the 11.4 MeV running period, we took 3 sets of data for each

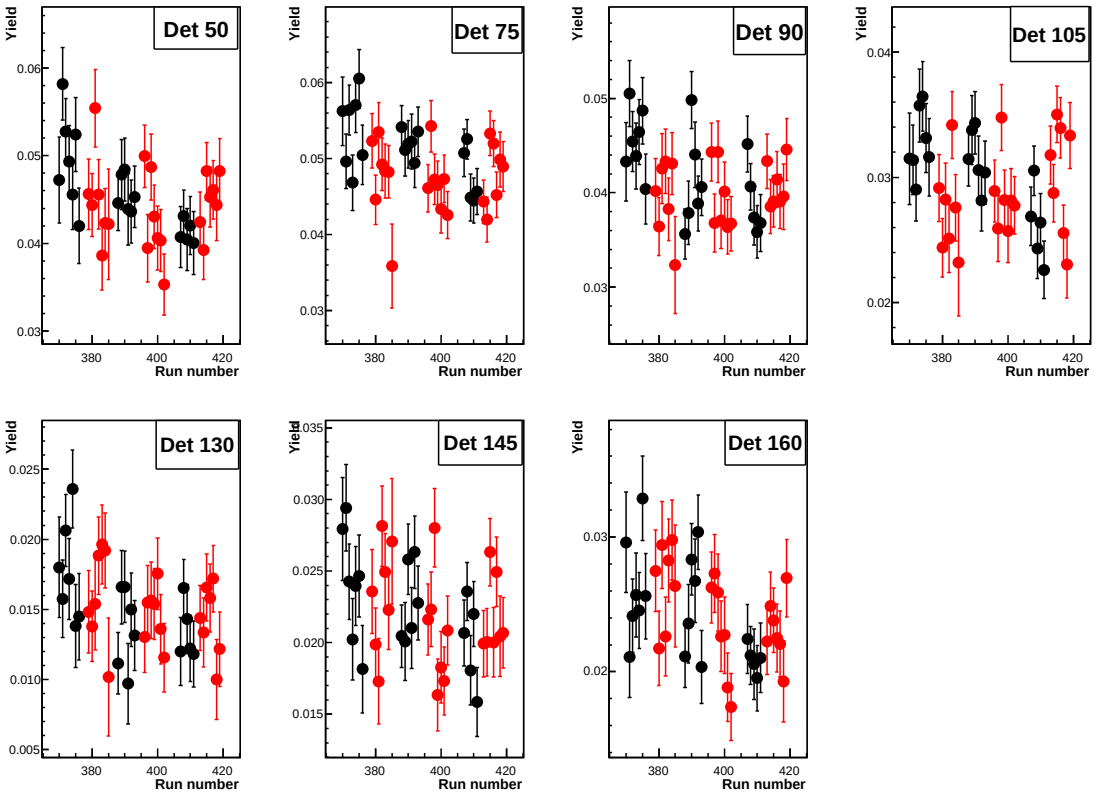

FIGURE 5.12: Neutron yields versus run number: Spin P (black) and Spin A (red). The yields are obtained from the number of accepted neutrons after PSD, PH and TDC cuts, corrected by the deadtime, then normalized by the average back detector counts.

spin state. A systematic downward trend versus run is observed, which gives rise to a false asymmetry. A considerable amount of work was devoted to studying this drift. The Experimental Physics and Industrial Control System (EPICS) online archive record during our running time was examined. This indicated that the beam intensity was increased by 30% between Run 395 and 400, which was during the second spin antiparallel period, as can be seen from Figure 5.13. Ring current was shifted from 105 mA to 108 mA, and intra-cavity power also shifted from 0.6 W to 0.7 W. The beam profile was relatively stable throughout the running time, because

the collision angles change very little, seen from Figure 5.14. Figure 3.2 shows that the distance between the collision point and the primary collimator is 60 m. Then in the X axis, if the angle changes by 0.01 mrad, the beam center will change by 60 m$\times$ 0.01 mrad $\sim$ 0.6 mm, which is negligible compared with the 22 mm diameter collimator. Therefore the beam profile was very stable during the runs.

The systematic drift of the normalized yields poses a challenge to the asymmetry measurement which is expected to be only of a few percent. Therefore, the result is very sensitive to relative normalization. After a lot of discussion, we decided to use a new method which is presented in the next subsection for relative normalization between spin P and A runs.

5.6.2 Gamma Peak Normalization

Fig 5.15 describes a new approach to estimate the relative photon flux: for each neutron detector, the majority of the events seen are photons, which means each neutron detector is essentially a gamma detector. For each run, we would select a gamma peak region on each detector's TDC spectrum and add the events together as the relative photon number measure for this run.

Figure 5.16 shows the comparison between back detector normalization and gamma peak normalization. We choose the 90° detector, and fit using a straight line to test the stability of the yields. Using the gamma peak, the yield is more stable, thus suppressing the false asymmetry.

However, there are two drawbacks of this gamma-peak method: first, this method can only provide relative integrated photon measurements. As a result, it is not applicable to cross section measurements which need absolute integrated photon information. Second, this method is cell- and position-dependent, which means the change of the target cell itself or its position would invalidate this method. Fortunately, the spin flip (P$\rightarrow$A or A$\rightarrow$P) didn't require the movement of the ^{3}He target, so this

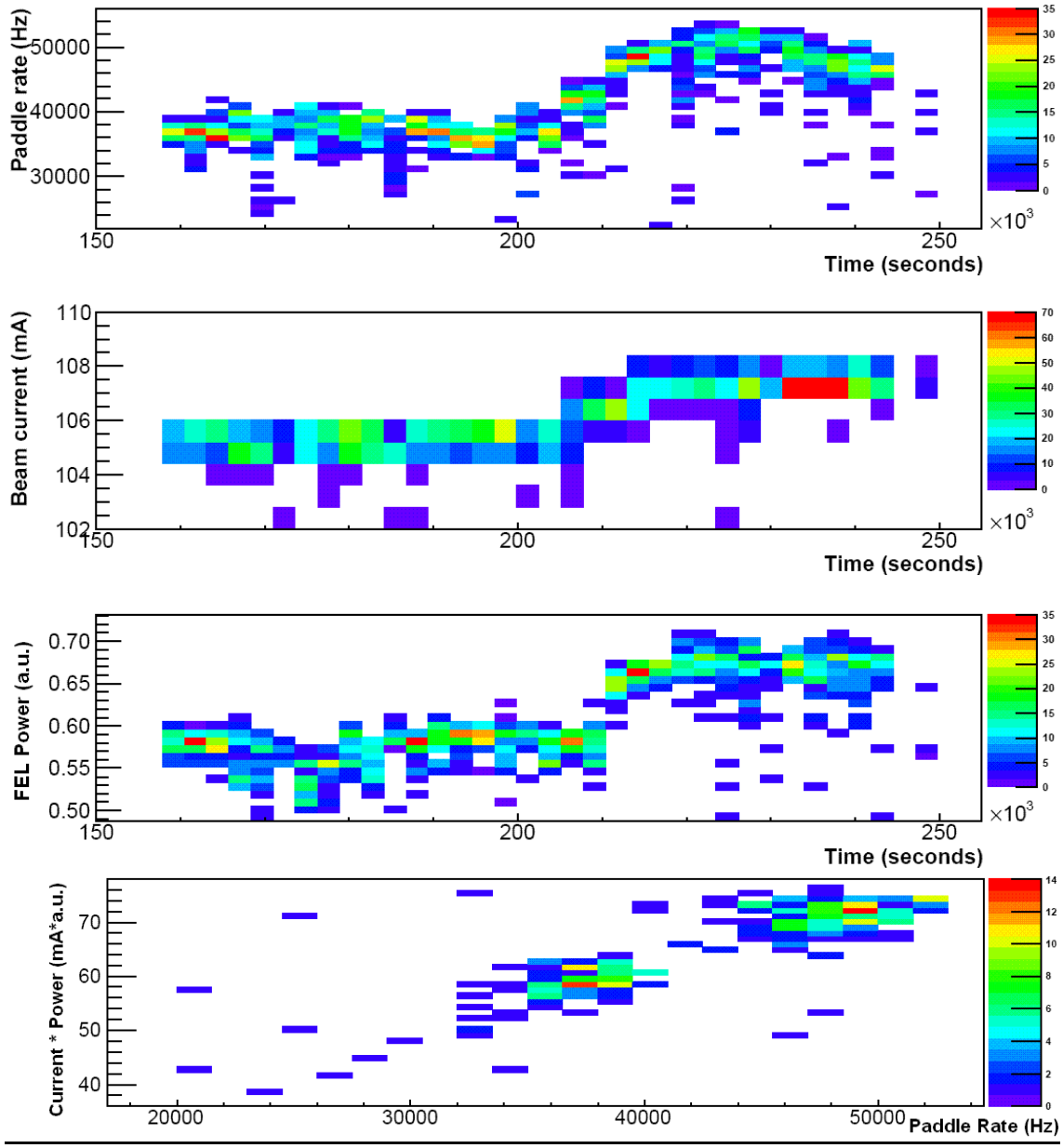

FIGURE 5.13: The top three plots show the Paddle rate, electron beam current and FEL power as a function of time. These three parameters indicate the stability of HIγS flux. The last one plots the correlation between the paddle rate and the product of beam current and FEL power. In principle, the product of ring current and FEL power should be proportional to flux.

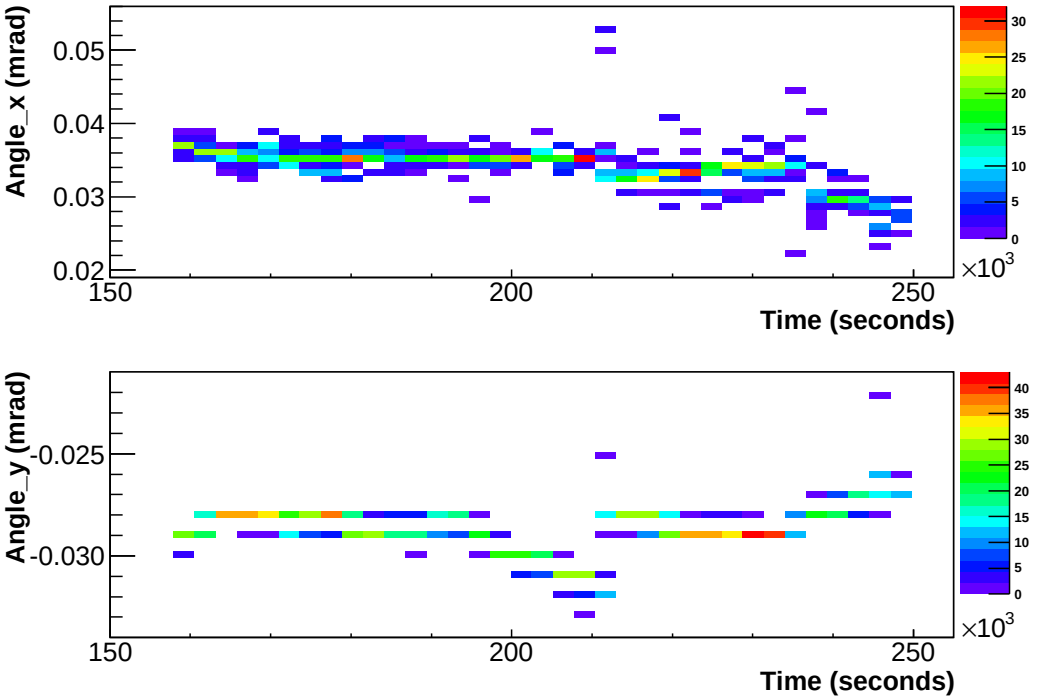

FIGURE 5.14: This plot shows the collision angles X and Y as a function of time. These two parameters indicate the stability of HIγS beam position. We consider beam profile stable during the running period.

gamma-peak normalization method is used to obtain the relative flux comparison between spin P and A runs.

Two other quantities are needed to obtain the physics asymmetry. They are ^{3}He target polarization and γ-beam polarization. It is claimed that the HIγS beam is 100% polarized, as presented in Section 3.2. We will discuss the target polarization in the next section.

5.7 Target Polarization

The ^{3}He target used in this experiment was named "Linda". Using the fact that Rb's resonance lines can be broadened by collisions with the ^{3}He atoms and the width of the laser absorption line is proportional to the density of the ^{3}He atoms

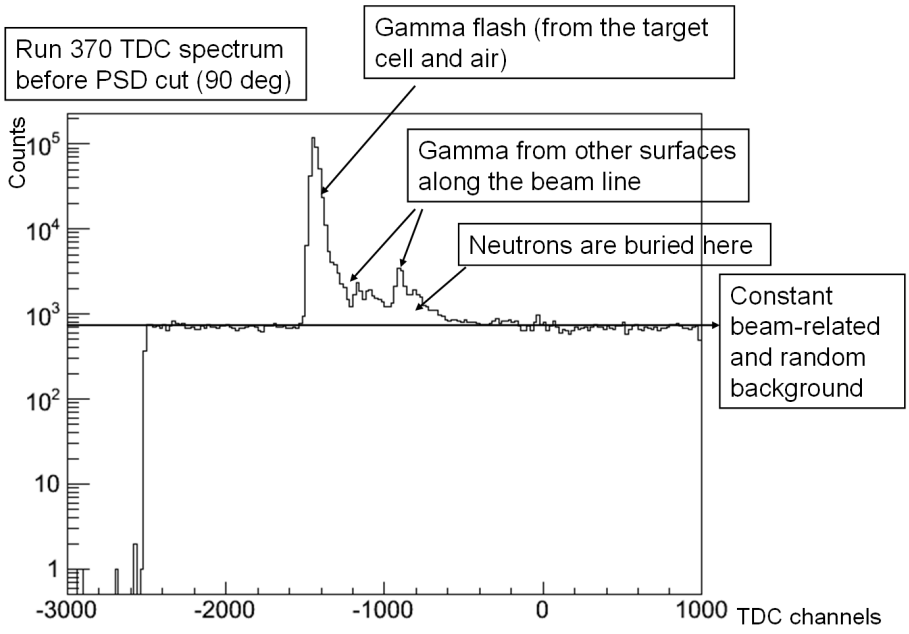

FIGURE 5.15: A self-explanatory figure: the straight horizontal line indicates a constant beam-related and random background. Total number of events within the γ-flash serves as a relative measure of the integrated photon numbers.

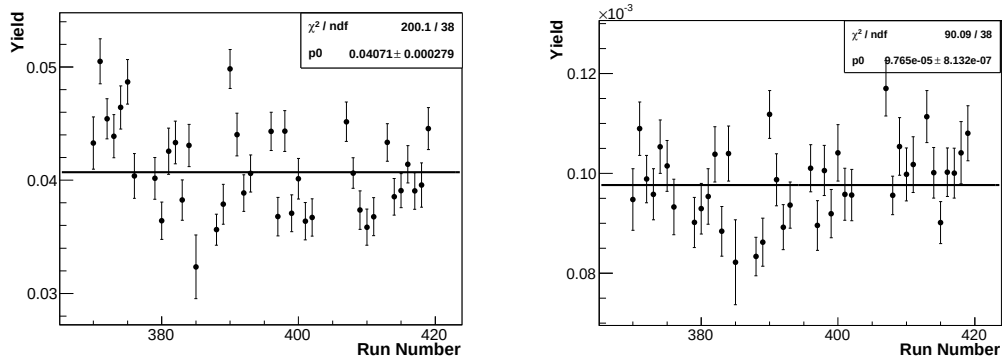

FIGURE 5.16: Comparison of the two normalization methods at 90°. The data points are normalized yields by back detector (left) and by photon (right). Both sets of data have "pol0" fit (fit with a straight line). The reduced χ^2 values are used to measure the yield stability. The photon normalization has a smaller value than the downstream detector normalization, which indicates that the γ-peak normalization method is more stable.

in the cell [92], its target density was determined to be 7.197 ± 0.070 amagats. At the beginning of the experiment, the oven temperature was not very stable, ranging from 228°C to 235°C. As a result, target polarization did not reach its peak (∼39%). Then a temperature controller was installed to maintain the oven temperature at 238°C. The NMR water calibration constant was determined to be 0.026 ± 0.001 $/mV$. During the production run period, we took advantage of the spin flip time interval (the time when we could access gamma vault) to do NMR measurements. The ^{3}He polarization were extracted as,

$$P_{^3He} = c_{NMR} \cdot S_{NMR}, \tag{5.12}$$

where c_{NMR} is the water calibration constant and S_{NMR} is the ^{3}He NMR signal. Figure 5.17 shows the ^{3}He polarization throughout the 11.4 MeV production runs. The average ^{3}He polarization was ∼42%.

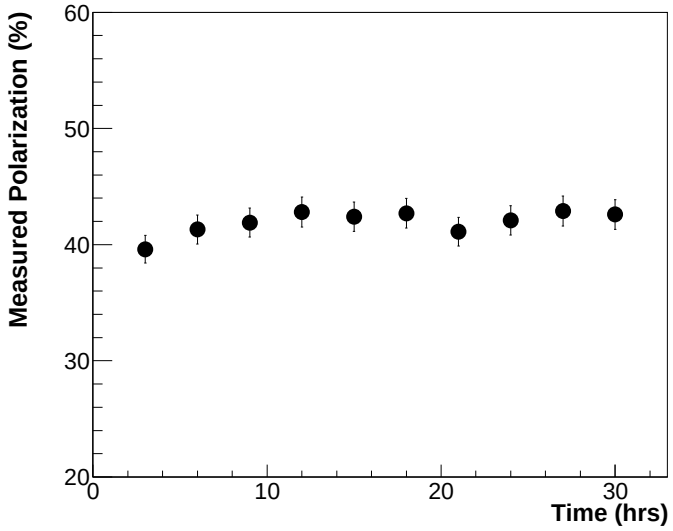

FIGURE 5.17: ^{3}He polarization during the 11.4 MeV running period. The polarization is based on ^{3}He NMR signal calibrated by water NMR signal.

5.8 Statistical uncertainty

After obtaining the neutron counts and polarizations, we are ready to extract the asymmetry.

5.8.1 Asymmetry Extraction

Rewrite the asymmetry from eqn. 4.2,

$$A = \frac{N_P - N_A \cdot \frac{N_\gamma^P}{N_\gamma^A}}{N_P + N_A \cdot \frac{N_\gamma^P}{N_\gamma^A} - 2N_N \frac{N_\gamma^P}{N_\gamma^N}} \cdot \frac{1}{P_t \cdot P_b}, \tag{5.13}$$

where N_P and N_A refer to the number of neutron events within the chosen acceptance and after the detector cuts. They include the contribution from the background, such as neutrons from the N_2, air and glass. The ratio $\frac{N_\gamma^P}{N_\gamma^A}$ is from the gamma peak normalization and $\frac{N_\gamma^P}{N_\gamma^N}$ is from the downstream detectors.

Another way to express the asymmetry is by using a dilution factor. They are two equivalent ways. Using the former expression makes the handling of statistical uncertainty easier; therefore, that's the one we chose to use.

5.8.2 Statistical Error Calculation

To properly handle the statistical uncertainty, we wrote the full expression for the asymmetry,

$$A = \frac{N_P - N_A \cdot a}{N_P + N_A \cdot a - N_N \cdot b} \frac{1}{P}, \tag{5.14}$$

where $a = \frac{N_\gamma^P}{N_\gamma^A}$, $b = \frac{N_\gamma^P}{N_\gamma^N}$, and $P = P_t \cdot P_b$.

The statistical uncertainty is,

$$\delta A = \frac{\delta(N_P - N_A \cdot a)(N_P + N_A \cdot a - N_N \cdot b) - (N_P - N_A \cdot a)\delta(N_P + N_A \cdot a - N_N \cdot b)}{(N_P + N_A \cdot a - N_N \cdot b)^2}$$
$$= \frac{\delta N_P(2aN_A - bN_N) + \delta N_A(-2aN_P + abN_N) + \delta N_N(bN_P - abN_A)}{(N_P + aN_A - bN_N)^2} \quad (5.15)$$

For further simplication, let

$$N_P + N_A \cdot a - N_N \cdot b = dn, \quad (5.16)$$

then

$$\delta A = \delta N_P(\frac{2aN_A - bN_N}{(dn)^2}) + \delta N_A(\frac{-2aN_P + abN_N}{(dn)^2}) + \delta N_N(\frac{bN_P - abN_A}{(dn)^2}). \quad (5.17)$$

Therefore we obtained the statistical uncertainty of the asymmetry:

$$\delta A = \sqrt{\delta N_P^2(\frac{2aN_A - bN_N}{(dn)^2})^2 + \delta N_A^2(\frac{-2aN_P + abN_N}{(dn)^2})^2 + \delta N_N^2(\frac{bN_P - abN_A}{(dn)^2})^2} \quad (5.18)$$

For the statistical uncertainty of the unpolarized differential cross section, we have

$$\frac{d\sigma}{d\Omega} = \frac{(N_P + N'_A)/2 - N'_N}{N_\gamma^P \cdot N_t \cdot \varepsilon}, \quad (5.19)$$

and the statistical uncertainty is,

$$\delta(\frac{d\sigma}{d\Omega}) = \frac{\sqrt{(N_P + N_A \cdot a^2)/4 + N_N \cdot b^2}}{N_\gamma^P \cdot N_t \cdot \varepsilon}. \quad (5.20)$$

For the helicity-dependent differential cross section difference, the statistical uncertainty is,

$$\delta((\frac{d\sigma}{d\Omega})_P - (\frac{d\sigma}{d\Omega})_A) = \frac{\sqrt{N_P + N_A \cdot a^2}}{N_\gamma^P \cdot N_t \cdot \varepsilon}. \quad (5.21)$$

5.9 GEANT4 Simulation

5.9.1 The Goal of the Simulation

To address the goal of the simulation, let's first write down the expression for the number of neutron events,

$$N_n = N_\gamma \cdot \rho \cdot \Delta Z \cdot \frac{d\sigma}{d\Omega} \cdot \varepsilon, \tag{5.22}$$

where N_γ is the integrated photon flux, ρ is the target density, ΔZ is the target length seen by the detector, $\frac{d\sigma}{d\Omega}$ is the differential cross section and ε is the acceptance.

There are two complications in the real experiment. One is that the ^{3}He target is 40 cm long, so the extended target effect needs to be taken into consideration. The other one is the detector efficiency, which depends on the PH cut. In order to correct for these effects, a GEANT4 simulation is needed.

The general methodology for the simulation is as follows. We ran the GEANT4 simulation twice under the same conditions. The first run is to use a point like target (Run 1) and the second is to use a 40 cm long target (Run 2). Then we divide the number of detected neutrons from Run 2, by the number of neutrons going into the detectors from Run 1 to obtain seven ratios, which describe the detector acceptance including both the detector efficiency and the extended target effect. The GEANT4 simulation needs to simulate as closely to the real experiment as possible so that all these convoluted effects could be taken into account.

5.9.2 GEANT4 *overview*

GEANT means GEometry ANd Tracking. It is a toolkit for simulating the passage of particles through various materials. The GEANT4 class has several categories: track, processes, tracking, event, run, readout. It is written in C++ and designed to accommodate the requirements of space and cosmic ray applications. The simulation

includes [93] many features, to name a few: 1. The geometry of the system. This means assigning a geometrical volume to all the experimental apparatus, and their relative positions. 2. The materials involved. We need to define all the materials in the objects. 3. The generation of primary events. In our case, the events are neutrons. 4. The tracking of particles through materials and electromagnetic fields. The beauty of `GEANT4` system is that a lot of built-in physics models describe the interactions of particles with matter very well.

5.9.3 A Description of the Simulation

The `GEANT4` simulation used in the data analysis was first constructed by Brent Perdue [94]. It contained all the materials for BC-501A liquid scintillating detectors, and the detector response function table. All the physics processes are defined in the `LHEP_PRECO_HP` physics list. The simulation was later modified by Wei Chen and myself to describe this 3-body photodisintegration experiment. A description of the simulation is as follows.

Geometry and Materials

The scintillator volume was built within `GEANT4` based on the actual experimental dimensions. Most materials are defined in the standard GEANT library. A picture of the defined geometry can be found in Figure 5.18.

Neutron Generation

Generally speaking, two methods could be employed to generate particles [95]. The first one is the indirect method, by simulating the γ source and using the cross section for the photodisintegration reaction. The second is to directly generate neutron events whose distribution is based on the differential cross section of the three-body photodisintegration reaction. The computational time for the second approach is much less.

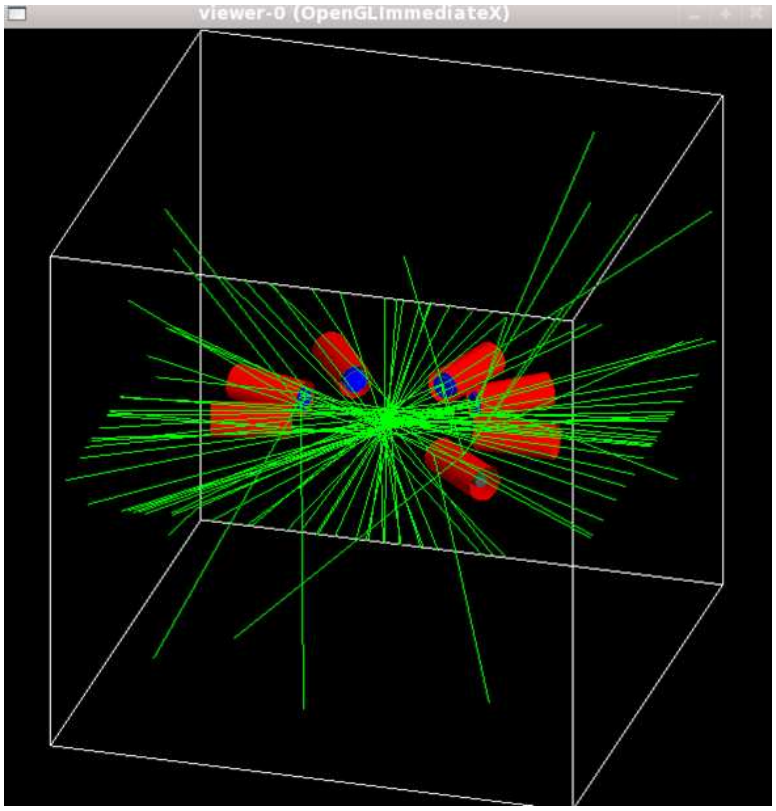

FIGURE 5.18: An overview of the graphic display of the simulation. Target and detectors locations are the same as in the actual experiment.

Neutrons were generated uniformly within the 40 cm long target weighted by the ^{3}He cross section. The differential cross section is provided by Deltuva [33] and it is calculated for every 5 degrees. At each angle, the neutron energies range from 0 to the cutoff[2].

Final Bookkeeping

Once an event is seen by a certain detector, it is registered. The output data file includes the following information of this event: Event ID, incoming neutron energy, neutron TOF, which detector sees this neutron, energy deposit and light output.

[2] In the 11.4 MeV case, the highest possible neutron energy is around 2.6 MeV. But it varies at different angles.

Then the light output is smeared in order to simulate the resolution of the detector. The new light output needs to be above a certain threshold, for example, 0.2 MeV_{ee} to be recorded. Neutrons with light output lower than PH threshold are rejected. The TOF of the event is also smeared to simulate the detector timing resolution. More details about smearing parameters are presented in the next section.

5.9.4 Simulation Calibration

In addition to the basic input of the simulation, additional user routines are used to take care of two important items: light output response function and detector resolutions.

Light output response

The nature of neutral particle detection is a double-edge sword. On the one hand, it makes the PSD technique possible and particle identification much easier; on the other hand, the detector-dependent factors must be taken into account and the light output response (LOR) function is a crucial one. This is because neutrons don't directly deposit energy in the scintillator, instead, it is proton in the hydrogen and carbon which interact with neutrons, producing scintillating photons.

The LOR functions of neutron detectors describe the amount of light obtained from a given amount of energy deposited in the scintillator. Birks [96] uses a parameterization that relates the differential light output dL/dx to the energy loss dE/dx,

$$\frac{dL}{dx} = S\frac{dE}{dx}[1 + kB(\frac{dE}{dx})]^{-1}, \tag{5.23}$$

where S is the absolute scintillation efficiency and kB refers to the quenching [3] of

[3] Light quenching is a phenomenon in which fluorescence emission can be quenched by laser light pulses from modern high repetition rate lasers.

the light output.

Then for a particle of energy E, the total light output can be calculated as,

$$L(E) = \int_0^R \frac{dL}{dx} dx. \tag{5.24}$$

A commonly used conversion relation from proton energy (T_p in MeV) to electron equivalent energy (T_e in MeV$_{ee}$) is from Cecil [97].

$$T_e = a_1 T_p - a_2(1 - e^{-a_3 T_p^{a_4}}), \tag{5.25}$$

where a_i are variables to be determined for each individual case.

Pywell et al. measured and used the light output for a BC-505 detector in the Blowfish detectors [98], a segmented neutron detector consisting of 88 BC-505 liquid scintillator cells. Considerable amount of work was also done at TUNL [99] to determine the detection efficiency. The pulse height is proportional to the total light output from the scintillator and is measured by ADC. For α-particles, the light-output function is described as follows,

$$\begin{aligned} L_\alpha(E) &= 0.017E^{1.6511} : \ E < 6.76MeV \\ &= -0.5319 + 0.0974E : \ E > 6.76MeV \end{aligned} \tag{5.26}$$

Tables of light output response functions were generated for all the likely particles with BC-501A [90]. They are: α, ^8Be, ^9Be, ^{10}Be, ^{12}C, ^{13}C, H, ^2H, ^3He, muon, ^{16}O, pion, triton.

5.9.5 Timing and Energy Resolution

Since the electronics have background noise, timing and energy resolutions are two terms we need to fine tune in the simulation.

First, the light output was smeared according to the following equation(L is before the smearing and L' is after the smearing),

$$L' = L + R(\sigma_1) + R(\sigma_2) \cdot \sqrt{L}, \tag{5.27}$$

where $R(\sigma)$ is a random number sampled from a normal distribution, and $\sigma_1 = 0.005\ MeV$; and $\sigma_2 = 0.077\ (MeV)^{1/2}$ [98].

Energy resolution is determined by the FWHM. The neutron TOF is smeared by a normal distribution with standard deviation to match the experimental readout.

One can determine the overall timing resolution by looking at the gamma flash peak. Since the photons from the target should all arrive at the same time, any broading of the peak would be due to electronics effects [90]. We fit the gamma-flash with a Gaussian to determine an appropriate FWHM.

Similar to the gamma peak, the energy resolution is also obtained from the aluminum plate run which is described in Section 4.4. The variance was varied until the shape of simulation matched the width of the γ-peak.

5.9.6 Detector Efficiency

The detector efficiency as a function of incoming neutron energy depends on the PH threshold applied. Since the neutron is charge neutral, it collides and transfers a fraction of energy to the proton. Depending on the value of PH cut, there is a probability that low energy protons are not detected. This leads to the conclusion that the lower the pulse height, the higher the detection efficiency, and vice versa. Figure 5.19 shows the efficiency as a function of neutron energy with the varying pulse height cut. The simulated data were produced by placing a detector in the path of a pencil-size neutron beam with energies from 0 to 15 MeV.

5.9.7 Comparison with Experimental Data

The simulation is obviously a very complicated one and needs to be checked before being applied to data correction. The method is to compare simulation results with some other existing data.

In order to test whether the light output table can match the experimental data,

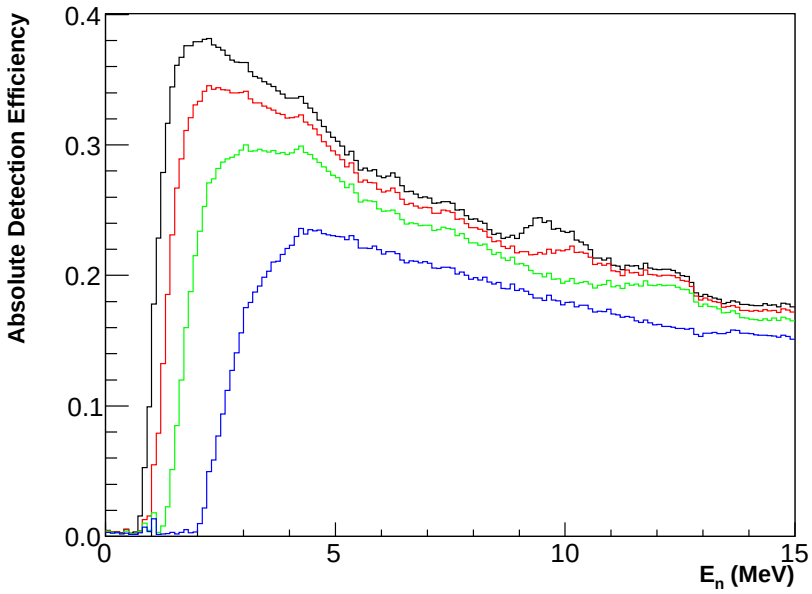

FIGURE 5.19: Neutron detection efficiency as a function of neutron energy. This plot compares the the detector efficiency with four different PH thresholds: 1 Cs (blue), 1/2 Cs (green), 1/3 Cs (red) and 1/4 Cs (black). The lower the threshold is, the higher the detection efficiency is.

we have simulated a 8 MeV neutron pencil beam to compare with the data. Shown in Figure 5.20, the agreement is quite remarkable. The comparison gives us confidence of the light output table we used.

During the experiment, Cs source runs were taken every 3 hours, during the spin flip time interval. The simulation was carried out to match the Cs run data, as shown in Figure 5.3. The agreement is also good, which further lends credibility to the simulation.

5.9.8 Apply Simulation to Data Correction

Here is a summary of the use of GEANT4 simulation.

- Simulate the Cs source run for ADC calibration
- Simulate $^2H(\vec{\gamma}, n)p$ for TDC calibration

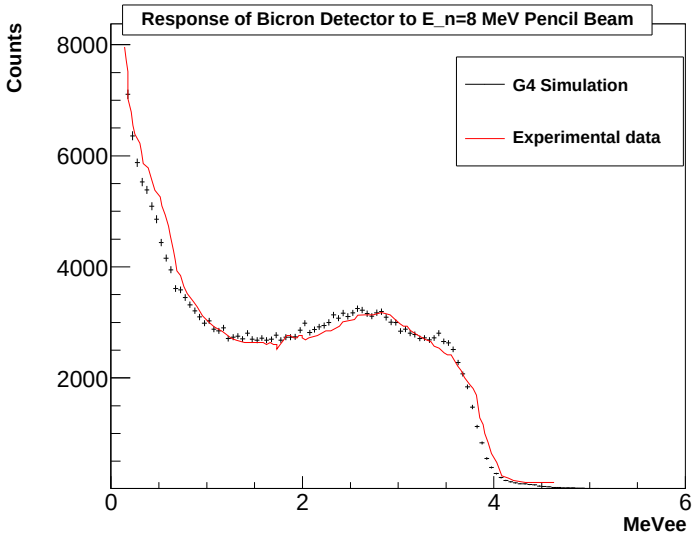

FIGURE 5.20: The comparison between the experimental data and the GEANT4 simulation results. It simulates the response of a BC-501A detector to 8 MeV neutron pencil beam. The data was taken at TUNL [99]. This direct comparison is to check the simulation parameters.

- Simulate the downstream neutron detector efficiency
- Compare the simulation with ^{3}He data to determine the TOF range
- Determine the main detectors convoluted coefficients.

The precise determination of detector efficiency and extended target effect requires GEANT4 simulation. The simulation was performed first with a point target, i.e., neutrons were generated at one fixed point. Then the simulation was performed again with a 40 cm long target, i.e. neutrons were generated within the target cell. By comparing the simulation results and the simulation input file, we can extract the convoluted coefficients, i.e. ratio between the true solid angle and point target solid angle, multiplied by the detector efficiency. The coefficients for ^{3}He spin P and A runs are of the same value, so the correction plays a negligible role in the asymmetry determination. Nevertheless, they are crucial in determining the unpolarized

differential cross section values.

Besides data correction, GEANT4 simulation is also used to study the systematic uncertainties, which are presented in the next section.

5.10 Summary of the Systematic Uncertainty

For any nuclear physics experiment, determining systematic uncertainty is a daunting challenge. The major systematic uncertainties are identified from the three sources: analysis cuts, the HIγS beam and the target.

Uncertainties due to the Analysis Cuts

- **PSD cut** The PSD cut was the most critical among all the cuts. The main goal of this cut is to eliminate background photons and retain as many neutrons from the process of interest as possible. The PSD cut was shifted by $\pm\sigma$ to 5σ and 7σ to compare the impact on the extracted asymmetries and differential cross section.

- **PH cut** As discussed before, the PH cut determines the neutron detector efficiency. The same PH values were applied in the data analysis and in the simulation. The uncertainty in the gain and pedestal determination could result in a mismatch. In this case, the PH threshold was varied by $\pm 5\%$ (from 0.19 MeV_{ee} to 0.21 MeV_{ee}) to observe the change.

- **TOF cut** The leading edge of the TOF window is fixed and the systematic effects of TOF cut comes from the trailing edge. This was studied by varying the low energy cut from 1.0 MeV to 1.2 MeV (approximately $\pm$ 3 ns on TOF) to observe the changes.

Uncertainties due to the Beam

- **Integrated Photon Flux** The estimation of systematics in the integrated photon flux, i.e. the total number of photons on the target during the data taking for each configuration, is a challenge. The systematics of the asymmetry and the differential cross section should be treated differently. As discussed in Section 4.6, in the asymmetry extraction, the integrated flux information is obtained by counting events within the gamma peak as a relative flux measurement. Since the gamma flash stability is around 1%, the systematic uncertainty in obtained by the change of the absolute asymmetry value if the relative normalization changes by 1%.

  For the differential cross section, the integrated photon flux is determined from the back detector monitor counts. We assume the gamma flash is quite stable, and study the standard deviation of the ratios between the back detector counts and the gamma flash counts. This gives us an estimation of how much the back detector counts fluctuate. It is determined to be 7.7%. Another factor which contributes to the integrated photon flux is the uncertainty of the total cross section of ${}^2H(\vec{\gamma}, n)p$, which is determined to be 2.9%.

- **Beam Polarization** We never had a chance to measure the beam polarization. According to FEL staff members, the circular polarization was close to 100%. In this case, we take 5% relative uncertainty in the asymmetry measurement and it has no effect on differential cross sections.

Uncertainties due to the Target

- **Target Polarization** We have already discussed about the target polarization in Section 3.5. Systematics due to NMR measurement is $\sim$3.5%, EPR measurement is $\sim$3.5%, and two methods agree to 4%.

- **Target Thickness** The systematic uncertainty of ^{3}He target thickness is estimated to be around 2%. Two factors contribute to this uncertainty: the first one is due to the density measurement, and the second one is due to the temperature change. We have varied the target chamber temperature by $\pm 10^\circ$ C to determine the change.

5.10.1 Table of Systematic Uncertainties

We present four tables of systematic uncertainties here: $^2H(\vec{\gamma}, n)p$ differential cross section, $^3\vec{H}e(\vec{\gamma}, n)pp$ asymmetry, unpolarized differential cross sections, and the helicity-dependent differential cross section difference. The asymmetry table contains absolute values. This is due to the small asymmetry which makes relative comparsion not meaningful. For other tables, all values are relative values.

Sources	Values at different angles (deg)						
	50.0°	75.0°	90.0°	105.0°	130.0°	145.0°	160.0°
(1a) PSD cut	0.99%	0.15%	0.29%	0.28%	1.97%	1.04%	2.33%
(1b) PH cut	0.93%	0.50%	0.43%	0.78%	1.58%	2.33%	2.26%
(1c) TOF cut	1.52%	0.44%	0.48%	0.69%	2.69%	2.79%	2.1%
1, From analysis cuts	2.04%	0.68%	0.70%	1.08%	3.69%	3.78%	3.86%
(2a) TXS uncertainty	2.9%	2.9%	2.9%	2.9%	2.9%	2.9%	2.9%
2, From HIγS beam	2.9%	2.9%	2.9%	2.9%	2.9%	2.9%	2.9%
(3a) Target thickness	2.0%	2.0%	2.0%	2.0%	2.0%	2.0%	2.0%
3, From target and detector	2.0%	2.0%	2.0%	2.0%	2.0%	2.0%	2.0%
Total Systematics	4.07%	3.59%	3.59%	3.69%	5.1%	5.17%	5.22%

Table 5.9: Systematic uncertainties in the $^2H(\vec{\gamma}, n)p$ differential cross section measurement. All are relative values.

Sources	Values at different angles (deg)						
	50.0°	75.0°	90.0°	105.0°	130.0°	145.0°	160.0°
(1a) PSD cut	0.0264	0.0019	0.0062	0.0045	0.0464	0.0315	0.0037
(1b) PH cut	0.0448	0.0089	0.0188	0.0311	0.0597	0.0504	0.1096
(1c) TOF cut	0.0257	0.0146	0.0123	0.0085	0.0161	0.0084	0.108
1, From analysis cuts	0.0581	0.0172	0.0233	0.0326	0.0774	0.06	0.1539
(2a) Beam Polarization (relative)	5.0%	5.0%	5.0%	5.0%	5.0%	5.0%	5.0%
(2b) Normalization	0.041	0.025	0.024	0.027	0.020	0.033	0.03
2, From HIγS beam	0.041	0.025	0.024	0.027	0.021	0.033	0.030
(3a) Target Polarization (relative)	4.0%	4.0%	4.0%	4.0%	4.0%	4.0%	4.0%
3, From target and detector	0.0037	0.0021	0.0018	0.0047	0.0049	0.0036	0.0019
Total Systematics	0.071	0.030	0.034	0.043	0.080	0.069	0.157

Table 5.10: Systematic uncertainties associated with ${}^3\vec{H}e(\vec{\gamma}, n)pp$ asymmetry measurement. All are absolute values except when indicated explicitly.

Sources	Values at different angles (deg)						
	50.0°	75.0°	90.0°	105.0°	130.0°	145.0°	160.0°
(1a) PSD cut	1.96%	0.29%	1.49%	0.44%	3.17%	4.94%	2.89%
(1b) PH cut	1.82%	2.31%	2.08%	3.41%	6.59%	6.13%	4.4%
(1c) TOF cut	2.01%	2.62%	1.03%	1.24%	7.97%	5.51%	8.85%
1, From analysis cuts	3.34%	3.5%	2.76%	3.65%	10.81%	9.61%	10.29%
(2a) Flux	7.7%	7.7%	7.7%	7.7%	7.7%	7.7%	7.7%
(2b) TXS error	2.9%	2.9%	2.9%	2.9%	2.9%	2.9%	2.9%
2, From HIγS beam	8.2%	8.2%	8.2%	8.2%	8.2%	8.2%	8.2%
(3a) Target thickness	2.0%	2.0%	2.0%	2.0%	2.0%	2.0%	2.0%
3, From target and detector	2.0%	2.0%	2.0%	2.0%	2.0%	2.0%	2.0%
Total Systematics	9.1%	9.1%	8.9%	9.2%	13.7%	12.8%	13.3%

Table 5.11: Systematic uncertainties of ${}^3\vec{H}e(\vec{\gamma}, n)pp$ differential cross section. All are relative values.

Sources	Values at different angles (deg)						
	50.0°	75.0°	90.0°	105.0°	130.0°	145.0°	160.0°
(1a) PSD cut	0.287	0.0387	0.1218	0.0384	0.3189	0.4060	0.0953
(1b) PH cut	0.4622	0.1481	0.4053	0.2333	0.3811	0.5825	2.1965
(1c) TOF cut	0.2763	0.2538	0.2924	0.0844	0.0401	0.0934	2.3903
1, From analysis cuts	0.6104	0.2964	0.5144	0.2510	0.4985	0.7162	3.2476
(2a) Flux	7.7%	7.7%	7.7%	7.7%	7.7%	7.7%	7.7%
(2b) TXS error	2.9%	2.9%	2.9%	2.9%	2.9%	2.9%	2.9%
2, From HIγS beam	8.2%	8.2%	8.2%	8.2%	8.2%	8.2%	8.2%
(3a) Target thickness	2.0%	2.0%	2.0%	2.0%	2.0%	2.0%	2.0%
3, From target and detector	2.0%	2.0%	2.0%	2.0%	2.0%	2.0%	2.0%
Total Systematics	61.6%	30.8%	52.1%	26.5%	50.6%	72.1%	324.9%

Table 5.12: Systematic uncertainties of ${}^3\vec{H}e(\vec{\gamma}, n)pp$ difference in differential cross sections. All are relative values.

6

Results and Discussions

In this chapter, we first present the differential cross section of the ${}^2H(\vec{\gamma}, n)p$ reaction using the D_2 gas target, and then present the asymmetry and unpolarized differential cross section results from ${}^3He(\vec{\gamma}, n)pp$ reaction, followed by the results of the helicity-dependent differential cross section difference and the total cross section.

6.1 ${}^2H(\vec{\gamma}, n)p$ Differential Cross Section at E_γ=11.4 MeV

A differential cross section measurement of the ${}^2H(\vec{\gamma}, n)p$ reaction using a 40 cm long D_2 gas target cell was taken prior to the main experiment. This half an hour run was for calibration purpose. The differential cross sections were extracted using the back D_2O detector for the determination of the integrated photon flux. As mentioned before, the total cross section of ${}^2H(\vec{\gamma}, n)p$ was previously well determined [64]. At 11.4 MeV, the total cross section of this reaction is $1257 \pm 36\ \mu b$ [100]. This reaction is predominantly an electric dipole interaction. In the center of mass frame, the angular distribution of the neutrons is $\sin^2(\theta_{\rm CM})$, therefore the differential cross section at any angle could be determined. The D_2 cross section measurement served as a calibration to make sure that detectors function properly and the analysis procedure is reliable,

etc.

The total number of events would follow the expression,

$$N_n = N_\gamma \cdot N_t \cdot \frac{d\sigma}{d\Omega} \cdot \Delta\Omega \cdot \epsilon. \tag{6.1}$$

The notations were introduced before. The solid angle $\Delta\Omega$ is first assumed the same as that of a point target,

$$\Delta\Omega = \frac{\pi r^2}{d^2}, \tag{6.2}$$

where r is the detector radius, and d is the distance between the center of the detector and the center of the target cell. We need to correct for the solid angle since the D_2 target cell is 40-cm long. In the simulation, the accepted neutrons were obtained through the same cuts described before and corrected for detection efficiency and acceptance.

Detector	Diff. cross section ($\mu b/sr$)	Stat.($\mu b/sr$)	Sys.($\mu b/sr$)
50°	98.9	5.3	4.0
75°	140.2	5.5	5.0
90°	150.0	5.8	5.4
105°	123.8	5.2	4.6
130°	84.2	5.1	4.3
145°	47.3	3.1	2.4
160°	23.7	2.1	1.2

Table 6.1: Differential cross section results of ${}^2\vec{H}(\vec{\gamma}, n)p$ as a function of the neutron angles in the CM frame, together with statistical and systematic uncertainties.

The integrated flux information is based on the average value of the two downstream detectors. The differential cross section we calculate is in the lab frame and has to be converted to the center of mass (CM) frame. This conversion is based on the fact that the same number of particles are scattered into the solid angle $d\Omega_{CM}$

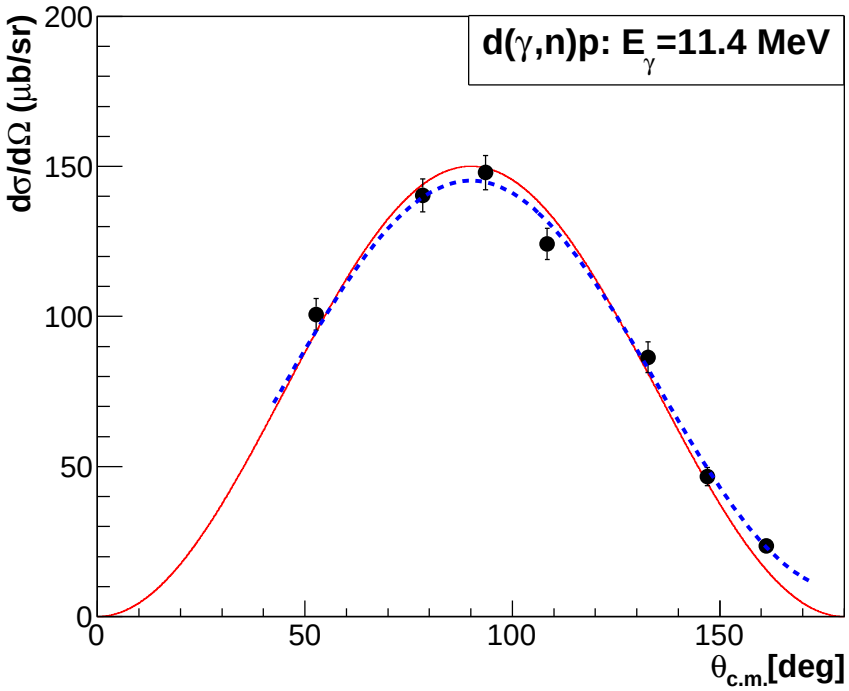

FIGURE 6.1: The differential cross section of ${}^2H(\vec{\gamma}, n)p$. There are two fitted curves: the red solid one is assuming the angular distribution in the format of $A\sin^2(\theta_{\rm CM})$, and the blue dotted one is assuming the angular distribution in the format of $B\sin^2(\theta_{\rm CM})+C$, both using the total cross section value 1257 μb. The solid circles are the data points from this measurement with statistical uncertainties only.

at θ_{CM}, and solid angle $d\Omega_L$ at θ_L in two different frames. Let's write down the equation,

$$(\frac{d\sigma}{d\Omega})_{CM} sin\theta_{CM} d\theta_{CM} d\phi_{CM} = (\frac{d\sigma}{d\Omega})_L sin\theta_L d\theta_L d\phi_L. \tag{6.3}$$

Since there is rotational symmetry, ϕ terms is cancelled out. We rewrite the equation,

$$(\frac{d\sigma}{d\Omega})_{CM} = (\frac{d\sigma}{d\Omega})_L |\frac{dcos\theta_L}{dcos\theta_C}|. \tag{6.4}$$

The ratio on the right hand side is the Jacobian of the transformation. Therefore,

the relationship between the two differential cross sections is,

$$(\frac{d\sigma}{d\Omega})_{CM} = (\frac{d\sigma}{d\Omega})_L \frac{1+\gamma cos\theta_{CM}}{(1+2\gamma cos\theta_{CM}+\gamma^2)^{3/2}}, \tag{6.5}$$

where

$$\gamma = (\frac{m_1 m_3}{m_2 m_4}\frac{E}{E+Q})^{1/2}, \tag{6.6}$$

where m_1 is the incoming particle mass, m_2 is the mass of the initial rest particle, m_3 and m_4 are masses after scattering. E is the total initial energy of the two particles in the CM frame and Q-value refers to the amount of mass converts to kinetic energy of the final states.

Figure 6.1 shows the unpolarized deuteron differential cross section as a function of $\theta_{c.m.}$ together with the expected angular distribution. As seen from the plot, the overall agreement is very good. Using $Asin^2\theta$ fit, we obtained $A = 148.9 \pm 2.8$. The total cross section is therefore $\sigma = 1248 \pm 23\mu b$. The aforementioned fit only takes electric dipole (E1) transition into account. In order to take the magnetic dipole (M1) transition into account, we used the formula $B + Csin^2\theta$ to fit again. The fitted parameters are: $B = 9.5 \pm 2.2$, $C = 134.6 \pm 4.3$, and the total cross section is $\sigma = 1247 \pm 45\mu b$. Compared with the world data $1257 \pm 36\mu b$, the good agreement demonstrates that the detectors were functioning well and the analysis procedure were solid, thus we have more confidence to proceed to the ^{3}He data analysis.

6.2 $^3\vec{H}e(\vec{\gamma}, n)pp$ Physics Asymmetry Result at E_γ=11.4 MeV

Figure 6.2 shows the extracted physics asymmetry as a function of the neutron scattering angles from 50° to 160° in the lab frame, integrated over neutron kinetic energy range above 1.1 MeV. The rather large statistical uncertainties are due to two reasons. One is the relatively short data taking time and the other is very high background rates observed in our experiment, as explained in the previous chapter.

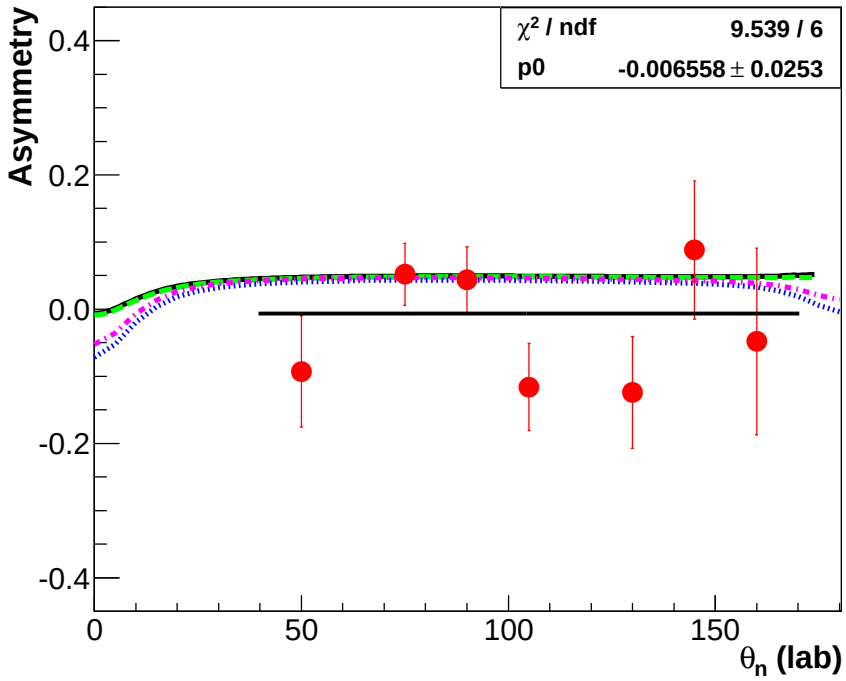

FIGURE 6.2: The physics asymmetry A as a function of neutron lab angles. The solid circles are the data points from this measurement with statistical uncertainties only. Two sets of calculations include four dynamic inputs: AV18 (Blue) and AV18+Urbana IX (Purple) from Golak [23]; CD Bonn (Green) and CD Bonn + Δ-isobar (Black) are from Deltuva [28].

Our asymmetry results are compared with two sets of calculations performed by two groups. Skibinski and Golak [47, 48] did their calculations by solving three-body Faddeev equations with the AV18 potential alone or supplemented with the 3NF-Urbana IX (UIX) [7], including explicit π- and ρ-meson exchange currents. Deltuva's calculations were based on the Alt-Grassberger-Sandhas (AGS) equation [27], and employed CD Bonn potential with Coulomb interaction between the two protons as a pure nucleonic reference and two-baryon coupled-channel CD Bonn +Δ with Coulomb. It is observed from Fig. 6.2 that the calculated asymmetry remains almost unchanged by the inclusion of the Δ-isobar, and this means there is no significant Δ-isobar effect at this energy. In contrast, a larger UIX 3NF effect is shown. There

are two reasons for this. First, UIX has a larger 3NF effect on trinucleon binding and subsequent scaling. Second, the calculations have different computational approaches. Overall, the effect due to the three-body force is still small in the calculated asymmetry.

The seven data points were fit by a straight line, i.e."pol0" fit. The fitted value was -0.0066 ± 0.0253. The χ^2/ndf=9.539/6, so the statistical uncertainty is $0.0253 \times \sqrt{9.539/6} = 3.2\%$. This is the first asymmetry result and agrees with theory to within 2σ. However, given the experimental uncertainty, our data can not differentiate one set of calculation from another. Therefore, it is important to have smaller uncertainties in future measurements.

Detector	N_P	N_A	Asymmetry	Statistical	Systematic
50°	4937	5385	-0.094	0.083	0.071
75°	5461	5708	0.052	0.046	0.030
90°	4573	4787	0.044	0.049	0.034
105°	3439	3787	-0.117	0.065	0.043
130°	1190	1336	-0.124	0.083	0.080
145°	1901	1968	0.089	0.103	0.069
160°	896	975	-0.049	0.139	0.157

Table 6.2: Asymmetry results of ${}^3\vec{H}e(\vec{\gamma}, n)pp$ from this experiment as a function of the neutron angle in the lab, together with the statistical and systematic uncertainties. N_P and N_A refer to the numbers of neutron events after all the cuts.

6.3 ${}^3He(\vec{\gamma}, n)pp$ Unpolarized Differential Cross Section Result at E_γ=11.4 MeV

The unpolarized differential cross section is extracted by averaging the parallel-spin and antiparallel-spin differential cross sections. It is defined as,

$$\frac{d\sigma}{d\Omega} = \frac{(N_P + N'_A)/2 - N'_N}{N^P_\gamma \cdot N_t \cdot \varepsilon}, \tag{6.7}$$

where N_P, N'_A and N'_N are defined before. N^P_γ is the integrated photon numbers extracted using the downstream detectors in spin parallel runs. N_t is the target thickness. ε is the detector acceptance which includes both the extended target effect and the detector efficiency extracted from the simulation.

Figure 6.3 shows the extracted unpolarized differential cross section as a function of the neutron lab angle. The four different theory curves are from the same calculations in the asymmetry analysis. The top two curves are from AV18 with and without the Urbana IX force. They predict larger differential cross section values than CD Bonn with and without Δ-isobar.

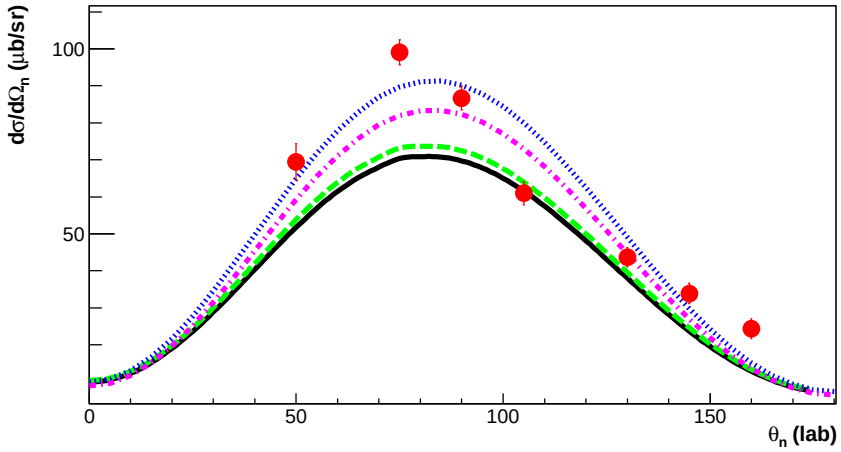

FIGURE 6.3: The extracted unpolarized differential cross section as a function of neutron lab angles. The solid circles are the data points from this measurement with statistical uncertainties only. Two sets of calculations include four dynamic inputs: AV18 (Blue) and AV18+Urbana IX (Purple) are from Golak [23]; CD Bonn (Green) and CD Bonn + Δ-isobar (Black) are from Deltuva [28].

It is important to point out that the differential cross section data are model-dependent. Recall that the TOF cut starts from 1.1 MeV, which means all neutrons with energy below this threshold are cut away. Therefore, one needs to address the model dependent uncertainty in addition to other systematic studies. The way that

Det.	Deltuva	Golak	DXS diff($\mu b/sr$)	Method I	Method II
50°	0.65	0.73	7.4	6.2%	3.7%
75°	0.66	0.75	11.5	6.8%	3.9%
90°	0.66	0.74	12.8	6.1%	5.0%
105°	0.64	0.73	11.4	7.0%	6.7%
130°	0.59	0.68	6.6	7.6%	6.2%
145°	0.53	0.62	3.3	8.5%	4.6%
160°	0.4	0.49	0.74	11.3%	1.8%

Table 6.3: Model dependent study of the unpolarized differential cross section of ${}^3He(\vec{\gamma}, n)pp$. The second and third columns list the ratios of the number of neutrons with energy higher than 1.1 MeV to the total number of events in different calculations (see text). The fourth column is the DXS difference between these two. The fifth and sixth columns give out the uncertainty using two different methods which are described in the main context.

Det.	N_N	DXS($\mu b/sr$)	Stat.($\mu b/sr$)	Sys.($\mu b/sr$)	Mod.($\mu b/sr$)
50°	1758	69.4	4.9	6.3	3.4
75°	1361	99.1	3.4	9.1	5.3
90°	1117	86.7	3.3	7.7	4.8
105°	973	61.0	3.1	5.6	4.2
130°	286	43.7	2.7	6.0	3.0
145°	579	33.9	2.8	4.4	2.2
160°	252	24.4	2.7	3.2	1.6

Table 6.4: Differential cross section results of ${}^3He(\vec{\gamma}, n)pp$ as a function of the neutron angle in the lab, together with statistical and systematic uncertainties. N_N refers to number of neutrons from the background including N_2. N_P and N_A are shown in the asymmetry table.

the detector acceptance ε corrects for the unmeasured part is described as follows: in the `GEANT4` simulation, the input neutrons are generated with energies ranging from 0 to the maximum possible E_n values, and the output neutron events are analyzed with the same PH and TOF cuts as those applied to the data. The ε is then extracted using the entire input neutron energy spectrum to account for the unmeasured region. The theoretical curves presented are also from $E_n = 0$ and up.

Since we actually measure neutrons with energies above 1.1 MeV, we depend on two different calculations from Deltuva (CD Bonn) and Golak (AV18) to extract the unmeasured part. Two different methods are used to extract this model-dependent uncertainty. The first one is to directly compare the ratios of the number of events with energy above 1.1 MeV to the total number of events from these two calculations, then take half of the difference between the two as the model-dependent uncertainty of the unpolarized differential cross sections. The second method is to compare the unpolarized differential cross sections in two theories, then multiple by the fraction of the unmeasured neutrons. The uncertainties from these two methods are presented in Table 6.3. The final uncertainty is based on the average of the two. The unpolarized differential cross section results, together with statistical, systematical and model dependent uncertainties are listed in Table 6.4.

As we can see, the overall agreement between the theoretical predictions and the experimental results is reasonable. At the forward and backward angles, the data agree more with Golak and at 105° and 130° more with Deltuva. The largest discrepancy is at 160°, the most backward angle. We have investigated the discrepancy at certain angles. First of all, they could be due to the contamination from the leak-in photons. We have revisited the particle identification procedure (PID) process and double checked the systematic study, and we are confident about the cuts applied. Secondly, an important factor that could result in the discrepancy has been addressed in Chapter 4: a PH cut of 0.2 MeV_{ee} makes most neutrons fall in the region where efficiency curve changes rapidly. Improved measurement in the near future with better absolute integrated photon flux measurement at higher photon energies is essential to provide a more stringent test of the theory.

6.4 Helicity-dependent differential Cross Section Difference Result at E_γ=11.4 MeV

The helicity-dependent differential cross section difference is calculated via the following formula,

$$(\frac{d\sigma}{d\Omega})_P - (\frac{d\sigma}{d\Omega})_A = \frac{N_P - N'_A}{N^P_\gamma \cdot N_t \cdot \varepsilon}. \tag{6.8}$$

Helicity-dependent differential cross section difference is proportional to the product of the asymmetry and the unpolarized differential cross section. Figure 6.4 plots the helicity-dependent differential cross section difference and Table 6.5 lists all the values as well as the associated uncertainties. The statistical uncertainties are dominated by the statistical uncertainties in the asymmetry measurement. In the future, we need to have better measurements at 11.4 MeV and other higher energies in order to extract the GDH integral value.

Detector	DXS diff.($\mu b/sr$)	Statistical ($\mu b/sr$)	Systematic($\mu b/sr$)
50°	-12.9	11.5	8.0
75°	10.3	9.1	3.2
90°	7.7	8.6	4.0
105°	-14.3	7.9	3.8
130°	-10.9	7.2	5.5
145°	6.0	6.9	4.3
160°	-2.4	6.8	7.7

Table 6.5: The differential cross section difference as a function of the neutron lab angle, together with statistical and systematic uncertainties.

6.5 $^3He(\vec{\gamma}, n)pp$ Total cross section result at E_γ=11.4 MeV

Although we only have seven unpolarized differential cross section data points, we are still very interested in extracting the total cross section. In order to do so, we

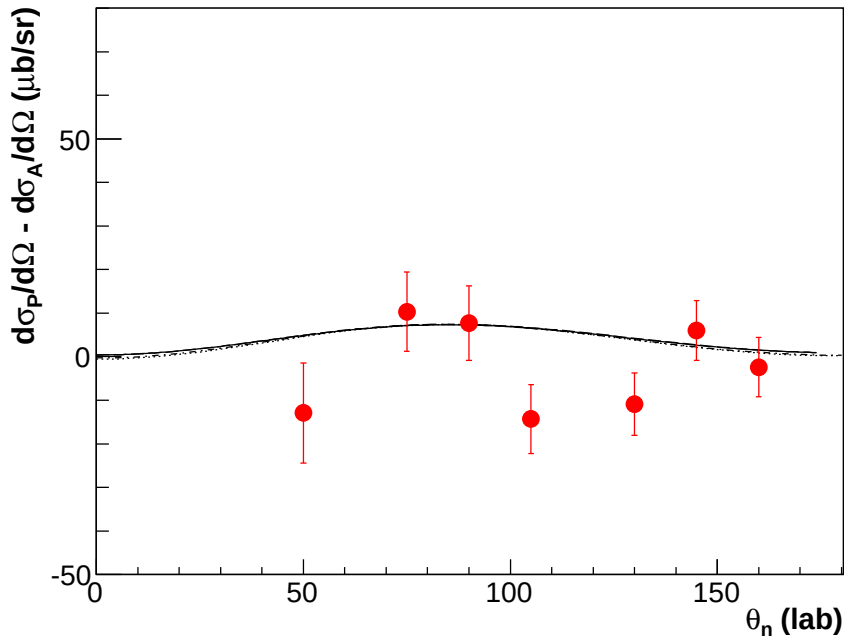

FIGURE 6.4: The helicity-dependent differential cross section difference at various neutron lab angle together with the four theoretical results presented previously in Figs. 6.2 and 6.3. The solid circles are the data points from this measurement with statistical uncertainties only.

took two different approaches. The first one is to assume the differential cross section distribution has the same shape as that of the theoretical prediction [23], and fit the experimental data using the theory curve. The fit constant is about 1.054, which then multiply by the theoretical total cross section (AV18+Urbana IX, 725.2 μb) to get the experimental total cross section. The second is to assume that the differential cross section can be written as an expansion in terms of Legendre Polynomials up to third order.

$$\frac{d\sigma}{d\Omega}(cos\theta) = a_0 P_0(cos\theta) + a_1 P_1(cos\theta) + a_2 P_2(cos\theta) + a_3 P_3(cos\theta), \tag{6.9}$$

where

$$P_0(cos\theta) = 1$$
$$P_1(cos\theta) = cos\theta$$
$$P_2(cos\theta) = (3cos\theta^2 - 1)/2$$
$$P_3(cos\theta) = (5cos\theta^3 - 3cos\theta)/2 \quad (6.10)$$

When we integrate the differential cross section to extract the total value, the higher order terms become zero when they are integrated over the solid angle. Therefore, the only term that matters is a_0, which is about 61.7. We multiply a_0 by 4π to get the total cross section. Table 6.6 lists the fit coefficients. A detailed discussion of the angular distribution coefficients was published by Weller.*et al* [101].

Parameters	Fit values (μb)
a_0	61.7 ± 2.9
a_1	14.2 ± 4.7
a_2	-44.6 ± 5.0
a_3	-21.9 ± 6.1

Table 6.6: The fit parameters of the total cross section.

The extracted values from these two methods agree with each other to within 11 μb. The final result based on the Legendre Polynomial expansion method on the extracted total cross section is 776±18 (stat.)±32 (sys.)±19 (mod. A)±11 (mod. B) μb. Model uncertainty type A refers to the uncertainties in correcting for the unmeasured neutrons with energy below 1.1 MeV (see section 6.3), and Model uncertainty type B refers to the two different approaches used to extract the total cross section.

Fig. 6.5 shows the world data on the total cross section of the three-body photodisintegration of ^{3}He for an incident photon energy range of about 10 - 24 MeV together with two sets of theoretical predictions. While the agreement between our

result and the theory at 11.4 MeV is good, the recent measurement [24] at 10.2 MeV is only about one third of the theoretical value. Future data in this energy region is crucial to clarify the situation.

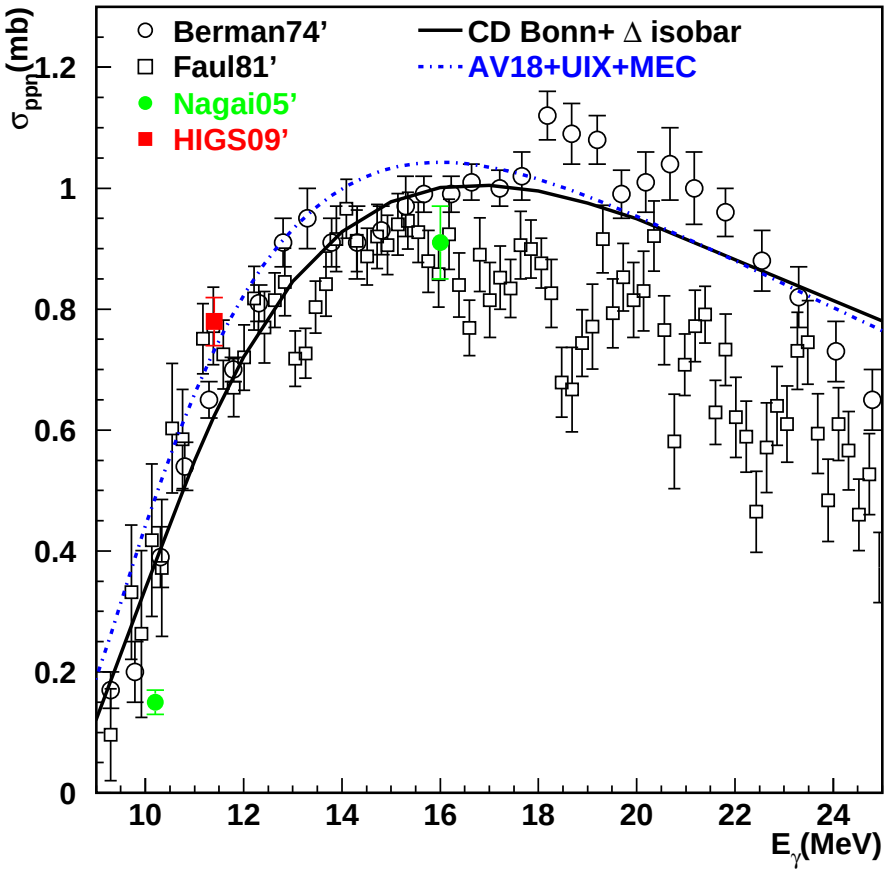

FIGURE 6.5: The total cross section of three-body photodisintegration. The square red point is from this measurement with the Legendre polynomial fit. Two green solid circles are from Nagai 2005 measurement. Other data points include all previous measurements. Data are compared to two theoretical curves: CD Bonn+Δ isobar (solid line), AV18+UIX+MEC (dot-dashed line).

7

May 2009 Test Run

7.1 New Developments since May 2008 Asymmetry Measurement at HIγS

Following the experiment in May, 2008, a new high pressure ^{3}He cell made of pyrex glass coated with a thin layer of pure aluminosilicate glass has been fabricated and tested [102]. The coating technique was first invented by Cates *et al.* at University of Virginia (UVA) by doping the aluminum nitrate nonahydrate ($Al(NO_3)_3 \cdot 9H_2O$) to the solution produced by the Sol-gel process [103]. Several smaller single pyrex cells produced using the Sol-gel technique yielded longer relaxation times than those from uncoated cells. This is the first time that this technique has been applied to a high pressure ^{3}He target, a double cell system with a much larger volume. The smooth, relatively paramagnetic-free aluminosilicate glass coated surface reduces the ^{3}He relaxation from magnetic impurities in the glass wall. Its low ^{3}He permeability helps prevent loss of ^{3}He atoms for long term operation at typical temperatures of spin exchange optical pumping (180° C for Rb-only-cells and 230° C for Rb-K hybrid cells). The high background rates from GE180 glass is expected to be highly suppressed since the coating thickness is on the order of microns. The cell was made

by Mike Souza from Princeton University, coated by Cates *et al.* and filled with ^{3}He by Averett *et al.* at the College of William and Mary. This new Rb-K hybrid ^{3}He gas target cell has the same dimensions as the GE180 cell previously used at HIγS, and contains 5.16 ± 0.29 amagats ^{3}He gas.

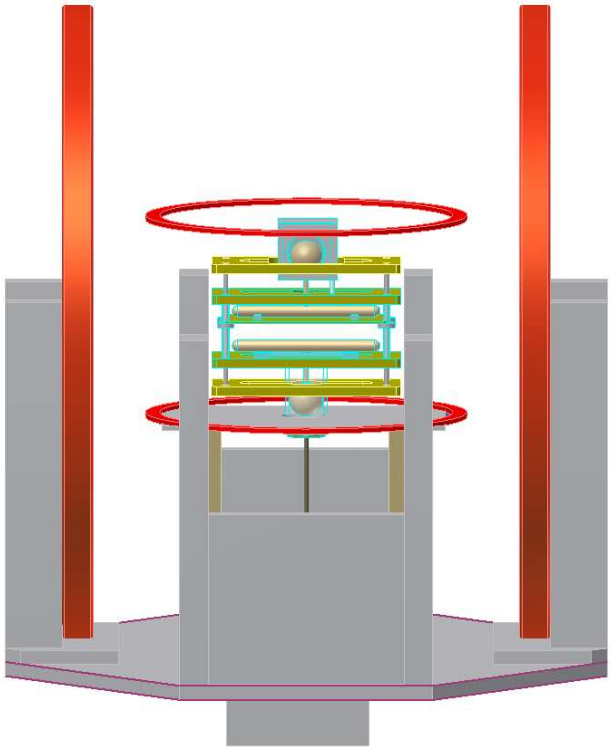

FIGURE 7.1: The design of a movable ^{3}He target. A large octagon support serves as the base. Two Helmholtz coils stand on both sides to generate a uniform magnetic field in the target cell region. The movable stand sits in the center of two RF coils which are placed parallel to the ground.

As mentioned in the Chapter 4, a N_2 reference cell with the same dimension as that of the target cell was used for background subtraction. The ^{3}He cell and the N_2 cell were interchanged frequently during the data taking at HIγS. This was done manually in the spring of 2008, which was inconvenient and inefficient. A computer controlled target motion system has been designed and assembled. Fig. 7.1 shows

the design of the target motion system. The ^{3}He and the N_2 cells are placed on the system and can move up and down together, in and out of the gamma beam by a motor-controlled support. When the N_2 cell is in the gamma beam line, the ^{3}He target is $\sim$ 11.5 cm above it while being polarized by the laser system at the same time, significantly reducing the overhead of the data taking.

7.2 Test Run: Setup and Findings

In May 2009, a test run of the unpolarized pyrex ^{3}He target "Bolt" was carried out at HIγS. This test run used a circularly polarized γ beam at an incoming energy of 11.4 MeV. Figure 7.2 shows the experimental setup including a motor controlled six-layer support and three detectors placed at 50°, 90°, 130° and 90 cm, 75 cm, 90cm away with respect to the center of the target. Two experimental issues were found during the measurement. One was that the photon flux was only 1.5×10^7/s, much lower than what we requested for the test, resulting in poorer statistics. The second was due to another experimental apparatus in the upper stream beamline, the ^{3}He target set up for the test was not ideal: the target was about 2 m downstream compared to the position in May 2008's experiment. This gave rise to problems including long air paths and the rather short distance to the downstream D_2O target which generated considerable background neutrons.

Table 7.1 lists six different targets on different layers and their allocated beam time in one cycle. Each cycle took 30 mins. The purpose of these targets are as follows: the aluminum plate was used to locate the γ-peak position in the TDC spectrum. The liquid D_2O target was to test the detector settings. The empty/air run was important because it would directly measure neutrons from scattering in the open air path. The D_2 gas cell had the same purpose as liquid D_2O except that the target thickness was much smaller. The N_2 gas cell was used for background subtraction. The ^{3}He cell "Bolt" was given half of the running time because the

FIGURE 7.2: (Left) The six layer support is attached to the automated motor control. A web camera was set up to monitor the movement of the support to make sure the right target cell was in place. (Right) A close look at the six layer support. From top to bottom: aluminum plate, liquid D_2O target, completely empty/air, D_2 gas target, N_2 gas target and ^3He target. The three lower targets have end caps attached to both ends for initial alignment.

main goal of the run was to test this new pyrex cell.

Targets	Allocated running time (min)
Al plate	1
D_2O	2
Empty/Air	2
D_2 Gas	5
N_2 Gas	5
^3He	15

Table 7.1: Six different targets and their allocated beam time. One complete cycle of data taking took 30 minutes.

As expected, the pyrex glass generated fewer background events, the neutron yield was 20% lower than that from the GE180 cell. Figure 7.3 shows the comparison between two different N_2 cells. There are two major differences between these two cells. First, the glass materials are different: one is pyrex (but not Sol-gel coated. Only "Bolt" was Sol-gel coated.) and the other is GE180. Second, one is a double cell system, and the other only has a target chamber. Since the pumping chamber is not placed in the photon beam anyway, a direct comparison between the two yields would shed light on the difference between the two glass materials. As seen from Figure 7.3, in most energy bins, the pyrex cell has ∼20% fewer events.

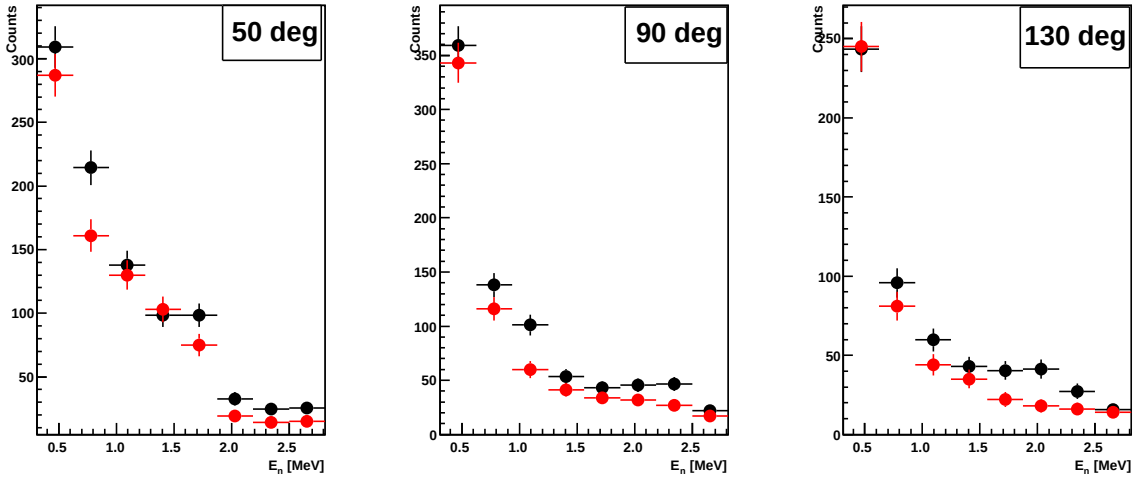

FIGURE 7.3: Comparison between N_2 GE180 (top, black) and N_2 pyrex (bottom, red) targets. In most energy bins, the number of events is reduced by ∼20% in the pyrex N_2 cell.

A comparison between ^{3}He GE180 ("Linda") and Sol-Gel coated pyrex ("Bolt") targets was also made. Since "Linda" had a larger ^{3}He number density than "Bolt", we used the following expression to extract the yield of the pressure scaled "Bolt":

$$(Y_{Bolt} - Y_{N_2}) \times 7.27/5.24 + Y_{N_2}, \tag{7.1}$$

where Y_{Bolt}, Y_{N_2} refer to the normalized yields of "Bolt" and N_2 pyrex targets. It is

observed that the pyrex cell yields fewer background neutrons, which is in agreement with the N_2 cell case.

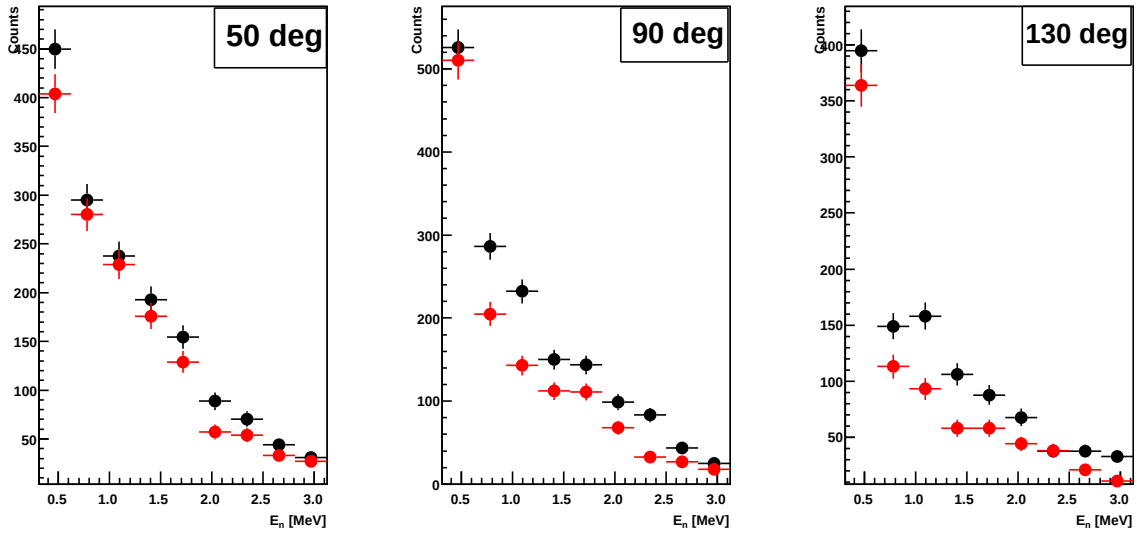

FIGURE 7.4: Comparison between GE180 ("Linda", top, black) and Sol-Gel coated pyrex ^{3}He ("Bolt", red, bottom) targets. The yield is scaled by the back detector counts.

What we have also learned from this test run includes the following: first of all, stable and high flux (at least 5×10^7/s) is important for obtaining good statistics. Second, the knowledge of relative flux measurement needs to be understood better than 1% which is crucial for helicity-dependent cross section difference measurements. Third, the downstream D_2O target needs better shielding from neutrons. Finally, a vacuum pipe between the beam source and the target is absolutely necessary because it helps reduce scattering from the air.

8

Summary and Future Outlook

8.1 Summary

In summary, this thesis presents a first study of three-body photodisintegration of ^{3}He with Double Polarizations at an incident energy of 11.4 MeV. The results are compared to the three-body calculations using both CD Bonn and AV18 potentials and are in agreement within limited statistics.

This measurement was carried out at the HIγS facility located at Duke University. The γ-rays were produced using the intra-cavity backscattering of a free electron laser. The γ-rays were 100% circularly polarized and the incident flux intensity was $\sim 5\times10^7$/s, with an energy spread of $\sim$3% at 11.4 MeV.

This measurement used a high-pressure polarized ^{3}He target and this target was based on spin-exchange optical pumping of hybrid alkali. Two methods NMR and EPR were used to measure the ^{3}He polarization, which was determined to be $\sim$ 42.0% $\pm$ 1.6%. The ^{3}He nuclear spin was aligned parallel and antiparallel to the incident γ-ray momentum direction to form the spin asymmetry measurement.

The neutrons from $^3\vec{H}e(\vec{\gamma}, n)pp$ reaction were detected using seven liquid scintil-

lating detectors with excellent pulse-shape discrimination properties between γ-rays and neutrons. The detectors were placed between 75 and 90 cm from the center of the target and at laboratory scattering angle of 50, 75, 90, 105, 130, 145 and 160 degrees. The PSD, PH and TOF information was recorded for each detector.

To select neutrons from the reaction, four cuts were applied. They were multiplicity, PSD, PH and TOF cuts. Normalization is a challenging part in the data analysis. In the asymmetry extraction, we took a new approach based upon the fact that each neutron detector was also a photon detector. For each run, events within the photon peak of each detector were counted. Then, by subtracting the sideband events, a relative measure of the integrated photon flux was obtained. Back detector counts were mainly used for the extraction of the unpolarized differential cross sections.

Results are compared with two sets of calculations performed by two groups. One calculation solves three-body Faddeev equations with the AV18 potential alone or with the 3NF-Urbana IX (UIX), including explicit π- and ρ-meson exchange currents. The other calculation was based on the AGS equation, and employed CD Bonn with and without Δ, including the Coulomb interaction between the two protons. Our measured asymmetry results are in agreement within limited statistics. However, our data can not differentiate one set of calculations from another.

The unpolarized differential cross section and the helicity-dependent differential cross section differences are also presented and compared to the same theoretical calculations. Some discrepancy was observed. An improved measurement in the near future with better absolute integrated flux measurement is essential to test the theory.

The total cross section is finally extracted from the seven unpolarized differential cross section data points. Two approaches are employed: one is to assume the differential cross section distribution has the same shape as that of the theoretical

prediction, and fit the experimental data using the theory curve. The other is to expand the differential cross section in terms of the Legendre Polynomials up to third order. The extracted result is much closer to Golak's calculation, compared with the 2005 Nagai measurement at 10.2 MeV, which was 1/3 of the theoretical prediction.

8.2 Future Prospects

This measurement at 11.4 MeV is just the beginning of the study of ^{3}He photodisintegration at HIγS. A new proposal was submitted and defended in June 2009 [104] and has been approved by the HIγS program advisory committee (PAC) in July 2009.

We requested a total of 240 hours of 100% polarized photon beam. The most important part in making projections is to calculate the statistical uncertainty. A detailed description of the statistical uncertainty is given in Section 5.8. In making the projections, we assumed a simplified expression:

$$Error = \frac{1}{P_b \cdot P_t \cdot \sqrt{2N_n}}, \tag{8.1}$$

where N_n is the total number of neutron events in one spin-state. Table 8.1 lists all the parameters for the beam and target that we use in making the projection. For simplicity, we assume it is a point-like target. The statistical uncertainties of seven angles at 11.4 MeV are estimated to be between 1.01% and 2.70%, where neutron counts at the backward angles have the largest uncertainties, as shown on the left side of Figure 8.1. On the right side of Figure 8.1, we calculate the asymmetry values based on the total cross section values from Deltuva [33]. Besides the point target assumption, the detector efficiency is taken to be 20%. The statistical uncertainties for these four points are between 0.5% and 0.7%.

E_γ (MeV)	Flux (/sec)	$\frac{\Delta E}{E}$(%)	P_{beam} (%)	P_{target} (%)	Beam time (hrs)
11.4	8×10^7	3.0	100.0	60.0	60
20.0	8×10^7	3.0	100.0	60.0	60
30.0	5×10^7	3.0	100.0	60.0	60
40.0	5×10^7	3.0	100.0	60.0	60

Table 8.1: Parameters for the projection of the proposed measurements.

Besides the asymmetry measurement, a direct measurement of the GDH integrand is of great interest. Right now a 5-Paddle system is under development [105] at HIγS, which will make the absolute flux measurement more reliable. The ultimate goal is to measure the GDH integrand up to pion production threshold, so that it provides more stringent tests of the theory.

HIγS PAC rated our proposal "very good" and granted us a total of 180 hrs to run three measurements below 30 MeV. They suggested that since the peak of the GDH integrand is $\sim$ 16 MeV, as shown in Figure 8.2, we should pick one energy point on each side of the maximum, and another energy point around 30 MeV to "capture the fall-off". Beam time for the future experiment could be as early as in 2010.

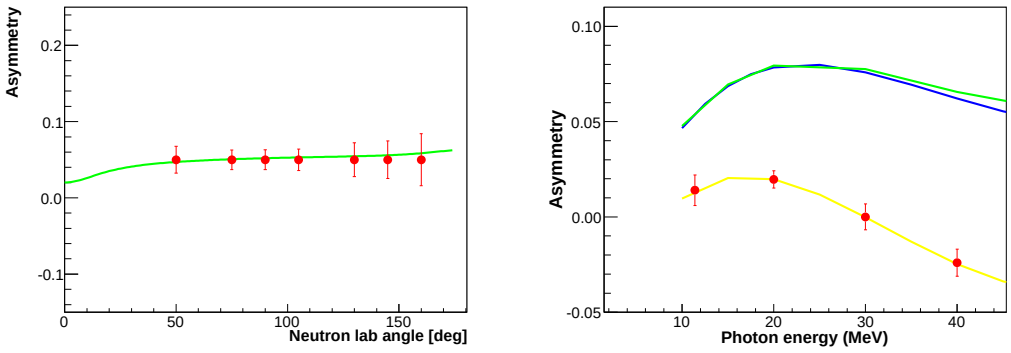

FIGURE 8.1: (Left) Projection for asymmetry measurements at $E_\gamma = 11.4$ MeV. (Right) Projection for total asymmetry measurement as a function of incident photon beam energy. The theory curves are labeled in the same way as in Figure 1.1.

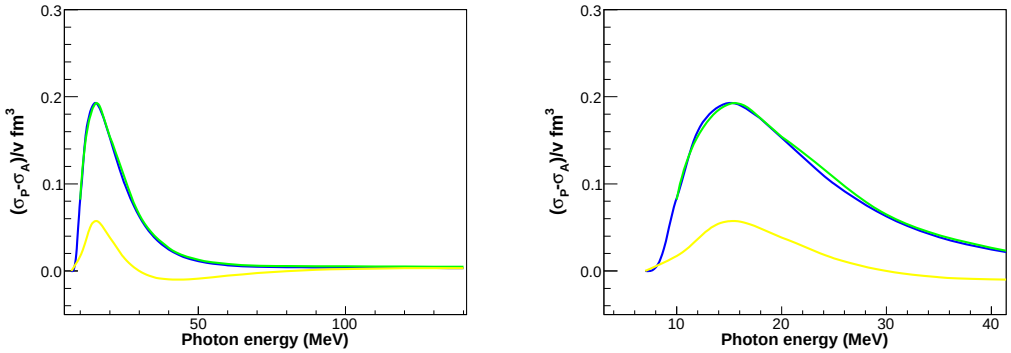

FIGURE 8.2: (Left) Three-body GDH integrand as a function of photon energy (E_γ) up to 140 MeV. Again, the theory curves are labeled in the same way as in Figure 1.1. (Right) The integrand up to 40 MeV dominates the total integrand, with interesting peak feature around 15 MeV.

Appendix A

EPR Measurement Procedure

The EPR measurement is a challenging task. The following precedure is based on a few good technical notes [106, 87] and modified for our own measurement.

A. Photodiode and lock-in Amplifier

- Adjust the position of the PIN diode so that it looks directly at the light beam coming from the cell.
- Measure the PIN diode output, it should be a DC signal with an amplitude between 100 mV ∼250 mV. If the signal is less than 100 mV, then check the light and PIN diode again, also check the windows and the RF coil.
- Set-up the lock-in amplifier parameter: AC-Gain: 10 dB; Sensitivity: 200 uV ∼2mV; Time constant: 100 ms.
- Connect PIN diode to the lock-in amplifier input.

B. Modulation Source (HP 3312A)

- Function: sine wave

- Sweep/modulate: No sweep or modulation
- Frequency: 200 Hz (this frequency is arbitrary. 200 Hz is a good choice since it is far away from most noise sources)
- Amplitude: $\geq$0.4 Vpp for polarization 30%, 1.0 Vpp for $\geq$ 40% (Vpp=Volts peak-to-peak), amplitude depends on the attenuation.
- HP 3312A Vp-p goes to PI circuit "V mod", HP 3312A "sync" to Lock-in Amplifier "ref in".
- Make sure PI box is unplugged because we need to first find EPR resonance without PI box.

C. Sweep Generator (HP 3314A Function Generator)

- Frequency: we need to find frequency, it changes with temperature and holding field, usually at 11.65 MHz (the EPR RF field is swept at a frequency of 200 Hz). The RF function generator needs to be set 10 kHz higher than resonance.
- Amplitude: the voltage is chosen to be between 5-10 V.
- Modulation Mode: VCO. VCO changes the frequency of the function generator based on the input.
- Connect PI circuit output to HP 3312A VCO.
- Connect HP 3314A sync out to Agilent 53132A Counter. Connect HP 3314A output to the cable leading to EPR coils.

After EPR lineshape measurement, it is time for EPR polarization measurement

1. Connect Lock-in amplifier channel 1 output (from rear panel) to PI circuit in.

2. To find the EPR resonance frequency, it is a two-step process:

   a. Manually adjust the HP 3312A frequency with the smallest step 0.01MHz, while observe the lock-in. We need to do this before plugging in PI Box.

   b. We should be able to observe the lock-in signal changing when adjusting the frequency. It should show a maximum ($\geq$0, peak) followed by a minimum ($\leq$0, dip), or vice versa. The resonance is in between them when the lock-in signal is small. Keep in mind that lock-in will read zero when it is far from resonance as well, so look for the characteristic resonance behavior

3. PI feedback box is always on.

4. Observe the V_{out} of PI circuit on an oscilloscope. If it is "jumping around" erratically, the gains must be adjusted. We need to start with the sensitivity on the lock-in, also if it is not locking need to adjust phase (+180°).

5. If the variation on the lock-in is big, then one possible solution is to increase the sensitivity.

6. Once this is done, the circuit should track the resonance frequency and the counter reading should change towards it. The lock-in signal should be stabilized to a minimum.

7. Wait until the counter reading is stabilized, change HP 3312A frequency manually by 0.01 MHz. You can observe a jump of 0.01 MHz in counter reading, but then it should change back to the resonance frequency, which means the circuit is following the resonance.

8. Start the VI program, the program cant stop the sweeping once it is trigged. Otherwise it will cause the ^{3}He to stay at the wrong state and hence a big loss in target polarization.

After EPR measurement, use a program to fit the upper and lower limit of the signal to extract the frequency shift.

Appendix B

A Calculation of the Background Rates

One major issue we discovered during the experiment was the background neutrons from the GE180 glass. A calculation from Perdue [90] has demonstrated the difference. Cross section values were taken from [107, 108].

A	Element	Abundance	Fraction	En(MeV)	nTOF(ns)	counts/hr
10	B	0.1980	0.0079	2.96	31.59	2
11	B	0.8020	0.0321	0.00	5422.39	9
16	O	0.9976	0.5383	0.00	5422.39	0
17	O	0.0004	0.0002	7.26	20.24	0
18	O	0.0020	0.0011	3.36	29.66	1
23	Na	1.0000	0.0282	0.00	5422.39	0
27	Al	1.0000	0.0116	0.00	5422.39	4
28	Si	0.9223	0.3479	0.00	5422.39	0
29	Si	0.0467	0.0176	2.93	31.75	15
30	Si	0.0310	0.0117	0.79	61.05	0
39	K	0.9326	0.0031	0.00	5422.39	4
41	K	0.0.0674	0.0002	1.31	47.43	0

Table B.1: Background Count Rate estimates of Pyrex cell @ 11.4 MeV. The total counts are calculated to be 132 counts/hr. A similar calculation was carried out for GE180 glass, whose background is listed in the following table.

A	Element	Abundance	Fraction	En(MeV)	nTOF(ns)	counts/hr
16	O	0.1980	0.0079	2.96	31.59	2
17	O	0.8020	0.0321	0.00	5422.39	9
18	O	0.9976	0.5383	0.00	5422.39	0
27	Al	0.0004	0.0002	7.26	20.24	0
28	Si	0.0020	0.0011	3.36	29.66	1
29	Si	1.0000	0.0282	0.00	5422.39	0
30	Si	1.0000	0.0116	0.00	5422.39	4
40	Ca	0.9223	0.3479	0.00	5422.39	0
42	Ca	0.0467	0.0176	2.93	31.75	15
43	Ca	0.0310	0.0117	0.79	61.05	0
44	Ca	0.9326	0.0031	0.00	5422.39	4
46	Ca	0.0.0674	0.0002	1.31	47.43	0
48	Ca	0.0004	0.0002	7.26	20.24	0
84	Sr	0.0020	0.0011	3.36	29.66	1
86	Sr	1.0000	0.0282	0.00	5422.39	0
87	Sr	1.0000	0.0116	0.00	5422.39	4
88	Sr	0.9223	0.3479	0.00	5422.39	0
130	Ba	0.0467	0.0176	2.93	31.75	15
132	Ba	0.0310	0.0117	0.79	61.05	0
134	Ba	0.9326	0.0031	0.00	5422.39	4
135	Ba	0.0.0674	0.0002	1.31	47.43	0
136	Ba	0.0467	0.0176	2.93	31.75	15
137	Ba	0.0310	0.0117	0.79	61.05	0
138	Ba	0.9326	0.0031	0.00	5422.39	4

Table B.2: Background Count Rate estimates for GE 180 @ 11.4 MeV

Bibliography

[1] W. Glockle *et al. Phys. Rep.*, 274:107, 1996.

[2] J. Carlson *et al. Rev. Mod. Phys.*, 70:3, 1998.

[3] V.G.J. Stoks *et al. Phys. Rev. C*, 49:2950, 1994.

[4] R.B. Wiringa *et al. Phys. Rev. C*, 51:38, 1995.

[5] R. Machleidt *et al. Phys. Rev. C*, 53:R1483, 1996.

[6] S. A. Coon *et al. Nucl. Phys.*, 317:242, 1979.

[7] J. Carlson *et al. Nucl. Phys. A*, 401:59, 1983.

[8] A. Deltuva *et al. Phy. Rev. C*, 68:024005, 2003.

[9] S. Weinberg *et al. Phys. Lett. B*, 295:114, 1992.

[10] E. Epelbaum *et al. Prog. in Nucl. and Part. Phys.*, 57:654, 2006.

[11] B. Blankleider and *et al. Phys. Rev. C*, 29:538, 1984.

[12] J. L. Friar and *et al. Phys. Rev. C*, 42:2310, 1990.

[13] H. Gao *et al. Phys. Rev. C*, 50:R546, 1994.

[14] W. Xu *et al. Phys. Rev. Lett.*, 85:2900, 2000.

[15] M. Meyerhoff *et al. Phys. Lett. B*, 327:201, 1994.

[16] J. Becker *et al. Eur. Phys. J. A*, 6:329, 1999.

[17] D. Rohe *et al. Phys. Rev. Lett.*, 83:4257, 1999.

[18] J. Bermuth *et al. Phys. Lett. B*, 564:199, 2003.

[19] P.L. Anthony *et al. Phys. Rev. D*, 54:6620, 1996.

[20] K. Abe *et al. Phys. Rev. Lett.*, 79:26, 1997.

[21] K. Ackerstaff *et al. Phys. Lett. B*, 404:383, 1997.

[22] F. Xiong *et al. Phys. Rev. Lett.*, 87:242501, 2001.

[23] J. Golak *et al. Phy. Rept.*, 415:89, 2005.

[24] S. Naito *et al. Phys. Rev. C*, 73:034003, 2006.

[25] R. Skibinski *et al. Phy. Rev. C*, 67:054002, 2003.

[26] A. Deltuva *et al. Phy. Rev. C*, 72:054004, 2005.

[27] E.O. Alt *et al. Nucl. Phys. B*, 2:167, 1967.

[28] A. Deltuva *et al. Phy. Rev. C*, 69:034004, 2004.

[29] A. Deltuva *et al. Phy. Rev. C*, 71:054005, 2005.

[30] S. D. Drell *et al. Phy. Rev. Lett.*, 16:908, 1966.

[31] M. Amarian *et al. Phys. Rev. Lett.*, 89:242301, 2002.

[32] M.W. Ahmed *et al. Phys. Rev. C*, 77:044005, 2008.

[33] A. Deltuva. *Private communication.*

[34] R. Skibinski. *Private communication.*

[35] B.L. Berman *et al. Phys. Rev. C*, 10:2221, 1974.

[36] D.D. Faul *et al. Phys. Rev. C*, 24:849, 1981.

[37] J.R. Bergervoet *et al. Phys. Rev. C*, 41:1435, 1990.

[38] V.G.J. Stoks *et al. Phys. Rev. C*, 48:792, 1993.

[39] R. Machleidt *et al. Phys. Rep.*, 149:1–89, 1987.

[40] R. Machleidt *et al. Phy. Rev. C*, 63:024001, 2001.

[41] S. Wong. *Introductory Nuclear Physics*, 1990.

[42] A. Crowell. *Ph.D. thesis*, 2001.

[43] J. Fujita *et al. Prog. Theor. Phys.*, 17:360, 1957.

[44] M. R. Robilotta *et al. Phys. Rev. C*, 31:646, 1985.

[45] A. Deltuva *et al. Phys. Rev. C*, 80:064004, 2009.

[46] J.D. Bjorken. *Relativistic Quantum Mechanics*, 1964.

[47] R. Skibinski *et al. Phy. Rev. C*, 67:054001, 2003.

[48] R. Skibinski *et al. Phy. Rev. C*, 72:044002, 2005.

[49] A. Deltuva *et al. Phys. Rev. C*, 79:014606, 2009.

[50] A. Deltuva *et al. Nucl. Phy. A*, 790:344c, 2007.

[51] A. Deltuva *et al. Annu. Rev. Nucl. Part. Sci*, 58:27–49, 2008.

[52] S. B. Gerasimov. *Sov. J. Nucl. Phys.*, 2:430, 1966.

[53] J.E. Purcell *et al. Nucl. Phys. A*, page to be submitted, 2010.

[54] F. E. Low. *Phys. Rev.*, 96:1428, 1954.

[55] M. Gell-Mann. *Phys. Rev.*, 96:1433, 1954.

[56] V. Sulkosky. *Ph.D. thesis*, 2007.

[57] V. Sulkosky *et al. http://hallaweb.jlab.org/experiment/E97-110/.*

[58] J.L. Friar *et al. Phys. Rev. C*, 42:2310, 1990.

[59] N. Bianchi *et al. Phy. Lett. B*, 450:439, 1999.

[60] H. Gao *et al. 6th International Workshop on Chiral Dynamics*, 2009.

[61] A.J.F. Siegert *et al. Phys. Rev.*, 52:787, 1937.

[62] H. Weller *et al. Progress in Particle and Nuclear Physics*, 62:257, 2009.

[63] Y. Wu. *Private communication.*

[64] W. Jaus *et al. Nucl. Phys. A*, 608:399, 1996.

[65] S. Stave *et al. TUNL Progress Report*, XLVII:128, 2007-08.

[66] http://www.mesytec.com/datasheets/MPD 4.pdf.

[67] K. Kramer *et al. Nucl. Inst. Method A*, 582:318, 2007.

[68] K. Hagiwara *et al. Phy. Rev. D*, 66:010001, 2002.

[69] *Particle Physics Booklet.*

[70] W. Happer. *Rev. Mod. Phys.*, 44:169, 1972.

[71] K. Kramer. *Ph.D. Thesis, William and Mary*, 2003.

[72] *CRC Handbook of Chemistry and Physics, 74th ed*, 1993.

[73] M. E. Wagshul *et al. Phys. Rev. A*, 49:3854, 1994.

[74] G.D. Cates *et al. Phys. Rev. A*, 37:2877, 1988.

[75] W. Happer *et al. U.S. Patent No.6318092*, 2001.

[76] A. Ben-Amar Baranga *et al. Phys. Rev. A*, 58:2282, 1998.

[77] W. C. Chen *et al. Phys. Rev. A*, 75:013416, 2007.

[78] G. Wang *et al. Phys. Rev. A*, 68:065402, 2003.

[79] Q. Ye. *Ph.D. thesis, Duke University*, 2008.

[80] W. Lorenzon *et al. Phys. Rev. A*, 47:468, 1993.

[81] S. R. Scheafer *et al. Phys. Rev. A*, 39:5613, 1989.

[82] N. R. Newbury *et al. Phys. Rev. A*, 48:558, 1993.

[83] A. S. Barton *et al. Phys. Rev. A*, 49:2766, 1994.

[84] M. V. Romalis *et al. Phys. Rev. A*, 58:3004, 1998.

[85] M. V. Romalis. *Ph.D. thesis, Princeton University*, 1997.

[86] J. S. Jensen. *Ph.D. thesis, Caltech*, 2000.

[87] X. Zheng. *Ph.D. thesis, MIT*, 2002.

[88] W. Korsch. *TJNAF E94-010 Technical Note E94010-TN-11.*

[89] B. Sawatzky. *Ph.D. thesis, University of Virginia*, 2005.

[90] B.A. Perdue. *Private Communication.*

[91] S. Stave. *Private communication.*

[92] M. V. Romalis *et al. Phys. Rev. A*, 56:4569, 1997.

[93] S. Agostinelli *et al. Nucl. Inst. and Meth. A*, 506:250–303, 2003.

[94] B.A. Perdue *et al. TUNL Progress Report*, XLVI:94, 2006-07.

[95] M. Blackston. *Ph.D. thesis, Duke University*, 2007.

[96] J.B. Birks *et al. The Theory and Practice of Scintillation Counting*, 1964.

[97] R. Cecil *et al. Nucl. Inst. Method*, 161:439, 1979.

[98] R.E. Pywell *et al. Nucl. Inst. Method in Physics Research A*, 565:725, 2006.

[99] D.E. Gonzalez Trotter *et al. Nucl. Inst. Method in Physics Research A*, 599:234, 2009.

[100] Y. Birenbaum *et al. Phys. Rev. C*, 32:1825, 1985.

[101] H. Weller *et al. Atomic Data and Nuclear Data Tables*, 58:219, 1994.

[102] M.F. Hsu *et al. Appl. Phys. Lett.*, 77:2069, 2000.

[103] C. Brinker. *Sol-Gel Science, Academic Press*, 1990.

[104] H. Gao *et al. A New Proposal to HIγS*, 2009.

[105] R. Pywell *et al. Nucl. Inst. and Meth. A*, 606:517–522, 2009.

[106] M. Liang. *JLab technical notes*, 2001.

[107] Dietrich and Berman. *Atlas of photoneutron cross section obtained with monoenergetic photons.*

[108] *Atomic data and nuclear data tables*, 38:199–338, 1988.

Biography

Xing Zong was born in Yangzhou, China on March 20th, 1981. He attended Yangzhou Middle School from 1993 to 1999. He obtained his B.S. degree in the Department of Phyics is 2003 from Nanjing University. He came to study at Duke Physics in Aug, 2003 and worked towards a Ph.D. degree in Prof. Haiyan Gao's Medium Physics Group. He co-authored a paper "A High-pressure Polarized ^3He Gas Target for the High Intensity Gamma Source (HIγS) Facility at Duke Free Electron Laser Laboratory". Xing was also active on campus, he and Wei Chen co-founded DukeChina.Org website to bridge Duke's connection with China, and was awarded the Cook Society Gradaute Student Award in Feb 2007. This dissertation was defended in Feb, 2010 at Duke University.